Enabling Millimeter Wave Communications for Use Cases of 5G and Beyond Networks

Mohamed Ibrahim

A Thesis

in

The Department

of

Electrical and Computer Engineering

Presented in Partial Fulfillment of the Requirements

For the Degree of

Doctor of Philosophy (Electrical and Computer Engineering) at

Concordia University

Montréal, Québec, Canada

April 2022

CONCORDIA UNIVERSITY
SCHOOL OF GRADUATE STUDIES

This is to certify that the thesis prepared

By: **Mohamed Ibrahim**

Entitled: **Enabling Millimeter Wave Communications for Use Cases of 5G and Beyond Networks**

and submitted in partial fulfillment of the requirements for the degree of

Doctor of Philosophy (Electrical and Computer Engineering)

complies with the regulations of the University and meets the accepted standards with respect to originality and quality.

Signed by the final examining committee:

_____ Chair
Dr. Ahmed Soliman

_____ External Examiner
Dr. Aboelmagd Noureldin

_____ Thesis Supervisor
Dr. Walaa Hamouda

_____ Examiner
Dr. Alina Stancu

_____ Examiner
Dr. Yousef Shayan

_____ Examiner
Dr. Reza Soleymani

Approved by _____
             Dr. Wei-Ping Zhu, Graduate Program Director

4/25/2022   _____
             Dr. Mourad Debbabi, Dean
             Gina Cody School of Engineering and Computer Science

Abstract

Enabling Millimeter Wave Communications for Use Cases of 5G and Beyond Networks

Mohamed Ibrahim, Ph.D.

Concordia University, 2022

The wide bandwidth requirements of the fifth generation (5G) and beyond networks are driving the move to millimeter wave (mmWave) bands where it can provide a huge increase in the available bandwidth. Increasing the bandwidth is an effective way to improve the channel capacity with limited power. Moreover, the short wavelengths of such bands enable massive number of antennas to be integrated together in small areas. With such massive number of antennas, narrow beamwidth beams can be obtained which in turn can improve the security. Furthermore, the massive number of antennas can help in mitigating the severe path-loss at mmWave frequencies, and realize high data rate communication at reasonable distances. Nevertheless, one of the main bottlenecks of mmWave communications is the signal blockage. This is due to weak diffraction ability and severe penetration losses by many common building materials such as brick, and mortar as well as the losses due to human bodies. Thus, user mobility and/or small movements of obstacles and reflectors cause rapid channel gain variations which leads to unreliable communication links.

The harsh propagation environment at such high frequencies makes it hard to provide a reliable service, hence, maintaining connectivity is one key design challenge in mmWave networks. Relays represent a promising approach to improve mmWave connectivity where they can redirect the signal to avoid the obstacles existing in the propagation environment. However, routing in mmWave networks is known to be a very challenging problem due to the inherent propagation characteristics of mmWave frequencies. Furthermore, inflexible routing technique may worsen network performance and increase scheduling overhead. As such, designing an appropriate transmission routing technique for each service is a crucial issue in mmWave networks. Indeed, multiple factors must be taken into account in the routing process, such as guaranteeing the robustness of network connectivity and providing high data rates.

In this thesis, we propose an analytical framework to investigate the network reliability of mmWave relaying systems for multi-hop transmissions. We also propose a flexible routing technique for mmWave networks, namely the nth best routing technique. The performance of the proposed routing technique is investigated using tools from stochastic geometry. The obtained results provide useful insights on adjusting the signal noise ratio (SNR) threshold for decode and forward (DF) relay according to the order of the best relay, blockage and relay densities in order to improve spectral efficiency. We also propose a novel mathematical framework to investigate the performance of two appropriate routing techniques for mmWave networks, namely minimum hop count (MHC) and nearest LoS relay to the destination with MHC (NLR-MHC) to support wide range of use cases for 5G and beyond networks. Analytical models are provided to evaluate the performance of the proposed techniques using tools from stochastic geometry. In doing so, we model the distribution of hop count using phase-type distribution, and then we use this distribution to derive analytical results for the coverage probability and spectral efficiency. Capitalizing on the derived results, we introduce a comprehensive study of the effects of different system parameters on the performance of multi-hop mmWave systems. These findings provide important insights for designing multi-hop mmWave networks with better performance.

Furthermore, we adapt the proposed relay selection technique for IoT devices in mmWave relaying systems to prolong the IoT device's battery life. The obtained results reveal the trade-off between the network connectivity and the energy consumption of IoT devices. Lastly, we have exploited the enormous bandwidth available in the mmWave band to support reliable fronthaul links for cell-free (CF) massive multiple-input multiple-output (MIMO). We provide a comprehensive investigation of different system parameters on the uplink (UL) performance of mmWave fronthaul-based CF mMIMO systems. Results reveal that increasing the access point (AP) density beyond a certain limit would not achieve further improvement in the UL data rates. Also, the higher number of antennas per AP may even cause UL data rates degradation.

Acknowledgments

First and foremost, all praise and thanks are due to Allah (God) for providing me with the strength to believe in my passion and pursue my dreams. I could never have finished this thesis without the faith I have in Him and depending on Him.

To be able to step strong and smooth in my Ph.D. journey, I have been supported and supervised by Prof. Walaa Hamouda. I could easily say that Prof. Hamouda has a great impact on me, and I learned so much from him. His support and insightful advice were crucial to my academic success and development as an independent researcher. Prof. Hamouda is a caring person that cares about you not only technically but also personally and socially. Prof. Hamouda, thank you for all the research skills and writing skills I have gained throughout the time I worked with you. Without your valuable support, encouragement, and flexibility, this thesis would not have been possible.

I would also like to thank my committee members, Prof. Y.R. Shayan, Prof. Reza Soleymani, Prof. Alina Stancu, and Prof. Aboelmagd Noureldin for the time and effort spent in reading my thesis, taking part in my Ph.D. dissertation defence committee, and providing me with valuable comments and suggestions.

I am sincerely thankful to Concordia Graduate Student Support Program (GSSP) for funding my Ph.D. studies.

My gratitude also goes to my close friends, Salah Elhoushy and Mohammed Elbayoumi. This would have been a much more difficult feat without you. Thank you for your unwavering support and have fun when I have been stressed out. We had nice times, stories, and humor which will be always in my memory. Wishing you the best of luck in your future endeavors.

I would like to express my heartfelt gratitude to my beloved mother, Fatma Ali, for the extraordinary efforts she has exerted to help me reach this important life milestone. Without you and your sincere prayers, I would not be the person I am today. I am also extremely grateful to my sister, Ehsan, and my brother, Mubarak, for their unconditional love and continuous support throughout my life. Last but not least, I would like to express my deepest gratitude to my future wife, Nariman Kamal, for being a steadfast source of encouragement to me. Thank you, Nariman, I am happy to have you in my life.

To my mother, Fatma Ali,
To my future wife, Nariman Kamal,
To my siblings, Ehsan and Mubarak,
To my niece and nephews, Karma, Moaaz, and Ziad
To the soul of my father, Ibrahim Khalil.

Contents

List of Figures

List of Tables

List of Acronyms

3GPP   third generation partnership project.

AF   amplify-and-forward.

AP   access point.

BS   base station.

CB   conjugate beamforming.

CF   cell-free.

CFE   Compress-Forward-Estimate.

CPU   central processing unit.

DF   decode-and-forward.

DL   downlink.

ECF   Estimate-Compress-Forward.

EDCF   Estimate-Detect-Compress-Forward.

FSO   free space optics.

FSPL   free space path-loss.

i.i.d.   independent and identically distributed.

IAB   integrated access and backhaul.

IoT   internet of things.

ITU   International Telecommunication Union.

LoS   line-of-sight.

MHC   minimum hop count.

mMIMO   massive multiple-input multiple-output.

MMSE   minimum mean-square error.

mmWave   Millimeter wave.

MRC   maximum ratio combining.

NLoS   non line-of-sight.

NLR   nearest line-of-sight relay.

NLR-MHC   nearest LoS relay to destination with MHC.

PDF   probability density function.

PPP   Poisson Point Process.

RIS   Reconfigurable Intelligent Surfaces.

SNR   signal-to-noise ratio.

TDD   time-division duplexing.

UEs   user equipments.

UL   uplink.

ZF   zero-forcing.

List of Common Symbols

L length of blockage

W width of blockage

λ_R Density of relays

λ_B Density of blockages

β Blockage density on the link

P transmit power

α Path-loss exponent

A Path-loss intercept

d_{SD} Distance between the source and destination

R_{th} Radius of the sector

K_{max} Hop count constraint

$P_{K_{max}}$ Transition probability matrix

$Q_{K_{max}}$ Intermediate probability matrix

ρ Initial transient state vector

T Absorption vector

p_k Transition probability

χ Log-normal random variable

BW Bandwidth

N_0 Noise power

d_{SD} Distance between source and destination

θ Deviation angle of the sector

N_B Number of blockages

γ_{th} SNR threshold

Chapter 1
Introduction

5G and beyond networks experience a new era of intelligence with connected people and things towards a fully connected intelligent digital world. This new era will lead to true device connectivity through the IoT where billions of devices, such as sensors, are connected among them and with the Internet [3]. In fact, the IoT technology is about the communication and interaction between devices from diverse environments to collect data, process it, and leverage resulting information and knowledge to make the world around us better via smarter and/or automated decision-making. In this spirit, 5G and beyond networks will lay the foundation of a more connected, sustainable society using new technologies such as smart factories, telehealth, augmented/virtual reality applications, smart homes, intelligent security guards, and intelligent transportation systems [4]. These application will shape the performance targets of the 5G and beyond networks. Cellular operators are therefore faced with the challenge of preparing their infrastructure to handle the performance targets of these future applications.

To enable the 5G and beyond networks applications and guarantee their performance requirements, new technologies must be integrated into 5G and beyond networks. In that, new network architectures are being introduced along with emerging technologies to provide powerful services and significant improvements on data rates as well as minimal latency [5]. All of this must be aligned with constrains regarding the specific environment characteristics and spectrum limitations. Use cases of 5G and beyond network applications set different requirement criteria and standards, such as an enormous number of connections, multi-fold increase in data rate, and stringent reliability and latency requirements [6]. For instance, virtual reality has a potential to allow geographically-separated people to communicate effectively in groups. They can make eye contact and can manipulate common virtual objects. It will require the real-time movement of extremely high resolution electro-magentic signals to geographically-distant places to relay various thoughts and emotions. As such, virtual reality will require data rates above 1 terabits-

per-second (Tbps). Additionally, real-time user interaction is bound to require minimum latency and ultra-high reliability [7]. On the other hand, smart transportation, smart grid, and telemedicine need to support massive connectivity for a very large number of devices. These future technologies are facing spectrum shortage challenges mainly due to the massive number of connections and the emerging bandwidth-hungry applications. Millimeter wave (mmWave) communication represents one of the most effective solutions to this spectrum scarcity challenge motivated by the immense amount of bandwidth at mmWave bands [8, 9].

MmWave spectrum naturally emerged as a potential solution for 5G and beyond networks. Although these bands were earlier thought to be unsuitable for the mobile operations due to their unfavorable propagation characteristics, the modern device and antenna technologies made it feasible to use them for commercial wireless applications [10]. In fact, the amount of available spectrum at mmWave frequencies is very large when compared to sub-6 GHz frequencies [11, 12]. As the bandwidth appears in the pre-log factor of the achievable data-rate, mmWave communication can potentially achieve an order of magnitude higher data rate, which made it attractive for inclusion in the 5G standards.

Operating 5G and beyond networks at the mmWave band imposes technological challenges while offering great opportunities. In fact, mmWave signals can propagate only a few miles or less due to a severe path-loss and may be completely blocked by static or dynamic physical blockages [13]. Therefore, small movements of obstacles combined with user mobility can cause the channel to rapidly appear or disappear. The high sensitivity of mmWave signal propagation to blockages greatly affects the link reliability, hence, a line-of-sight (LoS) link is highly desirable for mmWave networks to achieve high reliability. To overcome the aforementioned challenges of mmWave communications, relays will play a more important role to achieve high coverage performance and robustness in communication [14]. In this case, relays redirect the signal to avoid the obstacles existing in the propagation environment. Also, multi-hop transmission is an essential strategy for enabling long-distance mmWave communications and significantly improve the network reliability compared to single-hop mmWave transmissions [15].

1.1 Motivations

The key objectives of this thesis are to:

1. Study the network reliability for mmWave communications and provide efficient solutions based on relaying systems to improve network performance in different perspectives;

2. provide a practical solution to enable the design of the mmWave relaying systems to support IoT devices.

3. Address the potential of mmWave communications to support fronthaul networks for the future wireless networks.

4. Develop analytical and simulation frameworks for the proposed techniques.

The work in this thesis is important as it certainly addresses a vital and timely topic, which is expected to play a major role in mmWave relaying systems. In particular, our proposed work is related to providing efficiency and flexible routing techniques to improve network performance to enable mmWave relaying systems to serve use cases of 5G and beyond networks. In fact, mmWave communication is considered as an appealing technology for the use cases of 5G and beyond networks, such as smart cities, smart manufactures, intelligent transportation systems, autonomous and flying vehicles. Hence, researchers from both academia and industry are exploring new frequency spectrum (mmWave spectrum) to enable the use cases of 5G and beyond networks and guarantee their performance.

MmWave bands have been recognized as a promising technology candidate to support high data rates while maintaining service reliability poses significant challenges for system design. Indeed, the mmWave wireless links are considered highly unreliable because of their unfavorable propagation characteristics, which cause their transmitting beams to be exposed to blockage very easily. This in turn negatively impact the mmWave performance in term of network reliability and latency. As such, multi-hop transmission is an essential strategy for enabling long-distance mmWave transmissions as well as improving the network reliability compared to single-hop mmWave transmissions. Indeed, the multi-hop architecture has certain advantages. By using the multi-hop transmission to split a long transmissions link into multiple shorter communication links, the achievable data rate over the mmWave link could be further increased because of the improved path loss. Moreover, the shorter links reduce the interference range, thus creating the possibility of higher frequency reuse factor. However, multi-hop routing in mmWave networks is known to be a very challenging problem due to the inherent propagation characteristics of mmWave frequencies. In that, designing an appropriate transmission routing techniques

for each service is a crucial issue in mmWave networks. Indeed, multiple factors must be taken into account in the routing process, such as reducing the total latency, guaranteeing the robustness of network reliability, and providing high quality of service. Also, inflexible routing techniques may decrease network performance and increase scheduling overhead due to the inherent characteristics of mmWave signal. In light of this, we believe that novel and flexible routing techniques are required to meet the requirement for each application of 5G and beyond networks.

IoT is widely considered as an important service to be offered by the 5G and beyond networks. Since the traditional cellular networks were designed for services with high data rate and low latency, they experience technical challenges to meet the requirements of IoT devices, such as long device battery life and massive connectivity. Long battery life for sensor nodes is one of the important characteristics for IoT devices, which transmit data by a wireless communication scheme. In fact, IoT devices with intermittent operations sometimes consume a significant amount of power when communication conditions are not favourable, resulting in a battery life that is shorter than expected [16]. As such, it is important to prolong the IoT device's battery life by reducing power consumption due to communication.

Another direction towards meeting the requirements of 5G and beyond networks is to develop reliable network architecture. One of the major technological breakthroughs to cope with these requirements is the cell-free (CF) massive multiple-input multiple-output (mMIMO) systems. In cell-free (CF) massive multiple-input multiple-output (mMIMO) systems, all access point (AP)s are connected to a central processing unit (CPU) which operates all APs as a mMIMO network with no cell boundaries to serve all users by coherent transmission and reception [17]. In doing so, the CPU allows all APs to communicate with all users over the same time-frequency resources by means of spatial multiplexing, provided by the excessive number of APs over the number of users [18]. However, the capacity of the fronthaul network dramatically influences its performance. While wired fronthaul links can be seen as the optimal choice, they may not be practically feasible. Exploiting the enormous bandwidth available in the mmWave band to support the fronthaul links paves the way to achieve the full potential of CF mMIMO systems. Despite the potential of mmWave communications in improving the performance of CF mMIMO systems, the current literature lacks this essential investigation.

1.2   Thesis Contributions

Given the motivating points in the last section, the contributions of this thesis can be summarized as follows.

Network Connectivity for MmWave Networks. In Chapter 3, we evaluate the network reliability of mmWave relaying systems , while taking into account the mmWave signal propagation characteristics. To this end, we introduce a novel analytical framework to analyze the impact of limiting the hop count on the network reliability of mmWave communications using tools from stochastic geometry. We use the discrete phase-type distribution based on stochastic dependence between the states that are spatially dependent. In literature, it is assumed that the density of relays tends to infinity which results in an upper bound for the network connectivity. We differently consider relay density and investigate its impact on the network connectivity. Results obtained via both simulations and analyses reveal the trade-off between the network connectivity and the delay as a function of the hop count.

Spectral Efficiency of Multi-hop Millimeter Wave Networks using N^{th} Best Relay Routing Technique. In Chapter 4, we present the major challenge related to supporting the 5G and beyond network applications with reliable mmWave communication. Motivated by this, we propose a flexible routing technique for mmWave networks to achieves the maximum spectral efficiency compared to other techniques in the literature, while maintaining the network reliability. The performance of the proposed n^{th} best relay routing technique is investigated using tools from stochastic geometry. First, we derive the probability density function (PDF) of the distance between the nth best relay and destination. Capitalizing on this result, we derive a closed-form expression of the coverage probability over the log-normal fading channels. Monte Carlo simulations show an accurate match with the analytical results. We further demonstrate that the coverage probability varies according to specific system parameters, such as density of relays, blockage density and the signal-to-noise ratio (SNR) threshold. Furthermore, we show that the adaptive SNR threshold plays an important role in improving the spectral efficiency for different relay density, blockage density and the order of best relay (n). These findings provide insights for designing multi-hop mmWave networks with better performance.

Performance Analysis of Minimum Hop Count-Based Routing Techniques in Millimeter Wave Networks. In Chapter 5, we mainly address one important aspect of the routing process is the hop count which has a significant effect on network performance. In light of this, we propose two different routing techniques based on the minimum hop count for the path between the source and destination, namely minimum hop count (MHC) and nearest LoS relay to destination with MHC nearest LoS relay to destination with MHC (NLR-MHC) routing techniques. The MHC routing technique targets delay-sensitive applications such as medical and manufacturing, whereas the NLR-MHC provides a higher data rate compared to MHC technique by relaxing the minimum hop count. Different from existing research, we propose a suitable methodology to derive the hop count distribution of both the MHC and NLR-MHC routing techniques based on phase-type distribution. Given the hop count distribution of the two underlying routing techniques, we derive analytical expressions for the coverage and connectivity probabilities as well as spectral efficiency for multi-hop mmWave networks. We verify the accuracy of our analytical results for the two routing techniques through Monte Carlo simulations. Capitalizing on the derived results, we introduce a comprehensive study of the effects of different system parameters on the spectral efficiency, connectivity probability, and average hop count. This investigation provides accurate and insightful expressions for designing multi-hop mmWave networks to improve data rates and latency while maintaining the network reliability.

Reliable Millimeter Wave Communication for IoT Devices. In Chapter 6, we adapt the proposed NLR-MHC technique for IoT devices in mmWave relaying systems to prolong the IoT device's battery life. We investigate the impact of the relay-selected region and the distance between the base station and IoT device on the network connectivity of mmWave relaying systems. The analytical results unveil a high degree of accuracy which is confirmed by extensive simulations at different relay densities, blockage densities, andSNR thresholds. Results obtained via both simulations and analyses reveal the trade-off between the network connectivity and the energy consumption of IoT devices.

Uplink Performance of MmWave-Fronthaul Cell-free Massive MIMO Systems. In Chapter 7, we investigate the uplink (UL) performance of CF mMIMO systems supported by mmWave-fronthaul networks. We considered that the system consists of multiple CPUs to which APs are associated in a distance-based association approach.

Using tools from stochastic geometry, we derive analytical expressions for both the distribution of the provided fronthaul capacity and the average UL data rates. We show that although increasing the density of blockages degrades the average UL data rates, increasing the density of CPUs can limit such effect. Moreover, the obtained results reveal that the network deployment should be adjusted according to the available fronthaul bandwidth and the density of blockages. In particular, increasing the density of APs beyond a certain limit would not achieve further improvement in the UL data rates for a given fronthaul bandwidth.

1.3   Thesis Organization

The rest of the thesis is organized as follows. In Chapter 2, we provide a relevant background for the topics of this thesis. We evaluate the network connectivity for mmWave relaying systems in Chapter 3. In Chapter 4, we introduce the Nth Best Relay Routing Technique for multi-hop mmWave networks, and the performance analysis of minimum hop count-based routing techniques in mmWave networks is derived in Chapter 5. In Chapter 6, we present the nearest line-of-sight relay (NLR) selection technique for IoT devices. The uplink performance of CF mMIMO supported by mmWave-fronthaul networks systems is investigated in Chapter 7. Finally, we present a brief summery of our investigation and some important conclusions, and we suggest some potential topics for future research in Chapter 8.

Chapter 2
Background

In this Chapter, a background for the main topics of this thesis is given. First, we presented an overview of mmWave networks as a promising technology enabling use cases of 5G and beyond networks and discuss the main channel characteristics of mmWave bands. Then, we highlight the concept of relay transmission systems for mmWave networks. Finally, we review some of the tools from stochastic geometry that are utilized in the work proposed in this thesis.

2.1 MmWave Networks

Recently, wireless communication technologies in high frequency bands such as mmWave communication are currently considered as key enabling technologies to meet the unprecedented data rate requirements 5G and beyond networks. This is in fact due to the immense amount of available bandwidth in such frequency bands compared to the available ones in the microwave band, i.e., sub-6 GHz frequency band [9]. Indeed, mmWave signals suffer from a sever path-loss because of the short wavelengths, hence, mmWave signals can propagate only a few miles or less. However, the short wavelengths of mmWave signals enable the integration of massive number of antennas in small areas [19]. For instance, the antenna element spacing could easily fit into an area smaller than 20 mm^2 [20]. Having such massive number of antennas facilitate the generation of fine-grained narrow beams that can significantly improve the communication links [8].

Motivated by the above discussion, the first 5G system based on Release 15 version of the specifications developed by third generation partnership project (3GPP) is currently being deployed commercially throughout the world both at sub-6 GHz and at mmWave frequencies. Lastly, the second version of 5G have been standardized by 3GPP in the Release 16 of the specifications including enhancements for mmWave operation [21]. In particular, the integrated access and backhaul (IAB) feature in Release 16 have addressed

multi-hop backhauling for flexible range extension for mmWave communication [22]. In that, IAB allows base stations to provide both wireless access for devices and wireless backhaul connectivity, which eliminates the need for wired backhauls. While Release 15 and 16 support operation in spectrum up to 52.6 GHz, spectrum support in Release 17 will be extended to 71 GHz. Release 17 will extend means for topology adaptation to enable enhanced backhaul robustness as well as more general topology, and routing for improved efficiency of deployments utilizing IAB.

In what follows, we discuss the main channel characteristics of mmWave communications including the available mmWave bands and propagation characteristics. Also, we introduce adapted blockage modelings in mmWave network.

2.1.1 MmWave Bands

The mmWave spectrum ranges from 3 GHz to 300 GHz with corresponding wavelengths that vary between 1 and 100 mm. In that, the frequency band from 30 GHz to 300 GHz refers to extremely high frequencies, while the one from 3 GHz to 30 GHz is generally indicating the super high frequency band. In the following, we introduce the candidate mmWave bands for 5G and beyond network according to the US Federal Communications Commission regulations [23] and other regions are in the process of making high frequencies available to support fixed and mobile services.

- 28 GHz band (27.5–29.5 GHz)

  The 27.5–28.35 GHz (850 MHz) band operates for local multipoint distribution service, while the portion of 150 MHz, that is 29.1-29.25 GHz is shared on the services such as fixed satellite service, mobile satellite service, and non-local television transmission service, etc. Hence, there is approximately 1 GHz available for mobile broadband.

- 70 GHz and 80 GHz bands (71–76 GHz, 81-86 GHz)

  These bands, known by E-band, consist of 10 GHz and permit the use of smaller antennas for backhauling applications. The International Telecommunication Union (ITU) has allocated these bands for fixed and mobile services. The two contiguous bandwidths of 5 GHz make these bands promising for mobile broadband.

- 90 GHz band (92-100 GHz)

This band, known by W-band, is provisioned for licensed and unlicensed operations for outdoor and indoor applications, respectively. The ITU Radio regulations body has assigned 92-94 GHz and 94.1-100 GHz bands for fixed and mobile services.

Therefore, the 28 GHz, 71–76 GHz, 81–86 GHz, 92-94 GHz and 94.1-100 GHz bands are excellent candidates for fixed and mobile services due to 24 GHz of available bandwidth.

2.1.2   Propagation Characteristics

MmWave communications suffer from serious deterioration due to the propagation losses. In particular, the rain attenuation and atmospheric and molecular absorption characteristics reduce the range of mmWave communications [24]. Fig. 2.1 depicts the rain attenuation and atmospheric absorption characteristics of mmWave propagation [25]. The frequency bands with extremely high-attenuation properties (i.e., 60, 120, 183, 325, and 380 GHz) are allocated for short-range applications, such as wireless personal area network and imaging. On the other hand, the 28, 77, and 240 GHz frequency bands with relatively low space attenuation would be suitable for long-range applications, such as cellular, fronthaul, and vehicular radar. Recently, with new 5G and beyond network technologies such as multi-hop transmission with shorter communication links, mmWave can overcome the aforementioned issues of atmospheric absorption. More specifically, only 7 dB/km of attenuation is expected due to heavy rainfall rates of 1 inch/hr for cellular propagation at 28 GHz [26].

On the other hand, static and dynamic obstacles may completely block the mmWave signals due to its weak ability to penetrate obstacles [27]. For static blockages due to buildings and permanent structures, the authors in [28] conducted propagation measurements at 28 GHz. Results show that indoor clear glass and outdoor brick pillars have penetration losses of 3.6 and 28.3 dB, respectively. For measurements at 73 GHz [29], the penetration losses for many common indoor materials are nearly 25 dB. Hence, a study of network performance for mmWave networks should incorporate the impact of blockages.

Mobile blockers represent the second type of blockage due to pedestrians and vehicles which may cause frequent interruptions to the line-of-sight (LoS) links. Indeed, the 3GPP has identified humans as one of the major factors affecting the mmWave propagation and has incorporated a blockage model into TR 38.901 of Release 14 [30]. For instance, the
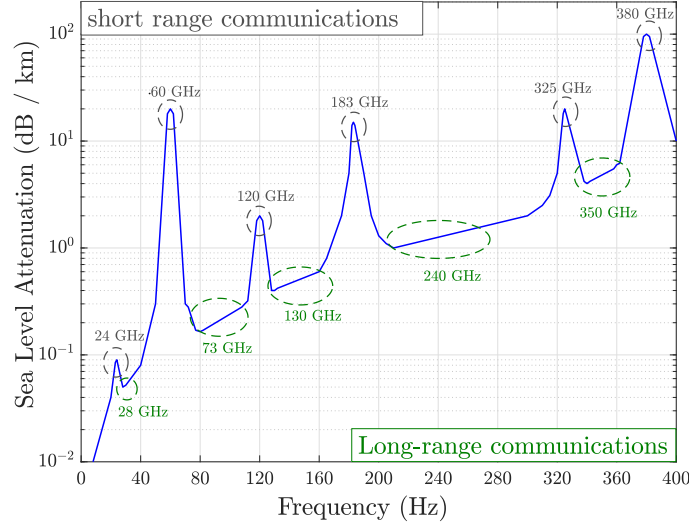
Figure 2.1: Atmospheric and molecular absorption at microwave and mmWave frequency bands.

measurement campaigns in [31] were conducted in a realistic indoor environment in the presence of human activity. Results showed that blockage by a human penalizes the link budget by 20-30 dB, and the channel is blocked for about 1% or 2% of the time. Hence, the non-static environments and the user mobility will lead to large dynamic variances in channel powers. As such, static and dynamic objects in the environment around the user may completely block the mmWave signals. In addition, small movements of the user can cause its channel to rabidly appear or disappear. Hence, an unblocked LoS link is highly desirable for mmWave networks, and every single mmWave signal reception should ensure the LoS between its transmitter-receiver pair.

The commonly adopted path loss models in mmWave networks are free space path-loss (FSPL) and the alpha plus beta. The first path-loss model, denoted as FSPL, represents the attenuation of signal strength between two isotropic antennas in free space. The FSPL between two nodes separated with a radius d can be expressed in dB scale as [32]

$$PL(d) = 20 \ log_{10}\big(\frac{4\pi d_0}{\lambda}\big) + 10 \ n \ log_{10}(\frac{d}{d_0}) + \chi_s, \tag{2.1}$$

where λ is wavelength, and d_0 is the reference distance (1 m). Moreover, the path-loss exponent n equals 2 for free-space, and χ_s is the shadow fading term which is a zero-mean Gaussian variable with a given standard deviation, σ in dB. Note that, (2.1) can be also used to account for the signal losses in non line-of-sight (NLoS) propagation as well, by making channel measurements and then finding a suitable value of n that approximately describes the path-loss measurements as depicted in Table 2.1. The second path-loss

model is the alpha plus beta model which is widely used in industry [33–35]. Its path-loss expression of alpha plus beta model is as follows

$$PL(d) = \mathscr{A} + 10\mathscr{B} \, log_{10}(d) + \chi_s, \tag{2.2}$$

where $\mathscr{A}$ is the best fit floating intercept point over the measured distances, and $\mathscr{B}$ is the slope of the best fit. The parameter values for $\mathscr{A}$, $\mathscr{B}$, and χ_s are determined with a least squares fit to the measured data. Table 2.1 shows the different values for path-loss, and shadowing for different environments in the mmWave bands based on measurements campaigns in New York City in both 28 and 73 GHz bands [24, 33, 36].

Model	Frequency	Scenario	LoS			NLoS		
			$\mathscr{A}$ [dB]	n / $\mathscr{B}$	σ [dB]	$\mathscr{A}$ [dB]	n / $\mathscr{B}$	σ [dB]
Free Space Path Loss	28 GHz	indoor office	-	2.9	13.3	-	4.8	11.9
alpha plus betaPath Loss	28 GHz	indoor office	83.4	0.8	12.2	87.5	2.4	10.1
Free Space Path Loss	73 GHz	indoor office	-	3.1	16.8	-	5.7	16.7
alpha plus beta Path Loss	73 GHz	indoor office	94.5	0.7	15.8	117.8	1.3	11.7
Free Space Path-Loss	28 GHz	outdoor cellular	-	1.1	1.7	-	2.7	9.6
alpha plus beta Path Loss	28 GHz	outdoor cellular	61.4	2	5.8	72	2.92	8.7
Free Space Path-Loss	73 GHz	outdoor cellular	-	4.17	9	-	6.4	15.8
alpha plus beta Path Loss	73 GHz	outdoor cellular	69.8	2	5.8	86.6	2.45	8

Table 2.1: The parameters for the free space path-loss and alpha plus beta path loss models at 28 GHz and 73 GHz.

2.1.3 Blockage Modeling

The impact of blockages on the performance of mmWave networks is a limiting factor where different approaches are introduced to model such blockages [37]. One approach is to model the blockages explicitly in-terms of their sizes, locations, and shapes using data from a geographic information system. This approach is well suited for site-specific simulations using electromagnetic simulation tools such as ray tracing [38–40]. An alternative is to employ a stochastic blockage model where the blockage parameters are drawn randomly according to some distribution. The stochastic approach can be applied to study system deployments under a variety of blockage parameters such as size and density [41, 42]. A simplified model for blockage effect, known as LoS ball model, is developed in [43] for tractable models. In that, a link between two nodes is assumed to have a LoS connection if and only if the separation distance is shorter than a given threshold. However, the randomness in the distance based path-loss is ignored which has a significant impact in empirical studies [44]. As such, the proposed model in [45] assumed each link to be LoS with constant probability if the link length is less than certain threshold D and zero

otherwise. This constant probability represents the average fraction of LoS area in a circular ball of radius D around the point under consideration.

In [46], a model was depicted using a stochastic blockage model where the centers of buildings model as a Poisson Point Process (PPP) where buildings are modeled as rectangle shape with density λ_B. The orientation of the blockages is uniformly distributed in $[0, 2\pi]$, and the lengths and widths of the buildings are independent uniformly distributed with $[L_{min}, L_{max}]$ and $[W_{min}, W_{max}]$, respectively. The number of blockages (N_b) on link follows a Poisson distribution with an average length link. This allows computing the LoS probability of the link which has no blockage using a Poisson distribution with $N_b = 0$. The LoS probability is represented as [46]

$$p_{LoS} = e^{-\beta \, r}. \tag{2.3}$$

The LoS probability is negative exponential function with a length of the link r and β

$$\beta = \frac{2\lambda_B}{\pi} \times (E(W) + E(L)), \tag{2.4}$$

where $E(.)$ denotes statistical expectation.

2.2 Relay Communication Systems

The high sensitivity of mmWave signal propagation to blockages greatly affects the link reliability, hence, a line-of-sight (LoS) link is highly desirable for mmWave networks to achieve high reliability. To overcome the aforementioned challenges of mmWave communications, relays will play a more important role to achieve high coverage performance and robustness in communication [14]. In this case, relays redirect the source signal to avoid the blockages existing in the propagation environment and are essential if the system targets to extend mmWave outdoor coverage to indoor users [47]. To improve the network connectivity of mmWave communications, relays will play a more important role in improving the robustness in communication between BS and user in the case of direct link blocking [9] as shown in Fig. 2.2. Instead of switching from mmWave to microwave band, which can significantly reduce the available bandwidth, relays can assist mmWave signals to turn around the blockages and increase the chance to forward the received signals to the destination [15, 48]. Multi-hop relaying communications are effective in maintaining the network connectivity in scenarios where single-hop communication would suffer from unacceptable outage [49].
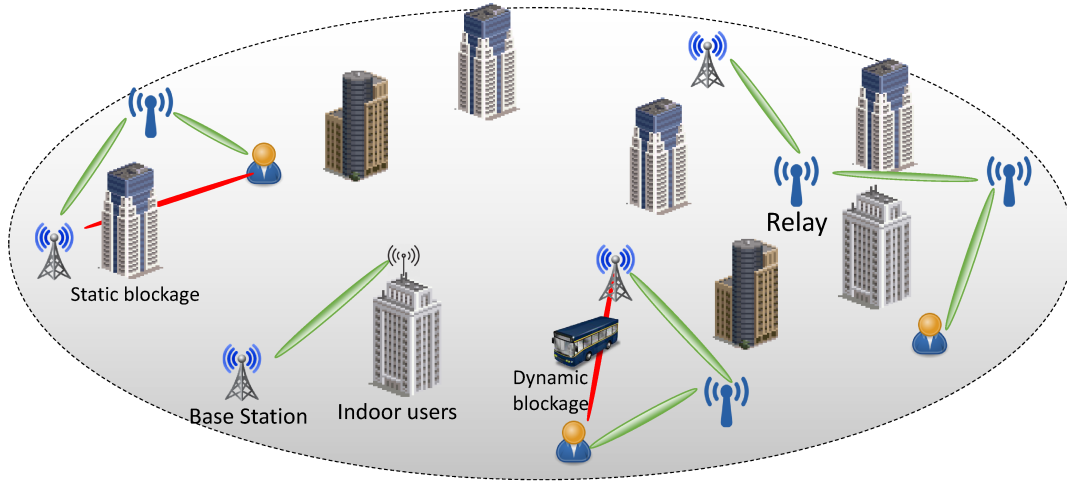
Figure 2.2: Illustration of the communication in mmWave networks when BSs communicate to users via relays.

Relays can be categorized based on their signal processing operation, among which the most popular are decode-and-forward (DF) and amplify-and-forward (AF). In DF technique, relays decode a noisy version of the signal transmitted from the source and retransmit it to the destination [50], while relays amplify a noisy version of the signal transmitted from the source and retransmit it to the destination in AF technique [51,52].

2.3   Stochastic Geometry

To characterize and understand the behavior of mmWave networks, stochastic geometry is a powerful mathematical tool to model different types of wireless networks [53]. The sources of uncertainties such as fading, shadowing, and power control can be incorporated in wireless networks. Analysis using stochastic geometry can lead to closed-form expressions that enable the understanding network operation and provide design guidelines [41]. Stochastic geometry allows to study the average behavior over many spatial realizations of a network whose nodes are placed according to some probability distribution. In stochastic geometry, the most basic objects are point processes, and a point process (PP) can be depicted as a random collection of points in space. A PPP is the most popular point process to model the location of BS and users in wireless networks. The model of PPP generally provides the low bound of performance in reality because the BSs are randomly dropped without any planning [54]. The definition related to PPP and mathematical operations apply to PPP to generate a new PPP [54,55] are given as follows

- Definition 1 (Poisson point process): the PPP is the point process which has the number of point in any set follows a Poisson distribution and the number of points in disjoint sets are independent.

- Definition 2 (homogeneous PPP): the homogeneous PPPs have constant density λ which represents the number of points per unit distance, area or volume.

- Definition 3 (non-homogeneous PPP): the non-homogeneous PPPs have density $\lambda(x)$ that depends on locations according to distance, area or volume.

- Operation 1 (Thinning): thinning operation is applied to PPP with density λ and produces two independent PPP of removed and remaining points with $\lambda_{Removed}$ and λ_{kept}, respectively.

- Operation 2 (displacement): the random independent displacement of PPP with density $\lambda(x)$, produces another PPP with $\lambda_D(y)$, given by

$$\lambda_D(y) = \int \lambda(x)\rho(x,y). \tag{2.5}$$

where $\rho(x,y)$ is displacement kernel function which represents the probability density function of y as a function of x and y .

- Operation 3 (Mapping): If the locations of PPP are mapped according to a function $f(x)$, then produce point process is also a PPP but with a different density $\lambda_m(x)$, defined as.

$$\lambda_m(x) = \lambda(f^{-1}(x)). \tag{2.6}$$

2.4   Summary

In this chapter, we gave the necessary background information related to topics studied in this thesis. First, an overview of mmWave networks as a promising technology enabling use cases of 5G and beyond networks was given. In this regards, we discussed the main channel characteristics of mmWave bands with an emphasis on the adopted blockage models in the literature for mmWave networks. We also shed light on the potential of relaying systems to solve the blockage problems for the mmWave communication. Finally, we presented some mathematical definitions and operations that will be frequently used throughout this thesis.

Chapter 3
Network Connectivity for MmWave Networks

3.1 Introduction

Motivated by the immense amount of bandwidth available at mmWave bands, mmWave communication is expected to play a key role in meeting the requirements of the different use cases of the fifth-generation (5G) and beyond [56]. However, to exploit the full potential of mmWave communications, several challenges need to be addressed such as a severe path-loss and sensitivity to blockages. To extend the range of communications and deal with blockages, the utilization of relays for mmWave communications is recommended and transmission over multiple hops is preferred [49]. Indeed, these relays route the mmWave signals to turn around blockages and forward the traffic generated in the transmitters to their intended receivers. In other words, a blocked link will be replaced by multiple LoS links yielding improved coverage and reliability [34].

The lack of direct links between sources and destinations in mmWave networks is mitigated by using the multi-hop relay system. Indeed, recent studies have demonstrated that multi-hop relaying can significantly improve mmWave connectivity. For instance, the authors in [15] showed that multi-hop relaying can greatly improve the connectivity compared to single-hop mmWave transmissions. However, a larger hop count increases the signaling overhead as well as the scheduling delay is directly proportional to the hop count [57]. In addition, the communication links in mmWave networks are vulnerable due to both blockages and mobility of users. This will significantly increase the delay. Hence, reducing the hop count is essential to yield a smaller delay.

In this chapter, we propose an analytical framework to characterize the network connectivity of mmWave communication. In doing so, we use the discrete phase-type distribution based on stochastic dependence between the states that are spatially dependent.

This distribution is described by a Markov chain with transient states and one absorbing state. Indeed, the authors in [15] studied the connectivity of multi-hop mmWave networks. However, it is assumed that the density of relays tends to infinity which results in an upper bound for the network connectivity. We differently consider relay density and investigate its impact on the network connectivity. Furthermore, we address the impact of limiting hop count on network connectivity in mmWave networks.

3.2 System Model

We consider a downlink transmission for multi-hop networks which consists of a single source, a destination, and a set of relays. The distribution of these relays is modelled as uniform PPP with density λ_R. The destination is assumed to be located at the origin, and the source is located at (x_s, y_s). For simplicity, we assume source and all relays have equal transmit power P, and all relays perform DF strategy. We categorize all links on the network into connection links and relay links. A relay can communicate with source/relays via relay link, while the connection between the destination and relays/source is defined as a connection link. The small wavelength of mmWave signals makes it convenient to pack a large number of antennas into a small space. These antennas provide high directivity gain which compensates for high path-loss. We assume source and relays are equipped with a large number of antennas that provide a narrow beam with a high directivity gain G, and a perfect beam alignment is considered [58]. Hence, the total gain G_t for connection link and relay link are G^2.

Note that mmWave communications suffer from a severe path-loss in the higher fre-
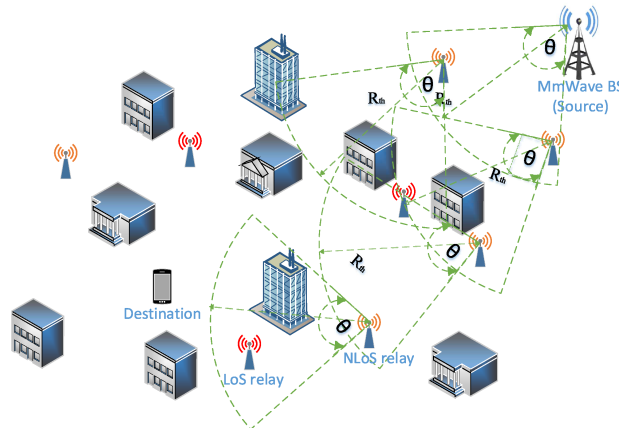
Figure 3.1: A realization of multi-hop mmWave networks.

quency bands, hence, the interference among relays is strongly mitigated which will permit high-level frequency reuse. This will facilitate efficient spectrum utilization and support design of mmWave multi-hop networks. However, each relay on the path may suffer from an inter-beam interference due to transmitted and received beams (self-interference) [59]. To eliminate such self-interference, we consider the frequency reuse of order 2 for the links on the path as it renders transmitted and received beams at each relay orthogonal in bandwidth.

For mmWave networks, the NLoS channel suffers from higher attenuation than the LoS channel as shown in the channel characterization in [60]. Hence, we consider the LoS link only in communication among nodes. For the path-loss model, we assume the reference distance is 1 m, and propagation distance r is attenuated as r^α where α is the path-loss exponent [61]. The corresponding signal-to-noise ratio (SNR) received at the destination is defined as $\gamma = \frac{PG_t}{Ar^\alpha N_0}$, where N_0 is the thermal noise power, and A is path-loss intercept. In DF strategy, relays decode a noisy version of the signal transmitted from the source and retransmit it to the destination if the received SNR is greater than a threshold γ_{th}. Hence, the maximum distance between the source/relay and relay to receive a signal with SNR $\geq \gamma_{th}$ is given by

$$R_{th} = \big(\frac{PG^2}{A\ N_0\gamma_{th}}\big)^{\frac{1}{\alpha}}. \tag{3.1}$$

All transmitting nodes (relays/source) have a visible region defined by a sector as shown in Fig. 3.1. This sector is limited by angle θ and R_{th}. θ is the deviation angle from the direct link between the current node (source/relay) and destination. The connectivity probability p_{con} is a metric to measure the network connectivity, defined as the probability that the user is connected to the network through LoS link(s).

The algorithm in Fig. 3.2 represents the flowchart for finding the path between the source and destination with hop count constraint. It starts with scanning the connections between transmitting nodes (source/relays) and the receiving nodes (relays/destination) where N_R is the number of relays. The active connection between nodes depends on the blockage-free link. It also depends on the location of receiving node which has to exist on the sector of the any transmitting node. The connectivity matrix C includes the connection status of the links between transmitting nodes and the receiving nodes. Each $C_{i,j}$ in matrix C equals 1 if transmitted node i has an active connection with receiving nodes j; otherwise $C_{i,j} = 0$. Using the connectivity matrix, we build the graph
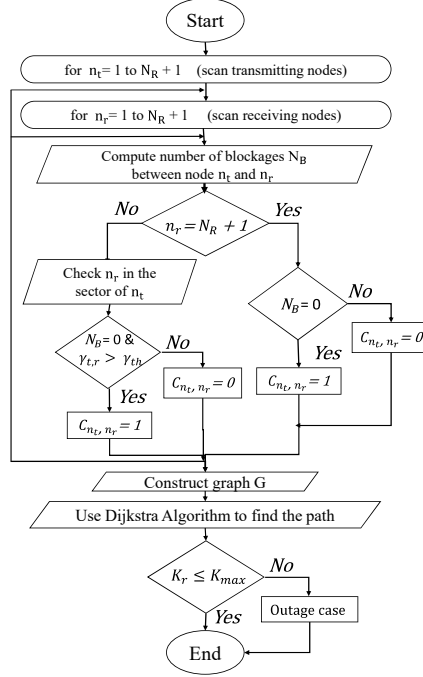
Figure 3.2: Flow diagram of finding the path between the source and destination with hop count constraint.

between nodes connected by active connections. Then we use the Dijkstra's shortest path algorithm [62] to select the relays between source and destination. We do a standard run of the Dijkstra algorithm with equal cost for each link. Finally, when the path hop count does not exceed the maximum hop count K_{max}, this path is valid; otherwise, the destination will be in an outage case.

3.3 Network Connectivity Analysis

Our proposed framework comprises of modeling routing process as Markov stochastic processes with the phase-type distribution. A phase-type distribution describes a random variable generated by one or more Markov stochastic process(es), and it possesses some transient states and a single absorbing state. Each transient state can be characterized for our model by three parameters: transition probabilities to the next state, the absorbing state, and the outage state. Our representation of a phase-type distribution is shown in Fig. 3.3. In the context of the routing process in mmWave networks, transitions through the transient states could correspond to transmit data through relays. The number of states from the commencement of the process (source) until moving into the absorbing state (destination) is referred to as the hop count of the path.
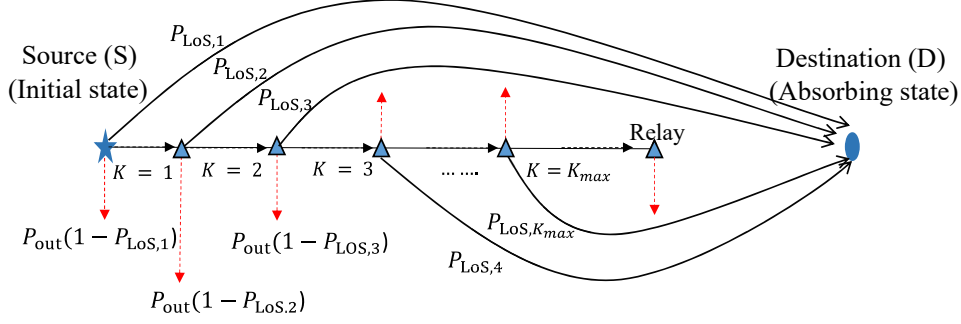
Figure 3.3: Representation of K_{max}-state Markov process for routing technique with hop count constraint.

To find the connectivity probability p_{con}, we derive the three parameters of the phase-type distribution. These parameters represent the transition probability from the current state to the next state. We firstly focus on the transition probability to outage state, p_{out} which is represented by the dotted red line in Fig. 3.3. The outage probability at each state depends on the density of active relays that receive the signal with $SNR \geq \gamma_{th}$. We start characterizing the density of active relays as a function of blockage and relay densities as well as γ_{th}. Indeed, blockages divide a set of relays into two subsets for each relay node, where the first subset contains relays that have LoS connection with the current state, and the others have NLoS connection. Active relays form non-homogeneous PPPs, and we use the properties of PPPs to compute the density of active relays. Using dependent thinning for relays [53], the density of LoS relays is derived as follows

$$\lambda(r) = \int_{-\theta/2}^{\theta/2} e^{-\beta r}\, \lambda_R r\; dl = \theta \lambda_R\; r\; e^{-\beta\; r}. \tag{3.2}$$

Then, the SNR point process can be defined by mapping the relays distances to SNR as shown in [53]. By defining SNR as $q = \frac{PG^2}{N_0 A} r^{-\alpha} = C r^{-\alpha}$ and using the LoS relay density, the density of SNR points is derived by substituting distance r to SNR q in (3.2), to give

$$\lambda(q) = \frac{\theta}{\alpha} \lambda_R C^{\frac{2}{\alpha}} e^{-\beta\; (C/q)^{\frac{1}{\alpha}}} q^{\frac{-2}{\alpha}-1}. \tag{3.3}$$

The active relays have LoS connection with the destination and achieve $SNR \geq \gamma_{th}$. Hence, the active relay intensity is derived as follows

$$\Lambda(\gamma_{th}) = \int_{\gamma_{th}}^{\infty} \lambda(q)\; dq = \int_{\gamma_{th}}^{\infty} -\frac{\theta}{\alpha} \lambda_R C^{\frac{2}{\alpha}} e^{-\beta\; (C/q)^{\frac{1}{\alpha}}} q^{\frac{-2}{\alpha}-1} d\; q$$

$$\overset{(t=\beta(\frac{C}{q})^{1/\alpha})}{\Longrightarrow} \frac{\theta \lambda_R}{\beta^2} \int_{0}^{\beta(\frac{C}{\gamma_{th}})} t\; e^{-t}\; d\; t = \frac{\theta \lambda_R}{\beta^2}\; \Gamma(2,\; \beta(\frac{C}{\gamma_{th}})^{1/\alpha})\;, \tag{3.4}$$

where $\Gamma(.\;,\;.)$ is defined as the lower incomplete gamma function. The current node (relay
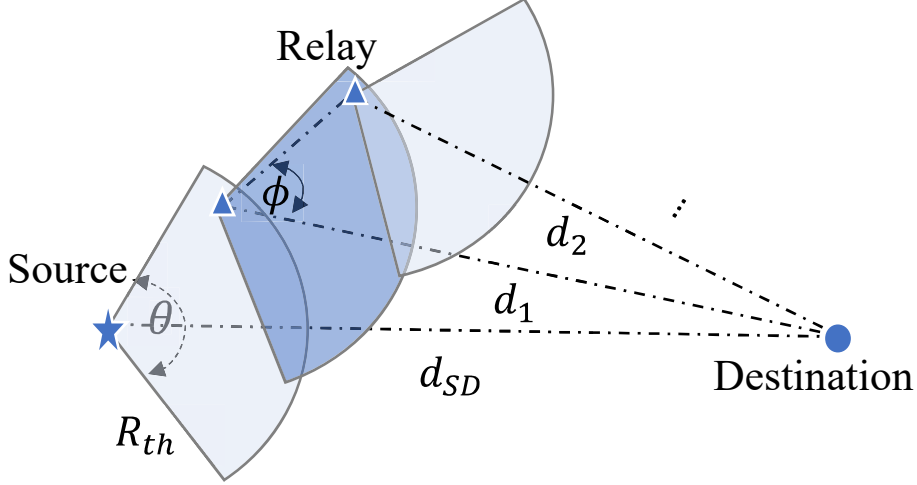
Figure 3.4: A graphical representation for distance from the current state to destination.

or source) transits to the outage state when all relays on the sector are blocked or have SNR less than γ_{th}. Hence, using the active relay intensity and the void probability of a PPP [53], the outage probability at the current state is given by

$$p_{out} = e^{-\Lambda(\gamma_{th})} = e^{-\frac{\theta\lambda_R}{\beta^2} \Gamma(2, \beta(\frac{C}{\gamma_{th}})^{1/\alpha})}. \tag{3.5}$$

Next, we find the transition probability to the absorption state. The absorption occurs in each state k depends on the distance between state k and destination as shown in Fig. 3.4. For the direct link between source and destination, the absorption probability is equivalent to the probability of LoS between source and destination.

$$P_{LoS,1} = p_{LoS} = e^{-\beta\, d_{S,D}}, \tag{3.6}$$

where $d_{S,D}$ is the distance between the source and destination. To find the absorption probability $P_{LoS,k}$ at each state (relay) k, one has to find the average distance between the destination and relay k. Here, the location of relays are distributed uniformly in the any given area, and the relay k has LoS connection with relay $k-1$. Hence, the number of blockages between two relays k and $k-1$, $N_B(k, k-1) = 0$. Based on this, we derive the distribution of the distance from relay $k-1$ to relay k as follows

$$f_{R_k}(r) = P(R_k = r | N_B(k, k-1) = 0) = \frac{\frac{2r}{R_{th}^2}e^{-\beta r}}{\int_0^{R_{th}} \frac{2x}{R_{th}^2}e^{-\beta x}d\,x} = \frac{\beta^2 r e^{-\beta r}}{1 - e^{-\beta R_{th}}(1 + \beta R_{th})}. \tag{3.7}$$

Then, integrating over the obtained distribution within the sector of relay $k-1$, the average distance d_k between relay k and destination can be expressed by

$$d_k = \frac{1}{\theta} \int_{-\theta/2}^{\theta/2} \int_0^{R_{th}} (r^2 + d_{k-1}^2 - 2\,r\,d_{k-1}\,cos(\phi))^{0.5} \times f_{R_k}(r)\,d\,r\,d\,\phi. \tag{3.8}$$

Note that the relay k may be located on any position on the sector of relay $k-1$.

Hence, we firstly derive the probability that there is a LoS relay with destination on the sector S_{k-1} of relay $k-1$ as follows

$$\mho = P(N_B(k,D) = 0 | k \in S_{k-1}) = \frac{1}{\theta} \int\limits_{-\theta/2}^{\theta/2} \int\limits_{0}^{R_{th}} e^{-\beta(r^2 + d_k^2 - 2rd_k \cos(\phi))^{0.5}} f_{R_k}(r) \ dr \ d\phi.$$

(3.9)

$$= \frac{1}{\theta} \int\limits_{-\theta/2}^{\theta/2} \int\limits_{0}^{R_{th}} \frac{e^{-\beta(r^2 + d_k^2 - 2rd_k \cos(\phi))^{0.5}} \ \beta^2 r e^{-\beta r}}{1 - e^{-\beta R_{th}}(1 + \beta R_{th})} dr \ d\phi.$$

Note that the relay intensity in the sector is derived as follows

$$\Lambda_A(r) = \int\limits_{-\theta/2}^{\theta/2} \int\limits_{0}^{r} e^{-\beta x} \ \lambda_R x \ dx \ d\phi = \frac{\theta \lambda_R}{\beta^2} \left(1 - \beta r e^{-\beta r} - e^{-\beta r}\right).$$

(3.10)

Let us define the absorption probability $P_{LoS,k}$ as the probability of at least one relay on the sector has LoS connection with the destination. For given m relays in the sector, we calculate the absorption probability $P_{LoS,k}$ as follows

$$P_{LoS,k} = 1 - \sum_{m=0}^{\infty} (1 - \mho)^m P(M = m) = 1 - \sum_{m=0}^{\infty} (1 - \mho)^m \frac{(\Lambda_A(r))^m}{m!} \times e^{-\Lambda_A(r)}$$

(3.11)

$$= 1 - exp(-\mho \ \Lambda_A(r)).$$

The distributions of hop count can be now represented in matrix notation. The absorption vector T which includes the absorption probability $P_{LoS,k}$ is expressed as follows:

$$T = [P_{LoS,1}, P_{LoS,2}, \ldots, P_{LoS,K_{max}}],$$

(3.12)

where K_{max} indicates the hop count constraint. The transition probability matrix $P_{K_{max}}$ for the routing process represents the probabilities of transit between states and has the form

$$\mathbf{P_{K_{max}}} = \begin{pmatrix} 0 & p_1 & 0 & \ldots & 0 \\ 0 & 0 & p_2 & \ldots & 0 \\ \ddots & \ddots & \ddots & \ddots & \ddots \\ 0 & 0 & 0 & \ldots & p_{K_{max}} \\ 0 & 0 & 0 & \ldots & 0 \end{pmatrix},$$

(3.13)

where p_k denotes the transition probability, given by

$$p_k = (1 - P_{LoS,k})(1 - p_{out}^h).$$

(3.14)

Let ρ denotes a vector of probabilities defining the initial transient state, given by

$$\rho = [1, 0, \ldots, 0].$$

(3.15)

Here, we find the hop count distribution given that there is a path between source and destination (number of available paths $N_{path} > 0$). Therefore, the hop count distribution

is defined as follows

$$f_K(k) = P(K = k|N_{path} > 0) = \frac{P_{DPH}(k)}{\sum_{k=1}^{K_{max}} P_{DPH}(k)}, \tag{3.16}$$

where P_{DPH} is the probability of discrete phase-type distribution with parameters $P_{K_{max}}, \rho$ and T, and it can be formulated as

$$f_{DPH}(k) = \rho \; P_{K_{max}}^{k-1} \; T. \tag{3.17}$$

According to (3.17) and (3.16), the hop count distribution is given by

$$f_K(k) = \frac{\rho P_{K_{max}}^{k-1} \; T}{\sum_{k=1}^{K_{max}} \rho P_{K_{max}}^{k} \; T} \qquad for \;\; k \geq 1. \tag{3.18}$$

Therefore, the connectivity probability with limiting the hop count to K_{max} can be calculated using the hop count distribution as follows

$$P_{Con} = \sum_{k=1}^{K_{max}} \rho P_{K_{max}}^{k-1} T. \tag{3.19}$$

3.4 Simulation Results

Here, we show and discuss simulation results and numerical examples to give insights on the impact of the hop count constraint on the multi-hop mmWave network performance. All simulation results are averaged over 500×10^3 realizations, and the simulations consider a square area fixed to [1000 m × 1000 m]. We assume that buildings have length and width range of [10 m, 25 m], and [10 m, 20 m], respectively. Similar to [36], the path-loss exponent $\alpha = 2$ and path-loss intercept $A = 69.8$ dB for LoS links. The network is assumed to be operated at 73 GHz with a system bandwidth $BW = 2$ GHz. The transmit power $P = 30$ dBm, the thermal noise is given by $-174 + 10 \; log_{10}(BW)$ dBm, noise figure $= 10$ dB, and antenna gain for relays and source $G = 10$ dB.

Fig. 3.5 depicts the hop count distribution with minimum hop count constrain as a function of SNR threshold γ_{th} and d_{SD} for $K_{max} = 15$ and $\theta = 120°$. As shown in Fig. 3.5, the theoretical results are consistent with the simulated ones. The system parameters of the scenario in Fig. 3.5.a are $\lambda_R = \lambda_B = 4 \times 10^{-4} m^{-2}$, and $d_{SD} = 500$ m. Analyzing the results presented in Fig. 3.5.a, we observe that the mean and variance of hop count distribution increase as γ_{th} becomes higher. This is due to the fact that higher value of γ_{th} leads to shrinkage in the sector area, hence, the required hop count to reach the destination rises. It can also be noted that the probability that the source reaches the destination with 3 hops or less is 90 % and 25 % for $\gamma_{th} = 10$ and 15 dB, respectively. Fig. 3.5.b illustrates the hop count distribution for two different distances from source

(a) Varying γ_{th} (b) Varying d_{SD}
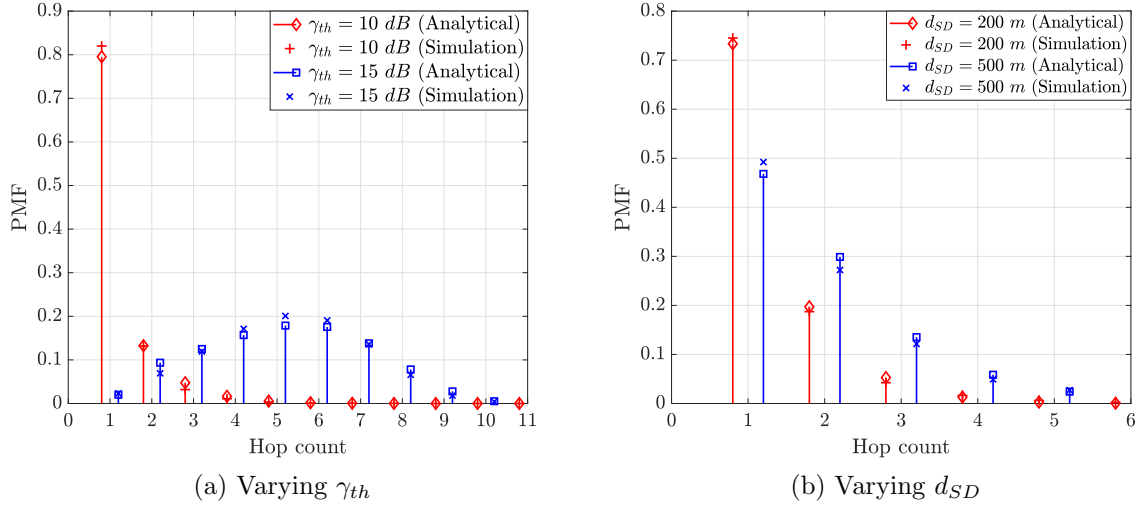
Figure 3.5: The hop count distribution as a function of d_{SD}, and γ_{th}.

to destination, $d_{SD} = 200~m$ and $500~m$. The system parameters of the scenario in Fig. 3.5.b are $\lambda_R = 4 \times 10^{-4}m^{-2}$, $\lambda_B = 1 \times 10^{-4}m^{-2}$, and $\gamma_{th} = 15$ dB. Note that the mean and variance of hop count distribution increase as the distance from source to destination increases. This is because the probabilities of LoS between source/relays and destination depend mainly on the corresponding distances. The effect of blockage and relay densities on the hop count distribution is illustrated in Fig. 3.6 for $d_{SD} = 500~m$ and $\gamma_{th} = 10$ dB. As one may notice that increasing the relay density from $1 \times 10^{-4}m^{-2}$ to $2 \times 10^{-4}m^{-2}$ leads to increase in the required hop count from source to destination. The reason is that an increase in relay density renders larger number of relays in the sectors, and this improves the connectivity by increasing the hop count between source and destination. It can also be noted that the required hop count decreases as the density of blockages becomes smaller. This is a direct implication of the blockage phenomenon, where small values of blockage density lead to higher probabilities of LoS between source/relays and destination.

In Fig. 3.7, the connectivity probability is depicted as a function of K_{max}, and λ_B with $\lambda_R = 4 \times 10^{-4}m^{-2}$, $\theta = 120°$, $d_{SD} = 300~m$, and $\gamma_{th} = 15$ dB. The results indicate that, with a fixed hop count constraint, the connectivity probability significantly decreases as the density of blockages increases. The reason is that increasing the blockage density decreases the availability of LoS relays in the sector, hence, the possible paths from source to destination lessens. As one may observe the connectivity probability starts to increase with K_{max} but finally saturates regardless of the increase of K_{max}. Indeed, the results
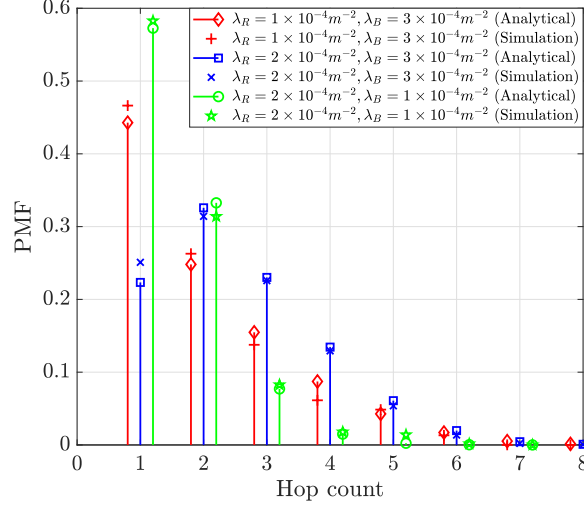
Figure 3.6: The hop count distribution as a function of blockage and relay densities.

reveal that the saturation limit has a strong relation with λ_B.
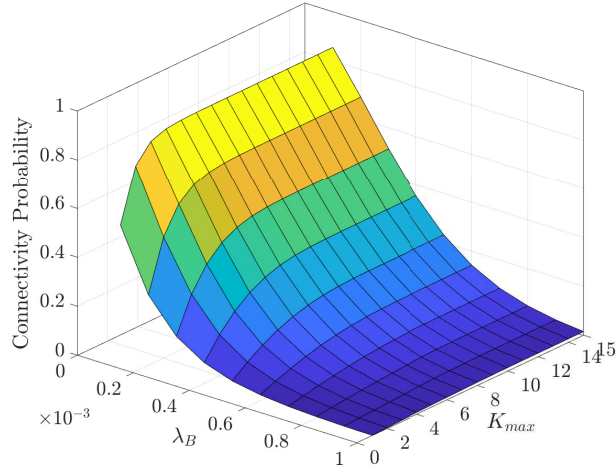
Figure 3.7: The connectivity probability as a function of λ_B and K_{max}.

To understand the impact of relay density on the connectivity probability, Fig. 3.8 plots the connectivity probability versus λ_R for $\lambda_B = 4 \times 10^{-4} m^{-2}$ with the same system parameters as in the scenario of Fig. 3.7. Increasing the density of relays has a dramatic improvement on the connectivity probability, and the rate of improvement depends on K_{max}. This is because an increase in relay density rises the number of relays in the sector, and the possibility to have a LoS relay with the destination in the sector increases. Considering higher hop count constraint and higher relay density, this dramatically increases the number of possible paths between source and destination which in turn improves the connectivity probability. We notice that the connectivity probability increases with K_{max}, however, it saturates and reaches a maximum at a given density of relays.
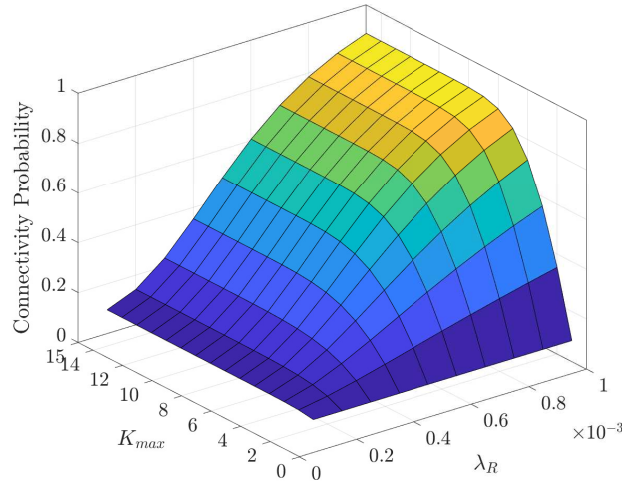
Figure 3.8: The connectivity probability as a function of λ_R and K_{max}.

3.5 Summary

In this chapter, we introduced an analytical framework to characterize the hop count distribution with minimum hop count constrain for mmWave networks. The hop count distribution is modelled as a phase-type distribution, and its parameters are derived using tools from stochastic geometry. Capitalizing on the hop count distribution, we investigate the impact of limiting the hop count on the connectivity of mmWave networks. We further demonstrate that the network connectivity varies according to specific system parameters, such as the densities of relays and blockages. Monte Carlo simulations showed an accurate match with the analytical results. The results showed the significant impact of the relay and blockage densities on the hop count distribution as well as the connectivity probability. Our results revealed that limiting the hop count has significant effects on connectivity probability. Results obtained via both simulations and analyses reveal the trade-off between the network connectivity and the delay as a function of the hop count.

Chapter 4

Performance of the Nth Best Routing Technique for MmWave Networks

4.1 Introduction

Smart manufacturing, intelligent transportation, smart homes, and intelligent security guards drive our lives into a higher level of convenience and efficiency. These future technologies are facing spectrum shortage challenges mainly due to the emerging bandwidth-hungry applications. MmWave communication represents one of the most effective solutions to this spectrum scarcity challenge motivated by the immense amount of bandwidth at mmWave bands [9]. In fact, mmWave networks are susceptible to blockages due to high penetration losses and severe diffraction loss [43]. To maintain connectivity between a transmitter and receiver pair in mmWave networks, two approaches are proposed when a direct link is blocked. The first approach is to switch from mmWave to microwave band, which can significantly reduce the available bandwidth. The second approach is to use multi-hop communications by relaying data. In that, relays can assist mmWave signals to turn around the blockages and increase the chance to forward the received signals to the destination as shown in the previous chapter.

Relay selection is a well-investigated topic in microwave spectrum range. However, there are few studies for mmWave band. One of the most common relay selection techniques is the best relay selection scheme, which selects the relay that minimizes the path-loss with the destination [2]. For instance, the authors in [1] analyzed three different relay selection techniques for a dual-hop relay mmWave network. It is shown that the best relay selection outperforms other selection schemes in-terms of coverage probability and spectral efficiency. Results in [1] showed that there is a gap between the simulation and analytical results that is caused by using fixed probability of LoS to model the blockage. However, the blockage process represents dependent thinning process [63] that depends on

distances among the destination and its relays. Hence, the exponential modelling of blockages accurately describe a real deployment scenario. Furthermore, this model provides more tractability in multi-hop performance analysis than fixed probability of LoS [64].

The best relay selection technique, discussed in [1, 2] considers only the impact of the static blockage. However, the mobility of users in the environment makes wireless channels alternate between blocked and unblocked LoS states. Indeed, even when the active user is static, the movements of other nearby objects, such as humans and vehicles, may cause LoS blockage [65]. Also, the best relay selection technique selects a single relay from a set of potential relays. However, two users or more may select the same best relay. Hence, one needs to study the performance of the second, third, or more generally the nth best relay. The selection of the nth best relay in traditional microwave systems is addressed in several research works, such as in [66,67]. For instance, the authors in [66] derived closed-form expression for the outage probability of the nth best DF relay networks. Moreover, the work in [67] derived closed-form expressions for the end-to-end bit error rate and outage probability for the nth best relay in cooperative network. In fact, the performance of nth best relay in mmWave networks is challenging due to the inherent characteristics of mmWave signals such as blockages that distinguish this network from other wireless networks. Furthermore, in applications that demand high reliability in mmWave networks, users need to remain connected to the base station (BS) through different relay links as well as switch between them in case of its active connection drops [68].

In this chapter, we propose a relay selection technique that aims at reducing the transmission distance between user and relay. In this technique, the user selects the nearest LoS relay that minimizes the link length between relay and user which is vulnerable to blockages. In addition, the proposed relay selection technique uses multiple hops by applying the minimum number of hops routing technique between the nearest LoS relay and the source. Moreover, we analyze the performance of mmWave networks at different orders of the best selected relay, up to the nth best relay. More specifically, we derive closed-form expressions for the coverage probability and the spectral efficiency for the general case of the nth best relay. Furthermore, we propose an adaptive SNR threshold technique based on the density of relays and buildings as well as the order of the best relay to maximize spectral efficiency.

4.2 System Model

We consider a multi-hop system, which consists of a single source, a destination and a set of relays as shown in Fig. 4.1. The positions of the relays are distributed as points of uniform PPP with density λ_R. The destination is assumed to be located at the origin, the distance between source and destination is fixed, and all relays and source have equal transmit power P. The small wavelength of mmWave signals makes it convenient to pack a large number of antennas into a small space. These antennas provide high directivity gain which compensates for high path-loss. Therefore, transmitting nodes in our model are equipped with a large number of antennas that provide a narrow beam with a high directivity gain, and a perfect beam alignment is considered [58].

Since NLoS transmission links suffer from higher attenuation than LoS links [36], we consider the LoS link only. In mmWave networks, measurement results indicated that small-scale fading is less severe than that in conventional systems when narrow beam antennas are used. Also, shadowing is more significant in such systems, hence, small scale fading can be ignored compared to blockage and shadowing [1, 36]. Note that mmWave communications have a severe path-loss in the higher frequency bands. Therefore, the interference among relays is strongly mitigated which will permit high-level frequency reuse. This will facilitate efficient spectrum utilization and support design of mmWave multi-hop networks. Nevertheless, each relay on the path may suffer from an inter-beam interference due to transmitted and received beams (self-interference) [59]. To eliminate such self-interference, we consider the frequency reuse of order two as it renders transmitted and received beams at each relay orthogonal in bandwidth.

MmWave networks are more noise-limited compared to conventional networks which are strongly interference-limited [45]. Hence, the SNR for the link provides a good approximation to signal-to-interference plus noise ratio (SINR) for directional mmWave networks. The SNR of the link between source and relay and among relays are formulated in [36] as

$$\gamma_{S,R} = \frac{P\,G^2\,\chi^{-1}}{N_0\,A\,r_{S,R}^{\alpha}}, \tag{4.1}$$

$$\gamma_{R,R} = \frac{P\,G^2\,\chi^{-1}}{N_0\,A\,r_{R,R}^{\alpha}}, \tag{4.2}$$

where $r_{S,R}$ and $r_{R,R}$ are the link distances between source and relay and between two
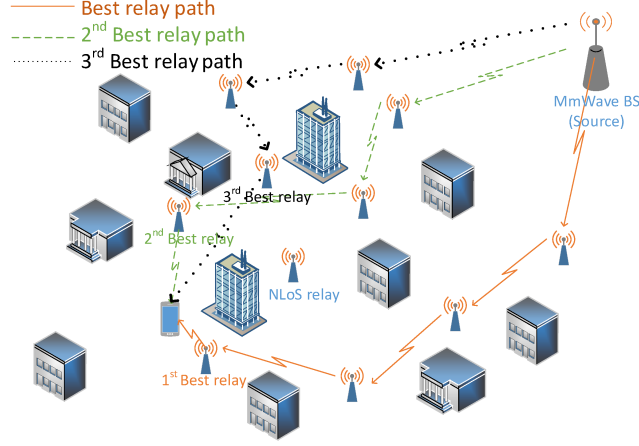
Figure 4.1: System model for multi-hop relaying system in mmWave networks.

relays, respectively, and N_0 is the noise power, and G is the directivity gain in the main lobe. A and α are the float variables that fit the slope and intercept linear data measurement, respectively. The SNR at the destination from the relay is defined in [36] as

$$\gamma_{R,D} = \frac{P\,G\,\chi^{-1}}{N_0\,A\,r_{R,D}^{\alpha}}, \tag{4.3}$$

where $r_{R,D}$ is the link distance between relay and destination. The deviation in the fitting χ in dB scale is modeled as a Gaussian random variable with zero mean and variance σ^2 in log scale and log-normal in linear scale. The PDF of log-normal random variable [1] is defined as

$$f_X(\chi) = \frac{10\,log_{10}(e)}{\chi\,\sqrt{2\pi}\,\sigma}exp\left(-\frac{(10\,log_{10}(\chi)-\mu)^2}{2\,\sigma^2}\right). \tag{4.4}$$

The SNR of the link between source and destination $\gamma_{S,D}$ can be approximated as

$$\gamma_{S,D} = \min_{j=1,\ldots,h}\gamma_j, \tag{4.5}$$

where h is the number of shorter links in the path, and γ_j is the SNR of link j. Note that relays should have SNR greater than or equal γ_{th} to be selected. Hence, all links from source to the nth best relay have SNR greater than or equal to the SNR threshold γ_{th}. Thus, $\gamma_{S,D}$ can be equivalent to SNR $\gamma_{R,D}$ between destination and the last relay in the path. The spectral efficiency for the path from source and destination can be defined as the throughput for a given link per Hertz, given in [2] as

$$\tau(\gamma_{th}) = \frac{1}{2}\log_2(1+\gamma_{th})\,P(\gamma_{S,D} > \gamma_{th}), \tag{4.6}$$

where $P(\gamma_{S,D} > \gamma_{th})$ is the coverage probability, defined as the probability of received SNR at the destination being above γ_{th}, and the factor of $1/2$ is due to frequency reuse 2.

4.3 N^{th} Best Relay Routing Technique

The harsh propagation environment at high frequencies makes it hard to provide a reliable service. Using the multi-hop transmission, it is possible to route the signal in such environments over many hops from source to destination and improves the reliability by combating the blockage effect. Indeed, the mmWave links are considered as highly unreliable due to its unfavorable propagation characteristics as its transmitting beam can be obstructed very easily [69]. Furthermore, an inflexible relay routing technique significantly degrades network performance and increases scheduling overhead. For instance, the first best relay is not always available due to dynamic blockage. In such scenario, the selection criterion should be relaxed to select the best available relay, i.e., 2nd, 3rd, or more generally the nth best relay. Hence, we propose a flexible relay routing technique, which selects the nth nearest LoS relay to the destination. Then, the path from the nth best relay to the source is obtained by applying the minimum number of hops technique. For instance, the solid lines and the dashed lines in Fig. 4.1 depict the first and the second best relay paths from the source to the destination, respectively.

Indeed, relays are able to participate in transmitting the signal if the relay decodes the signal correctly. Hence, there are many paths from source to destination for multi-hop relays. In our model, we select the nth best relay to the destination which has the nth lowest path-loss and LoS connection. Relays on the path between source and the nth best relay are selected according to the minimum number of hops. Hence, the proposed relay selection technique for multi-hop is a combination of the minimum number of hops and the nth best relay selection technique. The proposed routing technique can be summarized by Algorithms 4.1 and 4.2. Algorithm 4.1 gives out the pseudocode to create the connections between source and relays as well as among relays. In Algorithm 4.1, we start by defining the attributes of buildings and the position of source and relays and then find the LoS connections between source and relays or among relays. Based on the SNR threshold, we build the connectivity matrix between nodes C.

Using the connectivity matrix for the network, one can determine the path from source to destination as shown in algorithm 4.2. Firstly, we find the LoS relays, and sort them according to the distance with the destination. Then, we translate the connectivity matrix to a graph of nodes G, and the shortest path between the nth best relay node and source is

---

Algorithm 4.1: Algorithm for Setting Relays Connections

Input: $(N_R, \boldsymbol{Pos_R}, Pos_S, N_B, \boldsymbol{A_B}, \gamma_{th})$

Output: $(\boldsymbol{C})$;

  N_R = number of relays;

  $\boldsymbol{Pos_R}$ = matrix of relays positions;

  Pos_S = vector of source position

  N_B = number of buildings;

  $\boldsymbol{A_B}$ = matrix of attributes of buildings;

  for $u = 1$ **to** $N_R + 1$ **do**

    for $v = 1$ **to** N_R *and* $v \neq u$ **do**

      Create line L between relays of u and v or source and relay v;

      Intersection check between L and all buildings;

      N_P = number of intersection points;

      if *($N_P = 0$)* **then**

        Compute SNR $\gamma_{u,v}$ using (4.2)

        $\boldsymbol{C}(u,v) = (\gamma_{u,v} \geq \gamma_{th})$

Algorithm 4.2: Algorithm for Selecting the Path with n^{th} Best Relay

---

Input: $(Pos_U, N_R, \boldsymbol{Pos_R}, N_B, \boldsymbol{A_B}, \boldsymbol{C}, N_R)$;

Output: $(\vec{Path})$;

Pos_U = vector of attributes of user position;

  for $u = 1$ **to** N_R **do**

    Create line L between relay of u and destination;

    Intersection check between L and all buildings;

    N_P = number of intersection points;

    if *($N_P = 0$)* **then**

      Compute distance D(u) between relay u and destination

    else

      $D(u) = \infty$

  Sort relays according to distance and select the nearest n^{th} relay;

  Construct the graph G using connectivity matrix $\boldsymbol{C}$;

  Find path nodes $\vec{Path}$ between source and the nth best relay using Dijkstra algorithm;

---

obtained using the Dijkstra algorithm. We use the Dijkstra's shortest path algorithm [62] to select the relays between the source and the nth best relay. We do a standard run of the Dijkstra algorithm with an equal cost for each link, and the shortest path is defined as the path with the least cost.

4.4   Coverage Probability Evaluation

In this section, we analyze the coverage probability of the nth best relay to find the spectral efficiency. Firstly, we derive a closed-form expression for the distance of the link between destination and the nth best relay. Then, we derive a closed-form expression for the coverage probability of the nth best relay. In the nth best relay technique, each destination can be served by the nth nearest relay. Relays seen from destination form independent and non-homogeneous PPP with density functions $\Lambda_{\mathcal{O}}(r)$. The intensity measure of non-homogeneous PPPs for a given area $\mathcal{O}$ is derived as

$$\Lambda_{\mathcal{O}}(r) = \int_0^r e^{-\beta x}\, 2\pi\lambda\, x\, dx = \frac{2\pi\lambda_R}{\beta^2}\left(1 - \beta r e^{-\beta r} - e^{-\beta r}\right). \tag{4.7}$$

According to *Poisson law* [70], the probability that a circle contains exactly n relays is $P(n, \mathcal{O}) = \frac{[\Lambda_{\mathcal{O}}(r)]^n}{n!}e^{-\Lambda_{\mathcal{O}}(r)}$. Then, the PDF of the distance between destination and the nth nearest node is given as

$$f_{R_n}(r) = \frac{[\Lambda_{\mathcal{O}}(r)]^{(n-1)}}{(n-1)!}\, e^{-\Lambda_{\mathcal{O}}(r)}\frac{d\Lambda_{\mathcal{O}}(r)}{dr}. \tag{4.8}$$

Note that for $n = 1$ which represents the selection of the nearest LoS relay (the 1st best relay), we can find the distribution of distance from the best relay to the destination as

$$f_{R_n}(r) = 2\pi\, \lambda_R\, r\, e^{\left(-\beta r - \frac{2\pi\lambda_R}{\beta^2}\left(1 - \beta r e^{-\beta r} - e^{-\beta r}\right)\right)}. \tag{4.9}$$

We now evaluate the coverage probability for the nth best relay technique. Let $Q_n = (P\,G)/(N_0\,A\,r_n{}^{\alpha})$ be the SNR without shadowing. We use mapping from distance (r_n) to Q_n as in [63], and find the PDF of Q_n as follows

$$F_{Q_n}(q_n) = P\left(\frac{P\,G}{N_0\,A\,r_n{}^{\alpha}} < q_n\right) = 1 - F_{R_n}\left(\left[\frac{P\,G}{N_0\,A\,q_n}\right]^{1/\alpha}\right), \tag{4.10}$$

$$f_{Q_n}(q_n) = \frac{(P\,G)^{1/\alpha}}{\alpha\, q_n(N_0\,A\,q_n)^{1/\alpha}}f_{R_n}\left(\left[\frac{P\,G}{N_0\,A\,q_n}\right]^{1/\alpha}\right). \tag{4.11}$$

The shadowing χ and Q_n are independent random variables, hence, the joint PDF is given by

$$f_{Q_n,X}(q_n, \chi) = f_X(\chi)\,\times\, f_{Q_n}(q_n). \tag{4.12}$$

Log-normal distribution X with zero mean has the same distribution of Log-normal

distribution $1/X$. Hence, we can use the transformation of variables method [63] to transfer joint PDF of shadowing and SNR without shadowing to joint PDF of the SNR with shadowing by defining $S_1 = Q_n/X$ and $S_2 = Q_n \times X$. After some mathematical manipulations, the Jacobian $J(q, \chi) = 2S_1$, S_1 and S_2 have the same distribution, $Q_n = \sqrt{S_1 S_2}$, and $X = \sqrt{S_2/S_1}$. For $n = 1$, we can find the joint PDF of SNR of the best relay which is calculated as follows

$$f_{S_1,S_2}(s_1, s_2) = \frac{f_{Q_n,X}(q_n, \chi)}{J(q_n, \chi)}$$

$$= \frac{K_1}{s_2 s_1}(\gamma_{s_1,s_2})^{1/\alpha} \quad exp\left[\frac{-(10log(\sqrt{\frac{s_2}{s_1}}))^2}{2\sigma^2} - \beta(\gamma_{s_1,s_2})^{1/\alpha} - \frac{2\pi\lambda_R}{\beta^2}\right. \qquad (4.13)$$

$$\left. \times \left(1 - e^{-\beta(\gamma_{s_1,s_2})^{1/\alpha}}(\beta(\gamma_{s_1,s_2})^{1/\alpha} + 1)\right)\right].$$

where $\gamma_{s_1,s_2} = (P\ G)/(\sqrt{s_1 s_2} \times N\ A)$, and $K_1 = (10\ log(e)\ \pi\ \lambda_R)/(\sqrt{2\pi}\ \alpha\ \sigma)$. Then, the coverage probability is given by

$$P_{\Gamma_{best}}(\gamma_{th}) = P(\gamma_{S,D} > \gamma_{th}) = \int_{\gamma_{th}}^{\infty} \int_{0}^{\infty} f_{S_1,S_2}(s_1, s_2)\ ds_1\ ds_2. \qquad (4.14)$$

4.5   Simulation Results

Here, we present numerical examples to validate the system model and verify the accuracy of the analytical results presented in the previous section. We evaluate the distance distribution and the coverage probability for different scenarios via Monte Carlo simulations. All simulation results are averaged over 500×10^3 realizations. The simulations consider a square area fixed to $[1000\ m \times 1000\ m]$. We assume that buildings have length and width range of $[10\ m,\ 25\ m]$, and $[10\ m,\ 20\ m]$, respectively. Similar to [36] and [45], the standard deviation σ of the log-normal channel is 5.2 dB, $A = 69.8$ dB and the path-loss exponent $\alpha = 2$ for LoS links. The network is assumed to be operated at 73 GHz with a system bandwidth $BW = 2$ GHz. The transmit power $P_t = 30$ dBm, the thermal noise is given by $-174 + 10\ log_{10}(BW)$ dBm, noise figure $= 10$ dB, and antenna gain for relays and source $G = 15$ dB.

In Fig. 4.2, we verify the accuracy of the derived distribution of distance from the nth best relay to the destination given in (4.8) with $\lambda_R = 5 \times 10^{-4}\ m^{-2}$, and $\beta = 0.0103\ m^{-1}$. In each realization, the nodes are randomly and uniformly distributed over the square area. As noted, the analytical results are consistent with simulations. As one note that

the distance distribution of the nth best relay has a maximum value that changes according to order n. This is because the distance distribution of nth best relay is a function of two terms as shown in (4.8). The first term is $[\Lambda_{\mathcal{O}}(r)]^{n-1}$ increases with increasing r, however, the second term is a negative exponential of r and independent of n. We can note that the gap in the mean and variance between the 1st and 2nd is greater than the one between 2nd and 3rd. The reason is that the first term, which increases with r, is less than 1. Hence, the rate of increase in the first term decreases as the order of the best relay (n) increases.
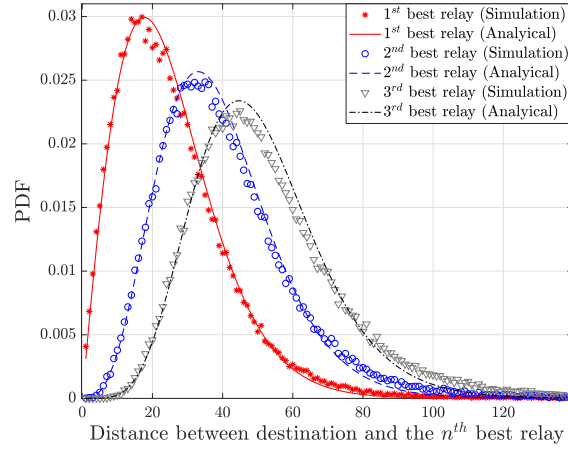
Figure 4.2: The probability distribution functions of distance from the best three relays to the destination.

The coverage probability for the nth best relay is illustrated in Fig. 4.3. The system parameters are the density of relays $\lambda_R = 5 \times 10^{-4}\ m^{-2}$, and $\beta = 0.0103\ m^{-1}$. Overall, the simulation results are in perfect agreement with the theoretical ones. It can be seen from the figure that the gap in coverage probability between the first best relay and the second is larger than the one between the second and the third best relay. This is explained by the fact that coverage probability of the nth best relay depends on the distribution of the distance between the nth best relay and destination, and the gap in the distance distribution decreases as the orders of the best relays increase.
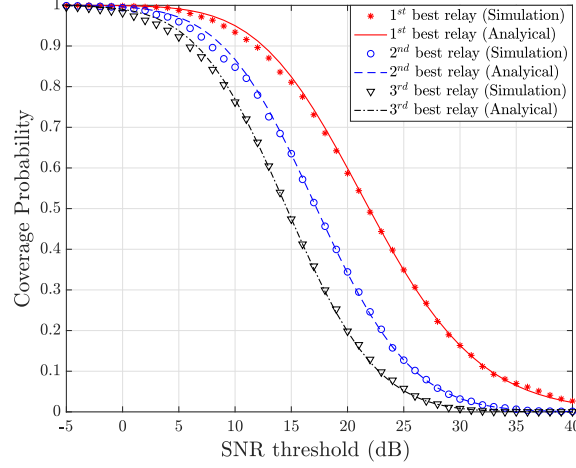
Figure 4.3: Comparison of SNR distribution for the best three relays.

In Fig. 4.4, we investigate the coverage probability of the best relay for different densities of relays and buildings at SNR threshold $\gamma_{th} = 5$ and 10 dB. It is noticed that the coverage probability has a significant increase with increasing the density of relays. For instance, the coverage probability rises from 0.65 to 0.9, when density of relays λ_R goes from 1×10^{-4} to $5 \times 10^{-4} m^{-2}$ at $\gamma_{th} = 10$ dB. This is due to the fact that increasing the relay density renders the best relay (nearest LoS relay) to be near the destination which significantly improves the coverage probability. The blockage density β decreases from 0.0103 to 0.00103, while the coverage probability has considerable improvement, but this improvement diminishes as the density of relays increases.
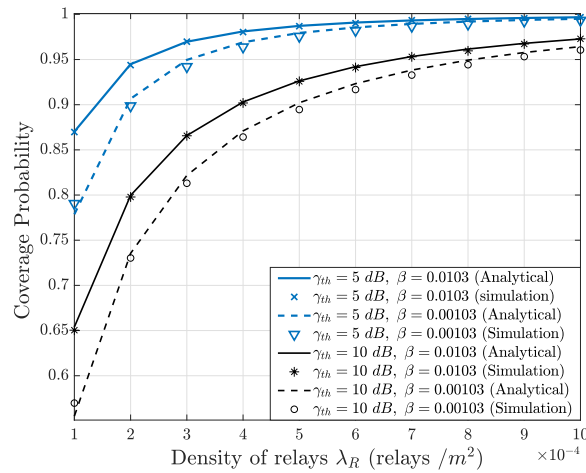
Figure 4.4: Comparison of coverage probability for different density of relays and different density of buildings.

Fig. 4.5 shows the spectral efficiency versus SNR threshold γ_{th} for three best relays

when $\lambda_B = 5 \times 10^{-4} \ m^{-2}$ and $\lambda_R = 5 \times 10^{-4} m^{-2}$. This relation is convex since the spectral efficiency is due to a product of two functions where the coverage probability is a decreasing function, and the log function is an increasing function. Hence, it is quite obvious for the spectral efficiency to reach an optimal point at a certain SNR threshold for the nth best relay. Note that the optimal points for spectral efficiency are at 10 dB, 12 dB, and 15 dB for the three best relays, obtained numerically from (4.6) due to the convexity property for the spectral efficiency. It is clear from this figure that the maximum spectral efficiency is achieved at different values of SNR threshold γ_{th} depending on the order of best relay (n). Furthermore, the gap in the spectral efficiency between the first and second best relay is larger than between the second and third best relay.
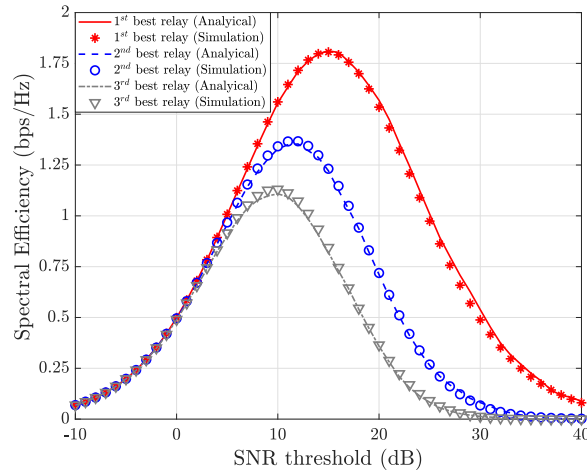
Figure 4.5: Spectral efficiency for the best three relays as function of SNR threshold.

We compare our relay selection technique with the best relay technique, studied in [1, 2] in-terms of the coverage probability and spectral efficiency. Fig. 4.6 shows the coverage probability and spectral efficiency at different distances between the source and the destination. We use the same channel propagation model, and densities of blockages and relays $\lambda_B = \lambda_R = 5 \times 10^{-4} m^{-2}$. It is observed that the performance of our proposed relay selection technique outperforms the relay selection in [1, 2] in-terms of the coverage probability and spectral efficiency. As shown in Fig. 4.6.a, the coverage probability curves for our proposed selection technique are the same for different distances, while the best relay in [1, 2] significantly decreases as the distance between the source and destination increases. We can note from Fig. 4.6.b that the maximum spectral efficiency for 1st and 2nd best relay is more than 1.5 and 2.5 times, respectively that achieved for the best relay

in [1,2]. The reason is that the relay routing technique in [1,2] selects the best relay based on minimizing the path-loss between relay and destination. Also, the best relay has to connect directly to the source with SNR $\geq \gamma_{th}$. However, in the nth best relay selection technique, the multi-hop transmission allows us to select the LoS relay that achieves the lowest path-loss. This leads to maximizing the spectral efficiency.

| (a) Coverage probability | (b) Spectral efficiency |
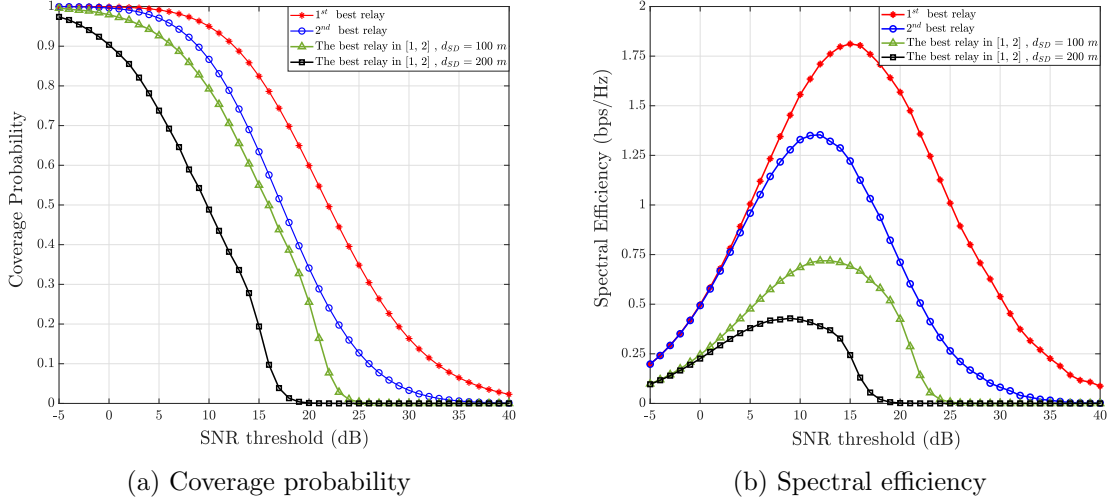
Figure 4.6: Performance of the proposed relay selection technique and the best relay routing technique in [1,2] for different distance between source and destination

To show the impact of selecting the SNR threshold, we consider multi-user in the network, and the users form PPP with density $\lambda_U = 5 \times 10^{-5} \ m^{-2}$. Moreover, we consider the dynamic blockage on the link between the nth best relay and each user as Bernoulli random variable with equal probability to be blocked or not. Here, we consider a scenario where each user can select one from the first k best relays according to availability of LoS link, and we discuss the impact of SNR threshold selection on the average spectral efficiency in the network. Under these assumptions, we show the effect of adapting the SNR threshold on spectral efficiency with $k = 3$ in Fig. 4.7. The impact of adjusting the SNR threshold according to the order of the best relay for different relay densities is shown in Fig. 4.7.a. As shown, increasing the density of relays improves the average spectral efficiency, and where the gain of adjusting the SNR threshold increases with the density of relays. For example, the average spectral efficiency for $\lambda_R = 2 \times 10^{-4} \ m^{-2}$ are 1.531 and 1.689 bps/Hz for adaptive and constant SNR threshold, respectively. The impact of building density on the average spectral efficiency is addressed for $\lambda_R = 5 \times 10^{-4} \ m^{-2}$ in Fig.4.7.b. It is noticed that the proposed adaptive SNR threshold technique achieves

gain on the average spectral efficiency of approximately 10 %. For instance, the average spectral efficiency rises from 2.719 to 2.967 bps/Hz for $\lambda_R = 2 \times 10^{-4}$ m^{-2}. Moreover, the average spectral efficiency reduces with increasing the density of buildings. The key insight from these results is that the SNR threshold should be adjusted according to the order of the selected relay. Besides, the increase in the relay density improves the average spectral efficiency, and the growth of building density has a significant impact on the average spectral efficiency.

(a) Varying λ_R (b) Varying λ_B
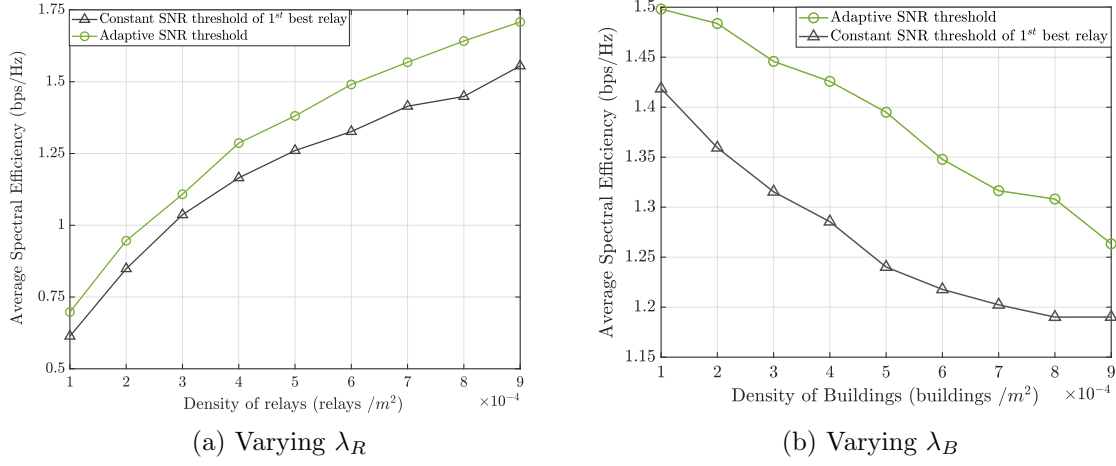
Figure 4.7: Average spectral efficiency for two techniques as a function of densities of relays and blockages.

4.6 Summary

In this chapter, we proposed a novel routing technique for mmWave networks to improve the spectral efficiency. The performance of the proposed n^{th} best relay routing technique is investigated using tools from stochastic geometry. First, we derived the distribution of the distance between the nth best relay and destination. Capitalizing on this result, we derived closed-form expressions of the coverage probability and spectral efficiency over the log-normal fading channels. Monte Carlo simulations show an accurate match with the analytical results. We further demonstrated that the coverage probability varies according to specific system parameters, such as density of relays, blockage density and the SNR threshold. Furthermore, we show that the adaptive SNR threshold plays an important role in improving the spectral efficiency for different relay density, blockage density and the order of best relay (n). These findings provide insights for designing multi-hop mmWave networks with better performance.

Chapter 5

Performance Analysis of Minimum Hop Count-Based Routing Techniques in MmWave Networks

5.1 Introduction

In the previous chapters, we showed that multi-hop relaying can significantly improve the network connectivity compared to single-hop mmWave transmissions. Moreover, deploying relays can achieve a significant improvement in-terms of coverage probability and spectral efficiency. Routing in mmWave networks is known to be a very challenging problem due to the inherent propagation characteristics of mmWave frequencies. In that, designing an appropriate transmission routing technique for each service is a crucial issue in mmWave networks. Indeed, multiple factors must be taken into account in the routing process, such as reducing the total latency, guaranteeing the robustness of network connectivity, and providing high quality of service. Due to these limitations relative to traditional networks, some new algorithms have been proposed for the routing problem in mmWave networks. For instance, the authors in [48] proposed a path selection scheme using a heuristic algorithm to solve the blockage problem and achieve the quality of service requirements of flows. Also, the work in [71] presented a heuristic multi-path routing technique in a dense multi-hop mmWave network. In [72], the authors addressed the problem of traffic allocation for multi-hop scheduling in mmWave networks. However, the impact of blockages was not accounted for in [71, 72].

Despite the significant impact of the employed routing technique on the performance of routing techniques on the mmWave networks, only few works considered the stochastic geometry-based analysis. Unlike a deterministic approach in which analysis is carried for given specific system parameters, stochastic geometry offers a statistical approach

to develop a tractable and accurate modeling framework to characterize the multi-hop transmissions for mmWave networks. For instance, the authors in [73] derived the outage performance of the multi-hop mmWave network in the presence of blockage effects. Also, the authors in [64] derived closed-form expressions for coverage probability, rate coverage, and symbol error rates for multi-hop mmWave networks. In [74], the authors studied the hop distance characteristics and their impact on the outage probability of multi-hop mmWave networks for two different routing techniques, namely, the furthest neighbor routing and the nearest neighbor routing technique. However, the dependence between the links on the path from source to destination was not considered. Indeed, most of previous works in multi-hop mmWave networks (e.g., [64, 73]) assumed that the relays on the multi-hop path are equidistant. However, in practical scenarios, the density of available relays is always limited, especially for mmWave networks due to blockages. Therefore, the positions of the relays are randomly allocated, and in some cases no available relay can be found between the source and destination. In addition, the authors in [75] proposed a quasi-equal-distance routing protocol considering random relay distribution and compared with the ideal equidistant routing. Results showed that the random relay deployment suffers from a significant performance loss compared to the ideal equidistant relays case. Therefore, unlike former studies, we consider the distribution of relays and blockages.

One important aspect of the routing process is the hop count which has a significant effect on network performance. As such, minimum hop count (MHC) is a widely used technique in wireless sensor networks [76], where sensors send their data to the source with the path that is comprised of the minimum number of relays. For mmWave networks, communication links are vulnerable due to blockages which bring the accumulative effect on the packet loss rate. With the increase of hop count, the end-to-end packet loss rate gets higher, which has vital importance on the end-to-end delay [57, 77]. The significant impact of hop count has been investigated on conventional microwave networks [78, 79]. However, in multi-hop mmWave networks, the existence of blockages definitely weakens the ability of routing techniques and brings the limitation of hop count [42]. Indeed, many users require paths that can guarantee the availability of LoS links and achieve the minimum hop count [76]. Hence, we analyze the performance of two different routing techniques based on the minimum hop count for the path between the source and destination, namely MHC and nearest LoS relay to destination with MHC (NLR-MHC) routing techniques. The MHC

routing technique targets delay-sensitive applications such as medical and manufacturing, whereas the NLR-MHC provides a higher data rate compared to MHC technique by relaxing the minimum hop count.

In this chapter, we propose a suitable methodology to derive the hop count distribution of both the MHC and NLR-MHC routing techniques based on phase-type distribution [80]. The MHC routing technique selects the path with the minimum number of links between source and destination. In the second routing technique, referred to as NLR-MHC, the destination selects the nearest LoS relay that should exist within a sector deviated from the direct link to the source with angle θ. Then, the path between the source and NLR is obtained by minimizing the number of links between the source and the NLR. The distribution of hop count for mmWave networks has not been derived in the literature. Hence, we model the hop count distributions using discrete phase-type (DPH) distribution based on stochastic dependence between the spatially dependent states. Given the hop count distribution of the two underlying routing techniques, we derive analytical expressions for the coverage and connectivity probabilities for multi-hop mmWave networks. We verify the accuracy of our analytical results for the two routing techniques through Monte Carlo simulations. Capitalizing on the derived results, we introduce a comprehensive study of the effects of different system parameters on the spectral efficiency, connectivity probability, and average hop count.

5.2   System Model

We consider the transmission of a multi-hop network which consists of a single source, a destination, and a set of relays. The relay locations are modeled as points of uniform PPP with density λ_R. The destination and source are located at the origin and (x_s, y_s), respectively. We assume both source and relays are equipped with a large number of antennas that provide a narrow beam with a high directivity gain G, and a perfect beam alignment is considered [58]. Hence, the total gain G_t for the link between source and relay and among different relays are G^2. Without loss of generality, the destination is assumed to have an omni-directional antenna. Also, we assume source and relays have equal transmit power P, and all relays perform DF protocol. Similar to the previous chapters, we consider frequency reuse of order two as it renders transmitted and received beams at each relay orthogonal. Also, we consider the LoS link only in communication between

transmitting and receiving nodes. In fact, many operations such as discovering neighbors and exchanging routing information rely on a control channel. Since microwave communications provide higher link stability compared to mmWave counterpart, the control channel should be transmitted over an omni-directional transmission at microwave frequencies [81]. It is well known that small scale fading can be ignored compared to blockage and shadowing due to the adoption of highly directional antennas and the weak capability of reflection and diffraction of the mmWave signals [36]. Furthermore, mmWave networks in an urban setting are more noise-limited compared to conventional cellular networks which are interference limited as shown in [45, 82].

5.3   Routing Selection Technique

5.3.1   MHC Technique

A multi-hop transmission significantly improves the connectivity of mmWave networks, while it leads to an increase in the delay as well as signaling overhead. To reduce such delay and signaling overhead, a routing technique that minimizes the hop count and improves the network connectivity is desired. As such, we introduce an MHC routing technique for mmWave networks considering the impact of blockages. In fact, identifying static blockages, including buildings and other static obstructions, has become an important design aspect of mmWave networks where the need for highly detailed data, known as clutter data, becomes crucial. Algorithm 5.1 describes the pseudo-code for the MHC technique that starts with scanning the connections between source and relays as transmitting nodes, and the receiving nodes which represent relays and destination. Similar to [74, 83], relay/source selects the next relay which exists in a sector defined by radius R_{th} and deviation angle θ as shown in Fig. 5.1.a. The radius R_{th} depends on the SNR threshold γ_{th} of the DF relaying, and θ represents the deviation angle from the direct link between the current node (source/relay) and destination.

For an active connection, the receiving node (relay) should exist on the sector of the transmitting node and has a LoS connection with the transmitting node, while the active connection with the destination is based on a blockage-free link. The connectivity matrix $\boldsymbol{C}$ includes the connection status of the links among transmitting and the receiving nodes. The entries $\boldsymbol{C}(n_t, n_r) = 1$ if transmitting node n_t has an active connection with receiving

---

Algorithm 5.1: Pseudo-code for MHC Routing technique.

Input: $(N_R, N_L, M_R, M_L, M_S, M_D, \gamma_{th}, \theta)$,
Output: (P_{MHC});
N_R and $N_L \rightarrow$ Number of relays and blockages.
M_R, M_L, M_S and $M_D \rightarrow$ Positions of relays, blockages, source, and destination.
Sector radius $R_{th} = (\frac{P(G)^2}{A\ N_0 \gamma_{th}})^{\frac{1}{\alpha}}$.

for *Each transmitting node (relay/source)* $n_t = 1$ **to** $N_R + 1$ **do**

  for *Each receiving node (relay/destination)* $n_r = 1$ **to** $N_R + 1$ *and* $n_t \neq n_r$ **do**

    Create line L between transmitting node n_t and receiving node n_r

    Find the number of intersection points N_B between L and all blockages;

    if $(N_B = 0)$ & $(n_r \neq N_R + 1)$ **then**

      Compute distance d_{n_t, n_r} between transmitting node and receiving node.

      Compute angle φ between the two vectors which represent the link from source/relay n_t to relay n_r and the link from source/relay n_t to destination.

      if $(\varphi \leq \theta/2)$ & $(d_{n_t, n_r} \leq R_{th})$ **then**

        $\boldsymbol{C}(n_t, n_r) = 1$

      else

        $\boldsymbol{C}(n_t, n_r) = 0$

    else

      if $(N_B = 0)$ & $(n_r = N_R + 1)$ **then**

        $\boldsymbol{C}(n_t, n_r) = 1$

      else

        $\boldsymbol{C}(n_t, n_r) = 0$

Construct the graph G using connectivity matrix $\boldsymbol{C}$
Find relays on the path (P_{MHC}) using Dijkstra algorithm.

---

node n_r; otherwise $\boldsymbol{C}(n_t, n_r) = 0$. Using the connectivity matrix, we build the graph between nodes. We do a standard run of the Dijkstra algorithm with the equal cost for each link, and the shortest path is defined as the path with the least cost.
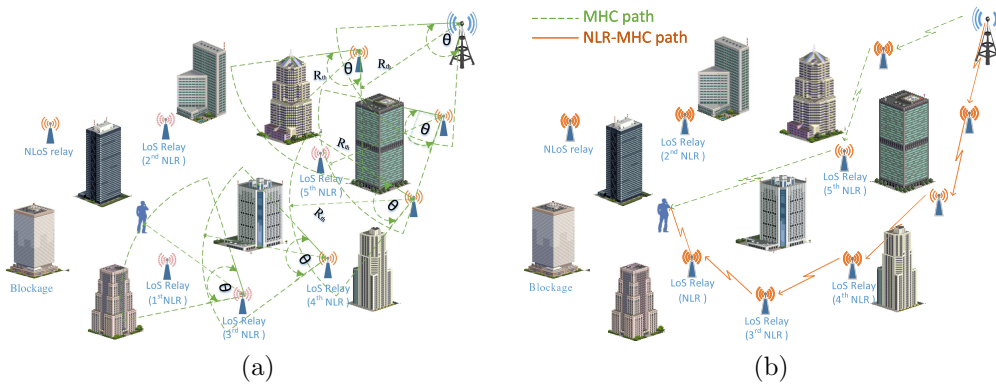
Figure 5.1: An illustration of selecting the path between the source and destination.

5.3.2 NLR-MHC Technique

Here, we propose a flexible relay routing technique by relaxing the minimum hop count. The proposed technique selects the nearest LoS relay (NLR) to the destination on the sector directed at the source. In the DF protocol, a relay can retransmit the signal if its received SNR is greater than or equal to γ_{th}. Hence, the coverage probability of the last link between the NLR and destination represents the coverage probability of the link between source and destination as will be discussed in section 5.5. As such, the idea of controlling the sector size through the deviation angle θ is to manage the distance between the NLR with both the source and destination. For instance, decreasing θ renders the NLR closer to the source, hence, the hop count decreases. On the other hand, limiting the sector size is equivalent to decreasing the density of relays. As a result, the NLR will become farther away from the destination. Hence, the coverage probability lessens due to the increase in the distance between the NLR and destination. The proposed routing technique can be summarized as in Algorithm 5.2.

Algorithm 5.2: Pseudo-code for NLR-MHC Routing technique.

Input: $(N_R, N_L, M_R, M_L, M_S, M_D, \gamma_{th}, \theta)$,
Output: (P_{NLR});
N_R and $N_L \rightarrow$ Number of relays and blockages.
M_R, M_L, M_S and $M_D \rightarrow$ Positions of relays, blockages, source, and destination.
Sector radius $R_{th} = (\frac{P(G)^2}{A\ N_0\gamma_{th}})^{\frac{1}{\alpha}}$.
Find the NLR to the destination on the sector directed at source.
for *Each transmitting node (relay/source)* $n_t = 1$ **to** $N_R + 1$ **do**
   for *Each receiving node (relay)* $n_r = 1$ **to** N_R *and* $n_t \neq n_r$ **do**
      Create line L between transmitting node n_t and receiving node n_r
      Find the number of intersection points N_B between L and all blockages;
      if $(N_B = 0)$ **then**
         Compute distance d_{n_t,n_r} between transmitting node and receiving node.
         Compute angle φ between the two vectors which represent the link
          from source/relay n_t to relay n_r and the link from source/relay n_t to
          the NLR.
         if $(\varphi \leq \theta/2)\&(d_{n_t,n_r} \leq R_{th})$ **then**
           $\boldsymbol{C}(n_t, n_r) = 1$
         else
           $\boldsymbol{C}(n_t, n_r) = 0$

Construct the graph G using connectivity matrix $\boldsymbol{C}$.
Find the path (P_{NLR}) using Dijkstra algorithm between source and NLR.

In Fig. 5.1.b, the solid and the dashed lines depict the NLR-MHC and the MHC paths

from the source to destination, respectively. Fig. 5.1.b shows one realization of network setting scenario where the fifth NLR is selected for the MHC routing technique for a path with three hops, whereas the NLR-MHC technique selects the first NLR which results in a path with total of six hops, hence higher number of hops.

5.4   Modeling Hop Count Distribution

In this section, we propose a mathematical framework for the performance evaluation of the two underlying routing techniques. The proposed framework comprises modeling the routing process as a Markov stochastic process with the phase-type distribution. This distribution was introduced in [84], described by a random variable generated by one or more Markov stochastic process(es). It is known that the phase-type distribution is a family of discrete and continuous probability distributions. The continuous distribution describes the time until reaching the absorbing state while the discrete distribution characterizes the number of states until reaching the absorbing state [80]. The phase-type distribution has favorable characteristics and can approximate any positive distribution which can reduce the difficulty of analysis and modeling [85]. Our representation of a phase-type distribution for the two routing techniques is shown in Fig. 5.2. Recall in chapter 3, each transient state can be characterized by three parameters: transition probabilities to the next state, the absorbing state, and the outage state. In the context of the routing process in mmWave networks, transitions through the ordered transient states could correspond to transmit data through relays. The number of states from the commencement (source) of the process until moving into the absorbing state (destination) is referred to as the hop count of the path.

5.4.1   Phase-type Distribution Parameters

We derive the parameters of the phase-type distribution which represent the transition probability from the current state to the next state. Firstly, we have obtained the transition probabilities from the current state to the next state, the absorbing state, and the outage state in Section 3.3 for the MHC routing technique. In that, p_{out} and $P_{LoS,k}^{MHC}$ are defined as

$$p_{out} = exp\Big(-\frac{\theta\lambda_R}{\beta^2}\ \Gamma(2,\ \beta(\frac{C}{\gamma_{th}})^{1/\alpha})\Big), \tag{5.1}$$

(a) MHC technique
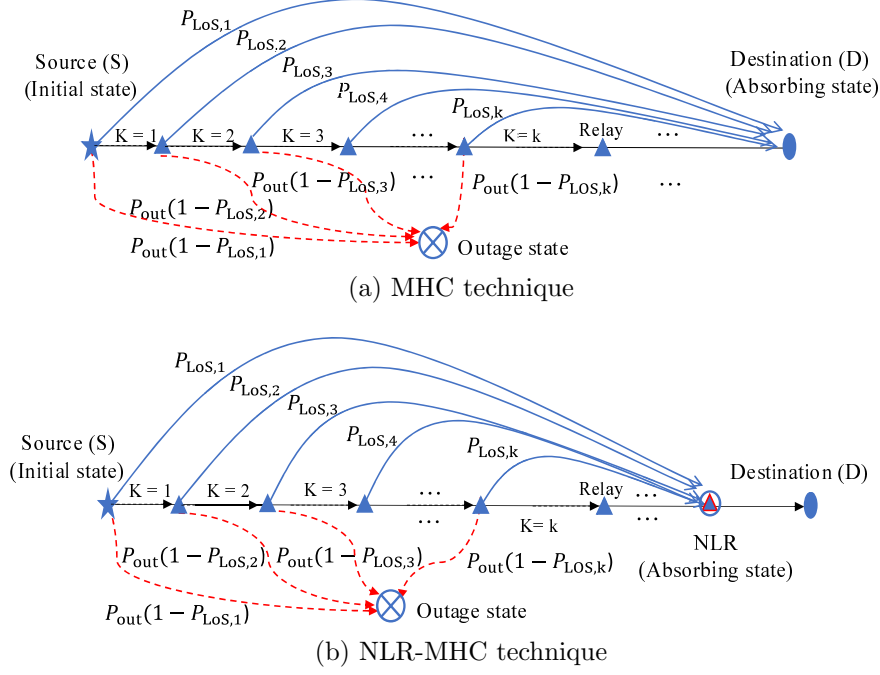
(b) NLR-MHC technique

Figure 5.2: Representation of (K)-state Markov process with a phase-type distribution for two routing techniques.

$$P_{LoS,k}^{MHC} = \begin{cases} e^{-\beta\ d_{SD}} & \text{if } k = 1 \\ 1 - e^{-\mho\ \Lambda_A(r)}, & \text{if } k > 1 \end{cases}. \tag{5.2}$$

For the NLR-MHC technique, the absorption probability $P_{LoS,k}$ is defined as the probability of NLR being on the sector of the current source/relay. To obtain this probability, we exploit the distance distribution between the NLR and destination which is derived based on the density of LoS relays with the destination,

$$\Lambda_A(r_{RD}) = \int_{-\theta/2}^{\theta/2} \int_0^{r_{RD}} e^{-\beta x}\ \lambda_R x\ dx\ d\phi = \frac{\theta \lambda_R}{\beta^2}\left(1 - \beta\ r_{RD}\ e^{-\beta r_{RD}} - e^{-\beta r_{RD}}\right). \tag{5.3}$$

Using the density of LoS relays and void probability [53], the CDF of the distance between the NLR and the destination is given by

$$F_{NLR}(r_{RD}) = 1 - e^{-\Lambda_A(r_{RD})}. \tag{5.4}$$

Then, the PDF of the distance between the destination and NLR can be formulated as

$$f_{NLR}(r_{RD}) = \theta\ \lambda_R\ r_{RD} \times exp\left[-\beta\ r_{RD} - \frac{\theta\ \lambda_R}{\beta^2}(1 - \beta\ r_{RD}\ e^{-\beta\ r_{RD}} - e^{-\beta\ r_{RD}})\right]. \tag{5.5}$$

One should notice that the absorption probability depends on the distance r_{RD} from the NLR to the destination where the relation between r_{RD} and $r_{k,k-1}$ for a given d_{k-1} is expressed by

$$r_{k,k-1} = \sqrt{r_{RD}^2 + {d_{k-1}}^2 - 2\ d_{k-1}\ r_{RD}\ cos(\phi)}. \tag{5.6}$$

For given angle ϕ and distance between the NLR and current source/relay, the absorption probability for the NLR-MHC $P_{LoS,k} = e^{-\beta \ r_{k,k-1}}$. For all possible locations of relays with SNR $\geq \gamma_{th}$ in the sector area A_s, the absorption probability using the distance distribution of the NLR is given by

$$P_{LoS,k}^{NLR} = \frac{1}{\theta} \iint_{A_s} e^{-\beta r_{k,k-1}} f_{NLR}(r_{RD}) \ dr_{RD} \ d\phi. \tag{5.7}$$

5.4.2 Probability Distribution of Hop Count

The parameters of two routing techniques in Fig. 5.2 are obtained in (5.1), (5.2) and (5.7). Therefore, the hop count distributions for the two routing techniques can be represented in matrix notation using three parameters; absorption vector, intermediate probability matrix, and initial transient vector. First, the absorption vector T^l which includes the absorption probability $P_{LoS,k}^l$ is expressed as follows:

$$T^l = \left[P_{LoS,1}^l, P_{LoS,2}^l, \ldots, P_{LoS,K_{max}}^l \right], \tag{5.8}$$

where $l \in \{MHC, NLR\}$, and K_{max} indicates the number of states which can be used as hop count constraint. The intermediate probability matrix $Q_{K_{max}}^l$ for the routing process represents the probabilities of transition between relays, given by

$$Q_{K_{max}}^l = \begin{pmatrix} 0 & p_1^l & 0 & \ldots & 0 \\ 0 & 0 & p_2^l & \ldots & 0 \\ \ddots & \ddots & \ddots & \ddots & \ddots \\ 0 & 0 & 0 & \ldots & p_{K_{max}}^l \\ 0 & 0 & 0 & \ldots & 0 \end{pmatrix}, \tag{5.9}$$

where p_k^l denotes the transition probability from relay $k-1$ to relay k, given by

$$p_k^l = (1 - P_{LoS,k+1}^l)(1 - p_{out}). \tag{5.10}$$

Let ρ denotes a vector of probabilities defining the initial transient state, given by

$$\rho = [1, 0, \ldots, 0]. \tag{5.11}$$

For the MHC technique, we find the hop count distribution conditioned on the existence of a path between the source and destination (number of available paths $N_{path} > 0$). The hop count distribution is defined as follows

$$f_K^{MHC}(k) = P(K = k | N_{path} > 0) = \frac{f_{DPH}(k)}{\sum_{k=0}^{K_{max}} f_{DPH}(k)}, \tag{5.12}$$

where f_{DPH} is the PDF of discrete phase-type variable with parameters $Q_{K_{max}}, \rho$ and T, and it can be formulated as

$$f_{DPH}(k) = \rho \ (Q_{K_{max}})^{k-1} \ T. \tag{5.13}$$

According to (5.12) and (5.13), the hop count distribution can be expressed by

$$f_K^{MHC}(k) = \frac{\rho \ (Q_{K_{max}}^{MHC})^{k-1} \ T^{MHC}}{\sum_{k=1}^{K_{max}} \rho \ (Q_{K_{max}}^{MHC})^{k-1} \ T^{MHC}} \qquad for \ \ k \geq 1. \tag{5.14}$$

For the NLR-MHC technique, as shown in Fig. 5.2.b, the NLR is considered as an absorption state, where it should decode the data correctly i.e., $\gamma_{NLR} \geq \gamma_{th}$. As such, the hop count distribution of the NLR-MHC technique is calculated as

$$f_K^{NLR}(k) = P(K = k | N_{path} > 0) = \frac{\rho \ (Q_{K_{max}}^{NLR})^{k-2} \ T^{NLR}}{\sum_{k=2}^{K_{max}} \rho \ (Q_{K_{max}}^{NLR})^{k-2} \ T^{NLR}} \ \ for \ \ k \geq 2. \tag{5.15}$$

In the following, we investigate the asymptotic behavior of increasing the relay density for the hop count distribution. In that, the hop count distribution mainly depends on the outage probability at each state p_{out} and the absorption probability $P_{LoS,k}^l$. At high relay density, the outage probability in (5.1) converges to zero. Furthermore, for large deviation angle, the absorption probability between relays and the destination defined in (5.2) converges to one for the MHC technique. Given the representation of the phase-type distribution depicted in Fig. 5.2.a, the asymptotic hop count distribution for the MHC technique in (5.14) can be expressed as

$$f_K^{MHC}(k) = \begin{cases} e^{-\beta \ d_{SD}} & \text{if } k = 1 \\ (1 - e^{-\beta \ d_{SD}}) & \text{if } k = 2 \end{cases}. \tag{5.16}$$

Thus, the asymptotic value for the average hop count becomes $2 - e^{-\beta \ d_{SD}}$. Similarly, for the NLR-MHC technique, the asymptotic hop count distribution in (5.15) can be computed as

$$f_K^{NLR}(k) = P_{LoS,k-1}^{NLR} \times \sum_{u=1}^{k-2} (1 - P_{LoS,u}^{NLR}) \ \ for \ \ k \geq 2. \tag{5.17}$$

5.4.3 Connectivity Probability

The connectivity probability p_{con} is a metric used to measure the network connectivity. In particular, it is defined as the probability that the destination connects to the source through LoS link(s) [15, 61]. From the representation of the phase-type distribution depicted in Fig. 5.2, one can determine the connectivity probability for the MHC and NLR-MHC techniques respectively, as

$$p_{con}^{MHC} = \sum_{k=1}^{K_{max}} \rho \ (Q_{K_{max}}^{MHC})^{k-1} T^{MHC} \ \ for \ \ k \geq 1. \tag{5.18}$$

$$p_{con}^{NLR} = \sum_{k=2}^{K_{max}} \rho \ (Q_{K_{max}}^{NLR})^{k-2} T^{NLR} \ \ for \ \ k \geq 2. \tag{5.19}$$

5.5 Coverage Probability and Spectral Efficiency

Here, we assess the network performance of the two routing techniques in-terms of the coverage probability and spectral efficiency. First, the coverage probability is defined as the probability of the destination to receive the signal with SNR $\geq \gamma_{th}$. The multi-hop DF channel is modeled as a single hop whose output SNR $\gamma_{s,d}$ is approximated as [86]

$$\gamma_{s,d} = \min_{j=1,...k} \gamma_j, \tag{5.20}$$

where k is the number of links in the path, and γ_j is the SNR for each link. For the DF protocol, relays can re-transmit the signal if the received SNR $\geq \gamma_{th}$. Hence, all received SNR values at the relays of the selected path should satisfy the condition $\gamma_j \geq \gamma_{th}$ except for the final link between the relay and destination. As a result, the coverage probability of the path from the destination to source is equivalent to the coverage probability for the link between the last relay and destination, given by

$$P_{Cov} = P(\gamma_{s,d} \geq \gamma_{th}) = P(\gamma_1 \geq \gamma_{th}, \gamma_2 \geq \gamma_{th}, .., \gamma_k \geq \gamma_{th}) = P(\gamma_k \geq \gamma_{th}) \tag{5.21}$$

In our analysis, we investigate the performance of the two underlying routing techniques in-terms of their achieved spectral efficiency defined for the selected path between the destination to source. In that, we adopt a fixed rate transmission scheme that works as follows: If the SNR of a link is equal or above the SNR threshold γ_{th}, the link can be successfully used for information transmission at spectral efficiency $log_2(1 + \gamma_{th})\ bps/Hz$. As such, the spectral efficiency can be expressed similar to $[1, 2, 87]$ as

$$\tau(\gamma_{th}) = 0.5 \times log_2(1 + \gamma_{th})P(\gamma_{s,d} \geq \gamma_{th}) = 0.5 \times log_2(1 + \gamma_{th})P(\gamma_k \geq \gamma_{th}). \tag{5.22}$$

where the factor of 0.5 is due to frequency reuse of order two.

5.5.1 MHC Routing Technique

In what follows, we derive the coverage probability for the MHC routing technique based on hop count distribution. We firstly study the connection between the destination to source through relays, and then we consider the direct link ($K = 1$).

Lemma 5.1. *The distance distribution of the final link between the destination and the last relay on the path for the MHC routing technique is given by*

$$f_R(r|K > 1) = \frac{\sqrt{\lambda_R}r}{\sum_{k=1}^{K_{max}} \rho\ (Q_{K_{max}}^{MHC})^k\ T^{MHC}} \times \sum_{k=2}^{K_{max}} \rho\ (Q_{K_{max}}^{MHC})^{k-1}\ T^{MHC}\ \frac{e^{-\pi\lambda_R(d_k-r)^2}}{\sqrt{d_k}}. \tag{5.23}$$

Proof. According to *Poisson law*, the probability that a circle with radius d_k contains

exactly n relays is defined as

$$P(N = n) = \frac{(\pi \lambda_R d_k^2)^n}{n!} e^{-\pi \lambda_R d_k^2}. \tag{5.24}$$

Let r_n be the distance between the destination and the nth nearest relay given hop count k, hence, the PDF of the distance r_n is given by [53]

$$f_{r_n}(r|K = k \neq 1, N = n) = 2\pi \lambda_R r \frac{(\pi \lambda_R r^2)^{(n-1)}}{(n-1)!} e^{-\pi \lambda_R r^2}. \tag{5.25}$$

Given the average distance d_k between the destination and relay k in (3.8), one can find the probability of having n relays in a circle centered at destination with radius d_k. Therefore, the final link distance distribution for the MHC technique can be derived as

$$
\begin{aligned}
f_R(r|K > 1) &= \sum_{k=2}^{K_{max}} f_K^{MHC}(k) \sum_{n=1}^{\infty} f_R(r|K = k, N = n) \, P(N = n) \\
&= \sum_{k=2}^{K_{max}} f_K^{MHC}(k) \sum_{n=1}^{\infty} \frac{2\pi \lambda_R r (\pi \lambda_R r^2)^{n-1}}{(n-1)!} e^{-\pi \lambda_R r^2} \times \frac{(\pi \lambda_R (d_k)^2)^{n-1}}{(n-1)!} e^{-\pi \lambda_R d_k^2} \\
&= \sum_{k=2}^{K_{max}} f_K^{MHC}(k) \, 2\pi \lambda_R \, r \, e^{-\pi \lambda_R (r^2 + d_k^2)} \times \sum_{n=1}^{\infty} \frac{(\pi \, \lambda_R \, d_k r)^{2(n-1)}}{((n-1)!)^2}.
\end{aligned}
\tag{5.26}
$$

Note that the inner summation over n is a Riemann sum derived in [88], and given by

$$\sum_{n=1}^{\infty} \frac{(\pi \lambda_R d_k r)^{2(n-1)}}{((n-1)!)^2} = \frac{1}{2\pi \sqrt{\lambda_R d_k r}} e^{(2\pi \lambda_R d_k r)}. \tag{5.27}$$

Therefore, according to (5.26) and (5.27), the distance distribution of the final link is given by

$$f_R(r|K > 1) = \sum_{k=2}^{K_{max}} f_K^{MHC}(k) \, \lambda_R r \, \frac{e^{-\pi \lambda_R (d_k - r)^2}}{\sqrt{\lambda_R r d_k}}. \tag{5.28}$$

Substituting (5.14) in (5.28) leads to the final expression in Lemma 5.1. $\qquad \square$

For the direct connection ($K = 1$), the source directly connects to the destination with distance d_{SD}. Therefore, the distance distribution of the last link on the path for the MHC technique accounting for both cases ($K = 1$) and ($K > 1$) is determined as

$$f_R(r) = f_R(r|K > 1) + f_K^{MHC}(1) \times \delta(r - d_{SD}), \tag{5.29}$$

where $\delta(r - d_{SD})$ is the Dirac delta function. Using the distance distribution of the last link, we derive the coverage probability for the MHC technique. Let $W = (PG)/(N_0 A r^\alpha)$ denotes the SNR in the absence of shadowing effect. For the case ($K > 1$), the CDF of W is obtained by substituting the last link distance r with W to give

$$F_W(w|K > 1) = P\Big(\frac{P\,G}{N_0\,A\,r^\alpha} < w \Big| K > 1\Big) = 1 - F_R\Big(\Big[\frac{P\,G}{N_0\,A\,w}\Big]^{1/\alpha}\Big|K > 1\Big), \tag{5.30}$$

and hence,

$$f_W(w|K > 1) = \frac{(P\,G)^{1/\alpha}}{\alpha\,w(N_0\,A\,w)^{1/\alpha}} f_R\Big(\Big[\frac{P\,G}{N_0\,A\,w}\Big]^{1/\alpha}\Big|K > 1\Big). \tag{5.31}$$

Given that the shadowing (χ) and the SNR in the absence of shadowing effect (W) are

independent random variables, hence,

$$f_{W,\chi}(w, \chi) = f_\chi(\chi) \times f_W(w). \tag{5.32}$$

Note that the log-normal distribution χ with zero mean has the same distribution of log-normal distribution $1/\chi$. Hence, the PDF of the SNR with shadowing can now be obtained by substituting W, χ with ζ_1, ζ_2 using $\zeta_1 = W \times \chi$ and $\zeta_2 = W/\chi$. Hence, the random variables ζ_1 and ζ_2 have the same distribution. After mathematical manipulations, the joint PDF of the SNR for $K > 1$ is defined as

$$f_{\zeta_1,\zeta_2}(\zeta_1, \zeta_2) = \frac{f_{W,\chi}(\sqrt{\zeta_1 \times \zeta_2}, \sqrt{\frac{\zeta_1}{\zeta_2}})}{2\zeta_1} = \frac{M_{kh}}{\zeta_1^{\frac{3}{4\alpha}+0.5}\zeta_2^{\frac{3}{4\alpha}+1}} \sum_{k=2}^{K_{max}} \frac{\rho\,(Q_{K_{max}}^{MHC})^{k-1}\,T^{MHC}}{\sqrt{d_k}}$$

$$\times \exp\left(-\pi\lambda_R\left(d_k - \left(\frac{\mathscr{J}}{\sqrt{\zeta_1\zeta_2}}\right)^{\frac{1}{\alpha}}\right)^2 - \frac{(10log(\sqrt{\frac{\zeta_1}{\zeta_2}}))^2}{2\sigma^2}\right), \tag{5.33}$$

where $\mathscr{J} = (P\,G)/(N_0\,A)$ and M_{kh} is given by

$$M_{kh} = \frac{10\,log(e)\mathscr{J}^{\frac{3}{2\alpha}}\sqrt{\lambda_R}}{\sqrt{2\pi}\,\sigma \times 2\,\alpha \sum_{k=1}^{K_{max}} \rho\,(P_{K_{max}}^{MHC})^{k-1}\,T^{MHC}}. \tag{5.34}$$

Then, the coverage probability for the direct link between the source and destination $(k = 1)$ is derived as follows

$$P_{Cov}(k = 1) = P\big(SNR > \gamma_{th}\big) = P\Big(\frac{P\,G\,\chi}{N_0\,A\,d_{sd}^\alpha} > \gamma_{th}\Big)$$

$$= P\Big(\chi > \frac{\gamma_{th}\,d_{sd}^\alpha}{\mathscr{J}}\Big) = \mathscr{Q}\Big(\frac{10\,log(\frac{\gamma_{th}d_{sd}^\alpha}{\mathscr{J}})}{\sigma}\Big), \tag{5.35}$$

where $\mathscr{Q}(.)$ is the cumulative distribution function of the standard normal distribution. Finally, the coverage probability of the MHC technique is expressed as

$$P_{Cov}^{MHC}(\gamma_{th}) = P(\gamma_{S,D} \geq \gamma_{th}) = P_{Cov}(k = 1) \times P(K = 1) + P_{Cov}(k > 1) \times P(K > 1)$$

$$= \rho T^{MHC}\,\mathscr{Q}\Big(\frac{10\,log(\frac{\gamma_{th}d_{sd}^\alpha}{\mathscr{J}})}{\sigma}\Big) + \int_{\gamma_{th}}^{\infty}\int_0^{\infty} f_{\zeta_1,\zeta_2}(\zeta_1, \zeta_2)\,d\zeta_1\,d\zeta_2.$$

$$\tag{5.36}$$

5.5.2 NLR-MHC Routing Technique

The coverage probability of the NLR-MHC technique depends on the density of LoS relays available with the destination, and these LoS relays form non-homogeneous PPP. In the following theorem, we derive the coverage probability for the NLR-MHC technique.

Theorem 5.1. *The probability that the SNR at the destination for the NLR-MHC routing technique is greater than or equal to a predefined threshold γ_{th} is given by*

$$p_{cov}^{NLR}(\gamma_{th}) = 1 - e^{-\Lambda_{NLR}(\gamma_{th})}, \tag{5.37}$$

with

$$\Lambda_{NLR}(\gamma_{th}) = \frac{\theta\lambda_R}{\beta^2}\Bigg[1 - \mathscr{L}\Big(\beta\,(\frac{\mathscr{J}}{\gamma_{th}})^{\frac{1}{\alpha}}, \frac{1}{\sqrt{2}\alpha e_g}\Big) - \beta\,e^{(2\alpha e_g)^{-2}}\Big(\frac{\mathscr{J}}{\gamma_{th}}\Big)^{\frac{1}{\alpha}}$$

$$\times \mathscr{L}\Big(\beta\,(\frac{\mathscr{J}}{\gamma_{th}})^{\frac{1}{\alpha}}e^{\frac{1}{2(\alpha e_g)^2}}, \frac{1}{\sqrt{2}\alpha e_g}\Big)\Bigg], \tag{5.38}$$

where $\mathscr{L}(.,.)$ is the Laplace transform of the log-normal distribution, and $e_g = \frac{10log_{10}(e)}{\sqrt{2}\sigma}$.

Proof. We transform the two dimensional PPP of the distances between relays and destination into one dimensional PPP of corresponding SNR without shadowing using the Mapping theorem [53]. In doing so, we define the SNR without shadowing as $w = (PG)/(N_0 A r^\alpha) = \mathscr{J}\,r^{-\alpha}$, and hence, its density is given by

$$\lambda_A(w) = \frac{\theta\lambda_R}{\alpha}\,\mathscr{J}^{\frac{2}{\alpha}}e^{-\beta\,(\mathscr{J}/w)^{\frac{1}{\alpha}}}w^{\frac{-2}{\alpha}-1}. \tag{5.39}$$

It is to be noted that to consider the shadowing effect χ in the SNR for the link between the destination and LoS relays, $\gamma = w \times \chi$, LoS relay points are displaced independently according to log-normal distribution in one dimensional PPP. The displaced points form a PPP by applying the displacement theorem [53]. The resulting density after displacement can be obtained as

$$\lambda(\gamma) = \int_0^\infty \lambda_A(w)\,\rho(w,\gamma)\,dw, \tag{5.40}$$

where the displacement kernel $\rho(w,\gamma)$, which represents the probability density function of γ as a function of w and γ, derived as

$$\rho(w,\gamma) = \frac{d}{d\gamma}P\big(w \times \chi < \gamma\big) = \frac{d}{d\gamma}\big(F_\chi(\frac{\gamma}{w})\big) = \frac{1}{w}f_\chi(\frac{\gamma}{w}). \tag{5.41}$$

Therefore, the intensity of LoS relays which achieve SNR $\geq \gamma_{th}$ can be derived as follows

$$\Lambda_{NLR}(\gamma_{th}) = \int_{\gamma_{th}}^\infty \lambda(\gamma)\,d\gamma = \frac{\theta\lambda_R}{\alpha}\,\mathscr{J}^{\frac{2}{\alpha}}\int_{\gamma_{th}}^\infty\int_0^\infty e^{-\beta\,(\frac{\mathscr{J}}{w})^{\frac{1}{\alpha}}}w^{\frac{-2}{\alpha}-2}f_\chi(\frac{\gamma}{w})\,dw\,d\gamma$$

$$= \frac{\theta\lambda_R\,10log(e)\,\mathscr{J}^{\frac{2}{\alpha}}}{\sqrt{2\pi}\sigma\alpha}\int_{\gamma_{th}}^\infty\int_0^\infty \frac{w^{\frac{-2}{\alpha}-1}}{\gamma}e^{\Big(-\beta\,(\frac{\mathscr{J}}{w})^{\frac{1}{\alpha}}-\frac{(10log(\gamma/w))^2}{2\sigma^2}\Big)}\,dw\,d\gamma$$

$$= \frac{\theta}{2\alpha}\,\lambda_R\,\mathscr{J}^{\frac{2}{\alpha}}\int_0^\infty e^{-\beta\,(\frac{\mathscr{J}}{w})^{\frac{1}{\alpha}}}w^{\frac{-2}{\alpha}-1}\,erfc\,\Big(\frac{10log(\gamma_{th}/w)}{\sqrt{2}\sigma}\Big)\,dw \tag{5.42}$$

$$\overset{v=\Big(\frac{10log(\gamma_{th}/w)}{\sqrt{2}\sigma}\Big)}{\Longrightarrow}\frac{\theta}{2\alpha\,e_g}\,\lambda_R\,\Big(\frac{\mathscr{J}}{\gamma_{th}}\Big)^{\frac{2}{\alpha}}\int_{-\infty}^\infty e^{-\beta\,(\frac{\mathscr{J}}{\gamma_{th}}e^{v/e_g})^{\frac{1}{\alpha}}}e^{\frac{2v}{\alpha e_g}}\,erfc\,(v)\,dv,$$

$$\Lambda_{NLR}(\gamma_{th}) \overset{(a)}{=} \frac{\theta}{2\beta}\,\lambda_R\,\Big(\frac{\mathscr{J}}{\gamma_{th}}\Big)^{\frac{1}{\alpha}}\int_{-\infty}^\infty e^{-\beta\,(\frac{\mathscr{J}}{\gamma_{th}}e^{v/e_g})^{\frac{1}{\alpha}}}e^{\frac{v}{\alpha e_g}}\Big[\frac{-2}{\sqrt{\pi}}e^{-v^2} + \frac{1}{\alpha e_g}\,erfc\,(v)\Big]\,dv$$

$$\overset{(a)}{=} \frac{\theta}{2\beta}\,\lambda_R\,\Big(\frac{\mathscr{J}}{\gamma_{th}}\Big)^{\frac{1}{\alpha}}\Bigg[\int_{-\infty}^\infty e^{-\beta\,(\frac{\mathscr{J}}{\gamma_{th}}e^{v/e_g})^{\frac{1}{\alpha}}}e^{\frac{v}{\alpha e_g}}\frac{-2}{\sqrt{\pi}}e^{-v^2}\,dv + \frac{2}{\beta\,(\frac{\mathscr{J}}{\gamma_{th}})^{\frac{1}{\alpha}}} \tag{5.43}$$

$$-\frac{2/\sqrt{\pi}}{\beta\,(\frac{\mathscr{J}}{\gamma_{th}})^{\frac{1}{\alpha}}}\int_{-\infty}^\infty e^{-\beta\,(\frac{\mathscr{J}}{\gamma_{th}}e^{v/e_g})^{\frac{1}{\alpha}}}e^{v^2}\,dv\Bigg]$$

$$= \frac{\theta \lambda_R}{\beta^2} \left[1 - \mathscr{L} \left(\beta \, (\frac{\mathscr{J}}{\gamma_{th}})^{\frac{1}{\alpha}}, \frac{1}{\sqrt{2}\alpha e_g} \right) - \beta \, e^{(2\alpha e_g)^{-2}} \left(\frac{\mathscr{J}}{\gamma_{th}} \right)^{\frac{1}{\alpha}} \mathscr{L} \left(\beta \, (\frac{\mathscr{J}}{\gamma_{th}})^{\frac{1}{\alpha}} e^{\frac{1}{2(\alpha e_g)^2}}, \frac{1}{\sqrt{2}\alpha e_g} \right) \right],$$

where $erfc(.)$ is the complementary error function, and (a) is obtained using integration by parts, and $\mathscr{L}(.,.)$ is the Laplace transform of the log-normal distribution. Since a closed-form expression of the Laplace transform of the log-normal distribution does not exist, we use the approximation in [89]

$$\mathscr{L}(s, q) = \int_{-\infty}^{\infty} \frac{1}{\sqrt{2\pi}q} exp\left[-se^y - \frac{1}{2q^2}y^2 \right] dy \approx \frac{1}{\sqrt{1 + \mathscr{W}(sq^2)}} exp\left[\frac{-1}{2q^2}\mathscr{W}(sq^2)^2 - \frac{1}{q^2}\mathscr{W}(sq^2) \right],$$

(5.44)

where $\mathscr{W}(.)$ is the Lambert-W function. Using the active relay intensity in (5.43) and the void probability [53], the proof of Theorem 5.1 is completed. $\square$

5.6   Simulation Results

In this section, we present simulation results and numerical examples to shed light on the performance of the multi-hop mmWave networks for the two underlying routing techniques. We evaluate the performance in-terms of average hop count, connectivity probability, and spectral efficiency. Similar to [45] and [36], we consider the path-loss exponent $\alpha = 2$, $A = 69.8$ dB, and $\sigma = 5.2$ dB for the log-normal channel. We assume that buildings have length and width range of [10 m, 25 m], and [10 m, 20 m], respectively. The network is assumed to be operated at 73 GHz with a system bandwidth $BW = 2$ GHz. The transmit power of relays and sources $P = 30$ dBm, the thermal noise is given by $-174 + 10 \, log(B)$ dBm, and noise figure $= 10$ dB. The antenna gain for relays and sources $G = 15$ dB, and $K_{max} = 20$. All simulation results are averaged over 500×10^3 realizations, and the simulations consider a square area fixed to [1000 m×1000 m].

Fig. 5.3 depicts the outage probability per hop given in (5.1) for different relay densities, $\theta = \{80°, 180°, 360°\}$, $\gamma_{th} = \{25, \, 30\}$ dB, and blockage density $\lambda_B = 5 \times 10^{-5} \text{m}^{-2}$. It is shown that increasing the density of relays λ_R and deviation angle θ significantly decreases the outage probability at each state whereas the outage probability rises with increasing γ_{th}. An interesting observation from the results is that the current source/relay can search backward, (i.e., $\theta \geq 180°$), to avoid the blockages between the current state and destination.

In Fig. 5.4, we compare between the MHC and NLR-MHC routing techniques in-terms of the hop count distributions for different SNR thresholds and blockage densities.
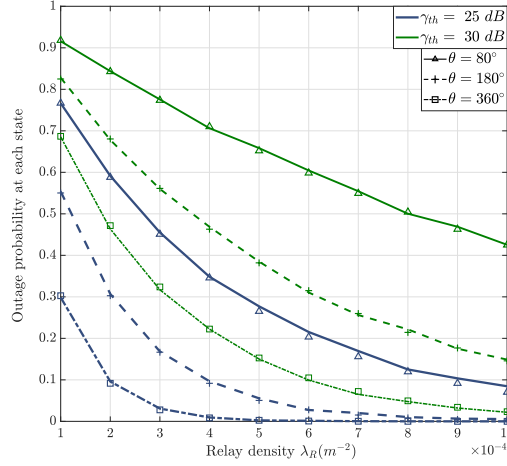
Figure 5.3: Outage probability at current state for different densities of relays, $\gamma_{th} = \{25, 30\}$ dB, $\theta = \{80°, 180°, 360°\}$, and $\lambda_B = 5 \times 10^{-5}$m^{-2}. Lines (solid and broken) and markers represent analytical and simulation results, respectively.

The system parameters are $\lambda_R = 2 \times 10^{-4}$m^{-2}, $d_{SD} = 300$ m, and $\theta = 120°$. One can notice that accuracy of our theoretical results when compared with simulations. It is observed that the hop count distribution of the MHC technique offers higher probability for small number of hops compared to the NLR-MHC technique. These results show how the selection of the NLR increases the mean and variance of the hop count distribution for the NLR-MHC technique. One can notice that increasing the blockage density from $\lambda_B = 1 \times 10^{-4}$m^{-2} to 2×10^{-4}m^{-2} significantly increases the required hop count between the destination and its source, especially for higher γ_{th}. Also, it is noted that the mean and variance of the hop count distribution reduce as γ_{th} decreases. This is due to the fact that reducing γ_{th} extends the sector radius, hence, the probability to find a path with lower hop count increases.

Fig. 5.5 shows the accuracy of analytical expressions in (5.36) and (5.37) for the coverage probability of the MHC and NLR-MHC routing techniques, respectively with $\lambda_B = \{1, 4\} \times 10^{-4}$m^{-2}, $\lambda_R = 2 \times 10^{-4}$m^{-2}, $d_{SD} = 300$ m, $\gamma_{th} = 20$ dB, and $\theta = 120°$. Results reveal the significant improvement in the coverage probability for the NLR-MHC compared to the MHC technique. Note that the impact of the blockage density on the two routing techniques are different. This can be interpreted as increasing the blockage density renders the NLR away from the destination for the NLR-MHC technique, hence, the coverage probability lessens. On the other hand, for the MHC routing technique, the hop count rises with increasing the blockage density to mitigate the impact of blockages which renders the last relay closer to the destination, leading to improved coverage probability.

(a) $\lambda_B = 1 \times 10^{-4} \text{m}^{-2}, \gamma_{th} = 15$ dB

(b) $\lambda_B = 1 \times 10^{-4} \text{m}^{-2}, \gamma_{th} = 20$ dB

(c) $\lambda_B = 2 \times 10^{-4} \text{m}^{-2}, \gamma_{th} = 15$ dB

(d) $\lambda_B = 2 \times 10^{-4} \text{m}^{-2}, \gamma_{th} = 20$ dB
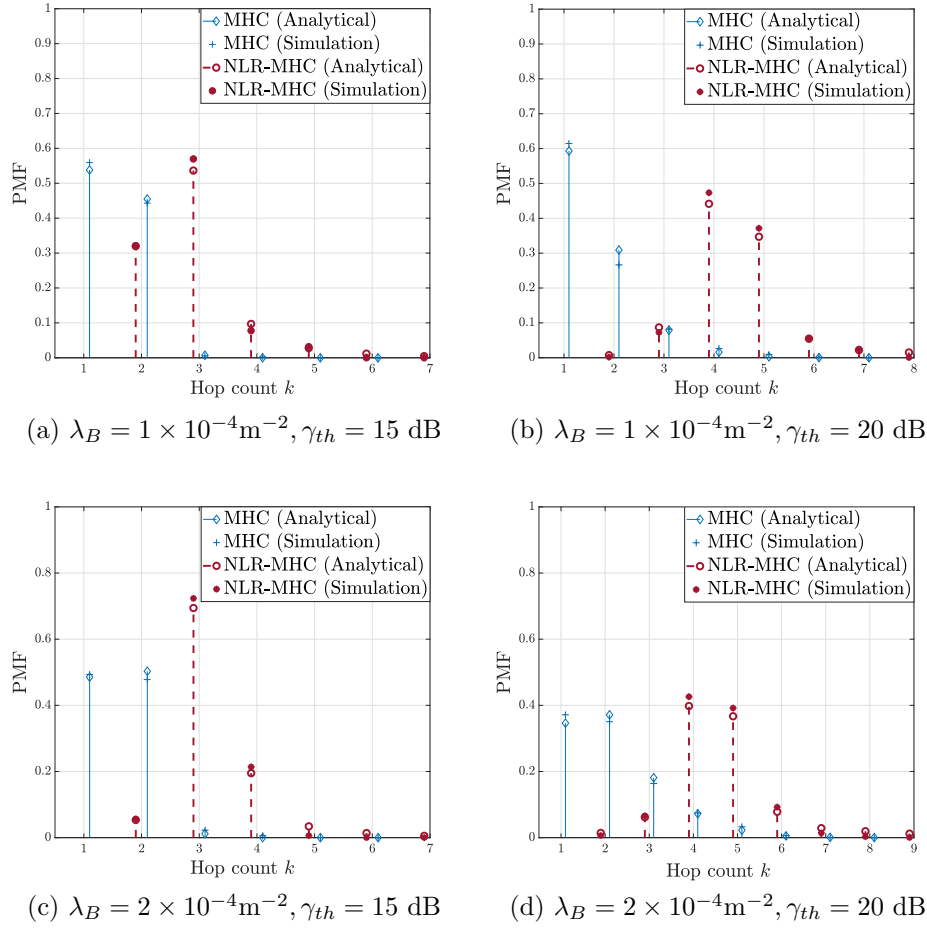
Figure 5.4: The hop count distribution of MHC and NLR-MHC techniques for different SNR thresholds and blockage densities with $\lambda_R = 2 \times 10^{-4} \text{m}^{-2}$, $d_{SD} = 300$ m, and $\theta = 120°$.

Fig. 5.6 shows the spectral efficiency results for the underlying routing techniques versus SNR thresholds using (5.22) for $d_{SD} = 300$ m, $\theta = 120°$, and different densities of blockages and relays. Indeed, the spectral efficiency is due to a product of two functions where the coverage probability is a decreasing function with SNR threshold, while the log function is an increasing function. Hence, it is quite obvious that the spectral efficiency is convex and reaches an optimal point at a certain SNR threshold. We can note that the spectral efficiency increases significantly in the MHC technique as the density of blockages rises. It is noticed that the spectral efficiency of the NLR-MHC technique improves as the density of relays gets higher, while it deteriorates for MHC technique. This can be interpreted as the higher the density of the relays, the shorter the distance between NLR and destination, hence, the spectral efficiency improves. On the contrary, increasing the relay density for the MHC technique rises the probability to reach relay which is near
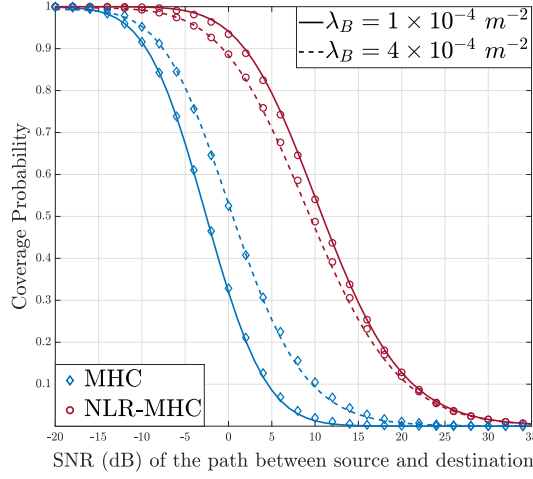
Figure 5.5: The coverage probability of the MHC and NLR-MHC techniques for different densities of blockages with $\lambda_R = 2 \times 10^{-4} \mathrm{m}^{-2}$, $\gamma_{th} = 20$ dB, $d_{SD} = 300$ m, and $\theta = 120°$. Lines (solid and broken) and markers represent analytical and simulation results, respectively.

to the source and has LoS connection with the destination. This leads to an increase in the distance between the last relay on the path and destination, hence, spectral efficiency deteriorates.

(a) $\lambda_R = 2 \times 10^{-4} m^{-2}$

(b) $\lambda_B = 4 \times 10^{-4} m^{-2}$
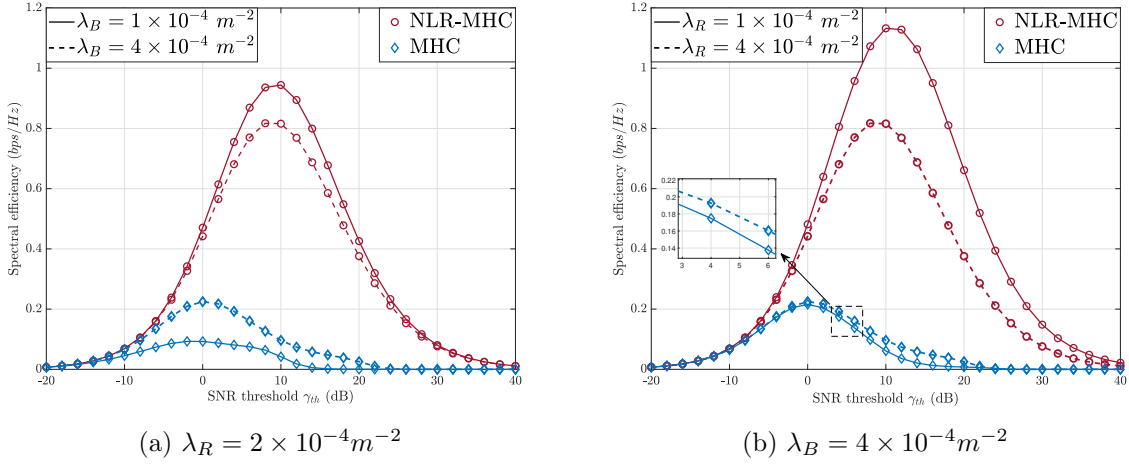
Figure 5.6: The spectral efficiency of the MHC and NLR-MHC techniques versus SNR threshold for different densities of (a) blockages and (b) relays with $d_{SD} = 300\ m$, and $\theta = 120°$.

For the sake of comparison, Fig. 5.7 plots the performance in-terms of spectral efficiency, connectivity probability, and average hop count for both the MHC and NLR-MHC routing techniques with $\theta = \{80°,\ 120°,\ 360°\}$ and different direct distances between the source and destination. The system parameters are $\lambda_R = 2 \times 10^{-4} \mathrm{m}^{-2}$, $\lambda_B = 4 \times 10^{-4} \mathrm{m}^{-2}$, and $\gamma_{th} = 20$ dB. Fig. 5.7.a shows that the NLR-MHC technique achieves high spectral ef-

ficiency compared to the MHC technique, and the difference in spectral efficiency increases as θ becomes higher. The reason is that higher values of θ reflects a shorter distance between NLR and destination for the NLR-MHC technique. For the MHC technique, as the deviation angle θ gets larger, the probability to find a LoS relay far from the destination increases, hence, the spectral efficiency decreases. Also, it is noticed that the spectral efficiency decreases as the direct distance becomes larger for the MHC technique, while it remains constant for the NLR-MHC technique. This is because the spectral efficiency for the NLR is independent of the direct link. The effect of the direct distance between the source and destination on the connectivity probability is illustrated in Fig. 5.7.b. As seen, the connectivity probability of the MHC technique outperforms the one of the NLR-MHC. This is due to the fact that the relay selection in the NLR-MHC technique reduces the number of available paths between the source and destination. It is noted that increasing the deviation angle significantly improves the connectivity probability, especially for the MHC technique. Also, the connectivity probability gap between the two routing techniques increases as the deviation angle gets higher. In Fig. 5.7.c, the average hop count is depicted versus the direct distance between the source and destination. As seen, the average hop count for the MHC technique outperforms the one for the NLR-MHC technique. It is also noteworthy that, a trade-off exists between the spectral efficiency, connectivity probability, and average hop count with a variation of θ in both underlying routing techniques.

(a) Spectral efficiency   (b) Connectivity probability   (c) Average hop Count
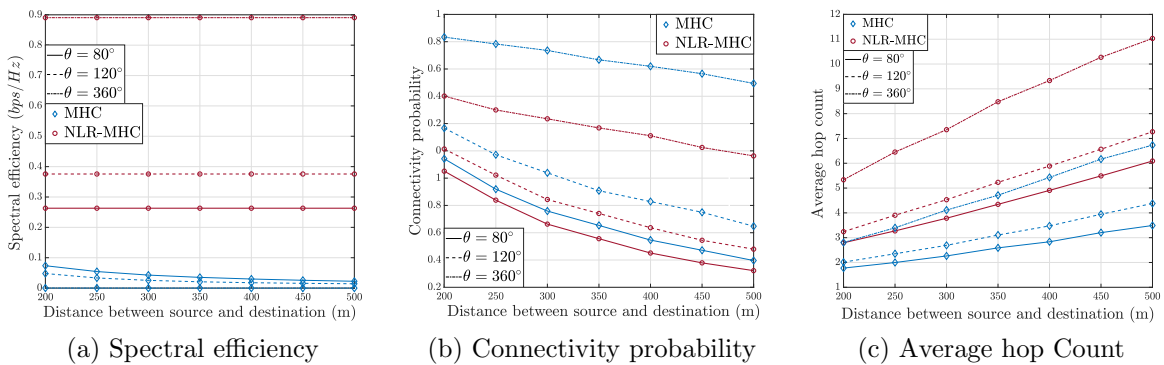
Figure 5.7: Comparison between the MHC and NLR-MHC techniques with $\lambda_R = 2 \times 10^{-4}\text{m}^{-2}$, and $\lambda_B = 4 \times 10^{-4}\text{m}^{-2}$ for different distances between the source and destination.

In Fig. 5.8, we show the performance in-terms of spectral efficiency, connectivity probability, and average hop count for the MHC and NLR-MHC routing techniques with $\gamma_{th} = \{10, 20\}$ dB and different relay densities. The system parameters are $d_{SD} = 300$

m, $\lambda_B = 4 \times 10^{-4} \mathrm{m}^{-2}$, and $\theta = 120°$. Fig. 5.8.a demonstrates that the spectral efficiency significantly increases as the relay density gets higher in the NLR-MHC technique. However, increasing relay density reduces the spectral efficiency of the MHC technique. It is noticed that the spectral efficiency of the MHC technique is very small compared to the NLR-MHC, and the difference increases as relay density rises. The effect of λ_R on the connectivity probability for different SNR thresholds is shown in Fig. 5.8.b. As seen from the results, the connectivity probability for the two routing techniques have similar behavior with increasing the relay density. Also, as γ_{th} increases, the connectivity probability significantly decreases. In Fig. 5.8.c, it is noticed that increasing the relay density decreases/increases the average hop count for the MHC/NLR-MHC techniques. The reason is that increasing relay density renders the NLR closer to the destination which leads to an increase in the number of hops. We illustrate as well the results for the asymptotic average hop count for high relay density. The obtained numerical results for the MHC technique show the tightness of the asymptotic expression for $\gamma_{th} = 10$ dB.

(a) Spectral efficiency (b) Connectivity probability (c) Average hop Count
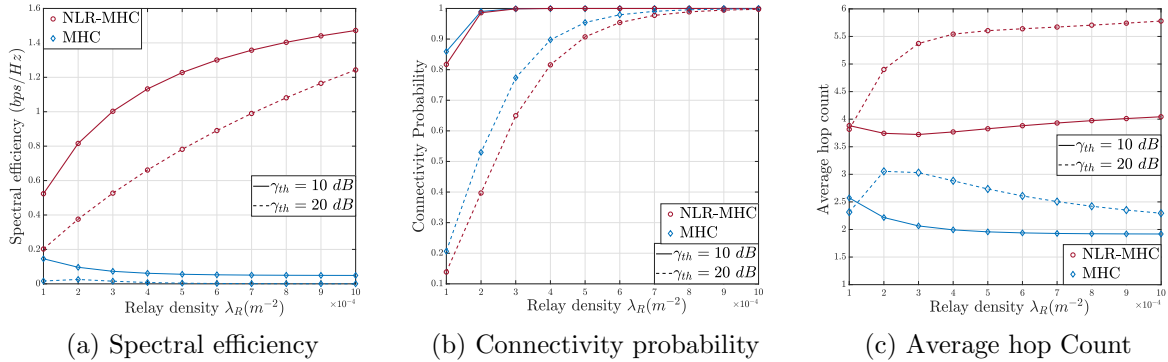
Figure 5.8: Comparison between the MHC and NLR-MHC techniques with $d_{SD} = 300$ m, $\lambda_B = 4 \times 10^{-4} \mathrm{m}^{-2}$, $\theta = 120°$, $\gamma_{th} = \{10, \ 20\}$ dB, and different relay densities.

Fig. 5.9 depicts the spectral efficiency and average hop count for the MHC and NLR-MHC techniques as a function of γ_{th} and θ for $\lambda_R = \lambda_B = 4 \times 10^{-4} \mathrm{m}^{-2}$. It is noticeable in Fig. 5.9.a that increasing θ results in improving the spectral efficiency of the NLR-MHC technique for different γ_{th}, and a reverse behavior is encountered for the MHC technique. It is also noticed that the MHC technique outperforms the NLR-MHC for small values of θ, and as θ increases, the NLR-MHC achieves a superior performance. Fig. 5.9.b shows a similar behavior of the average hop count for the MHC and NLR-MHC since both techniques aim at minimizing the number of hops between the destination and source and between source and the NLR, respectively. It is also shown that the average hop count of

the NLR-MHC technique increases with the deviation angle θ as the NLR becomes closer to the destination, but farther away from the source. Furthermore, the average hop count decreases as γ_{th} gets smaller due to the increased sector radius at smaller values of γ_{th}.

(a) Spectral efficiency
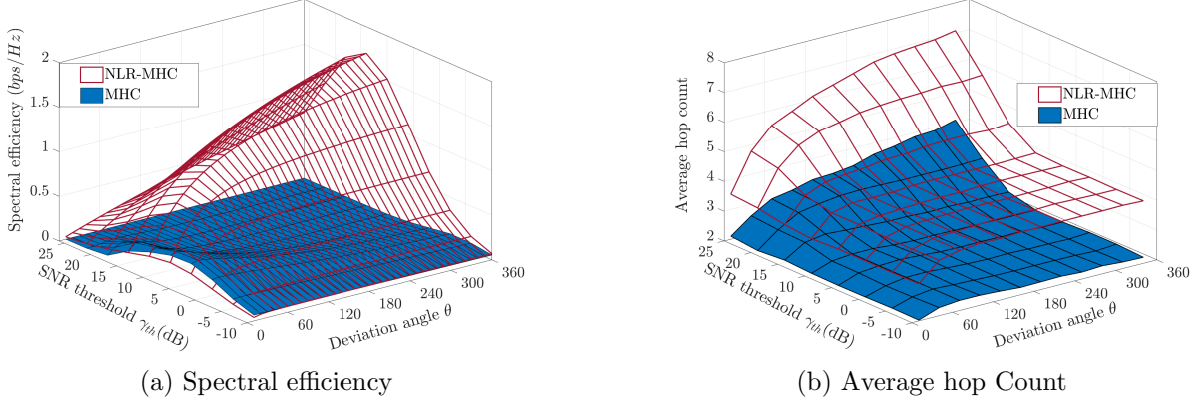
(b) Average hop Count

Figure 5.9: Spectral efficiency and average hop count of MHC and NLR-MHC techniques versus γ_{th} and θ with $\lambda_R = \lambda_B = 4 \times 10^{-4} \mathrm{m}^{-2}$.

Fig. 5.10 compares the MHC and NLR-MHC techniques in-terms of spectral efficiency and average hop count under various densities of relays and blockages. In each figure, we consider $\gamma_{th} = 15$ dB, and $\theta = 120°$. As one can observe, the relation between blockage density and spectral efficiency of the MHC follows the inverse trend for the NLR-MHC technique. As the blockage density increases, the spectral efficiency improves for the MHC technique, while it deteriorates with increasing the blockage density in the NLR-MHC technique. An interesting observation from the results is that the impact of relay density on the spectral efficiency is more significant compared to the blockage density for the NLR-MHC technique. It can be noticed that the average hop count rises as the blockage density increases for both routing techniques. As one can notice, the maximum hop count, on average, occurs at low relay densities when considering the MHC technique. However, this holds at a high density of relays for the NLR-MHC technique. It is noted from the figure that the NLR-MHC technique achieves higher spectral efficiency, while the MHC technique achieves lower average hop count.
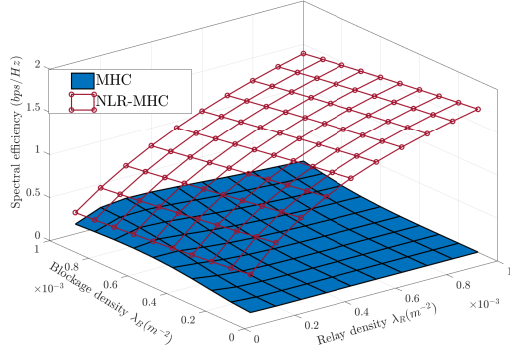
(a) Spectral efficiency
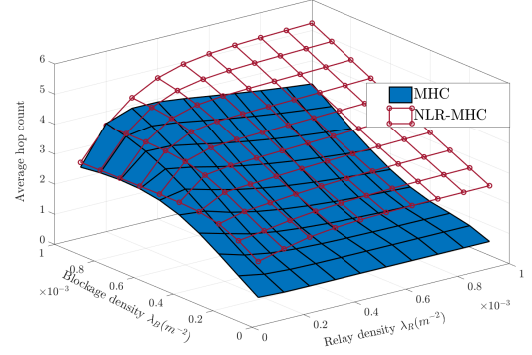
(b) Average hop Count

Figure 5.10: Spectral efficiency and average hop count of MHC and NLR-MHC routing techniques versus λ_R and λ_B with $\gamma_{th} = 15$ dB, and $\theta = 120°$.

5.7 Summary

In this chapter, we presented a novel mathematical framework for MHC and NLR-MHC routing techniques in multi-hop mmWave networks. Capitalizing on the proposed framework, analytical expressions for the hop count distribution, connectivity probability, and spectral efficiency have been obtained. Results have shown that NLR-MHC achieves a superior coverage probability and spectral efficiency compared to MHC. However, MHC provides better performance in-terms of connectivity probability and average hop count. It is shown that increasing the density of blockages deteriorates the spectral efficiency of the NLR-MHC technique. However, this leads to an unexpected improvement in the spectral efficiency of the MHC technique at the cost of increasing the hop count. It has been also shown that the deviation angle of the routing technique as well as the required signal-to-noise ratio threshold for decode and forward relays have a substantial impact on the performance of both routing techniques.

Chapter 6

Reliable Millimeter Wave Communication for IoT Devices

6.1 Introduction

5G and beyond networks experience a new era that will boost the efficiency of our lives and our business. This new era will lead to true device connectivity through the IoT where billions of devices, such as sensors, are connected among them and with the Internet [90]. According to Ericsson's mobility report, the 10.8 billion IoT devices of 2019 are expected to reach 24.9 billion by the end of 2025 [91]. This connectivity will be the foundation for increasingly intelligent mobility systems for new technologies such as smart manufacturing, telehealth, intelligent transportation, and smart homes. These future technologies are facing spectrum shortage challenges mainly due to the massive number of connections and the emerging bandwidth-hungry applications. MmWave communication represents one of the most effective solutions to this spectrum scarcity challenge motivated by the immense amount of bandwidth at mmWave bands.

To improve link reliability and extend the range of communications for IoT devices, the utilization of relays for mmWave communications is highly recommended. For network reliability, a relay selection algorithm is proposed in [92] according to the dependency between the source-destination and source-relay-destination links using geometric analysis. However, achieving high link reliability in mmWave relaying systems have not been compromised to support IoT applications. These applications depend mainly on battery-powered devices that will operate at low powers with a battery life of up to ten years in some applications. In [93], the authors showed that energy cost has critical importance in IoT devices because of the limited battery capacity. Indeed, radio communication at IoT devices significantly consumes higher than other components such as processor and memory as shown in [94]. As such, it is important to prolong the IoT device's battery life

by reducing power consumption due to communication.

In this chapter, we firstly adapt the relay selection technique of the previous chapter based on the nearest LoS relay (NLR) to IoT devices for mmWave relaying systems. The property of the NLR selection technique is that it consumes significantly less power than other links for IoT devices. This is because the IoT device needs to cover a much shorter distance to reach the NLR than to reach other relays. Also, the adapted technique is an adaptive and flexible relay selection by controlling the order of the NLR and limiting the relay-selected region. Secondly, we analytically derived the connectivity probability for the adapted technique, and we address the impact of limiting relay-selected region and order of NLR on network connectivity for IoT devices. Thirdly, we analyze the power consumption of IoT devices and show the trade-off between energy consumption and reliability of the IoT network under the proposed technique.

6.2 System Model

We consider a mmWave relaying system that consists of multiple IoT devices, their assigned BS, and a set of relays as shown in Fig. 6.1. These relays are distributed as uniform PPP with density λ_R. For simplicity, we assume BSs and relays have equal transmit power P, and all relays DF strategy. In fact, a DF relay can correctly decode and send the signal to the IoT device if its received SNR is above a certain threshold. We assume BSs and relays are equipped with a large number of antennas that provide a narrow beam with a high directivity gain G, and a perfect beam alignment is considered [58]. Hence, the total gain G_t for the link between the BSs and relays are G^2.
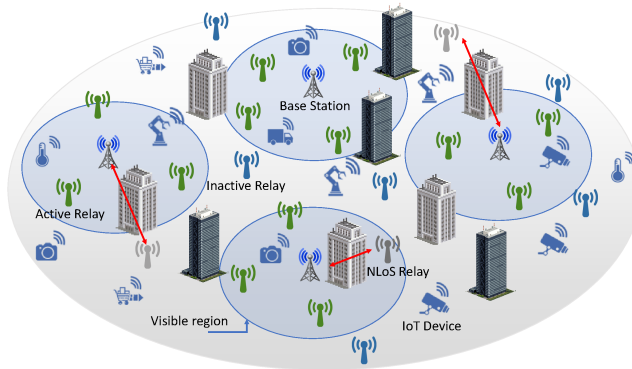
Figure 6.1: A realization of mmWave relaying systems for IoT devices.

Similar to the previous chapters, we consider the LoS link only in communication

between nodes. In DF strategy, relays decode a noisy version of the signal transmitted from the BS and retransmit it to the IoT device if the received SNR is greater than a threshold γ_{th}. We consider the uplink transmission of IoT applications because the uplink traffic load is much higher than the downlink traffic. Given the path-loss model in the chapter 3, the maximum distance between the BS and relay to receive a signal with SNR $\geq \gamma_{th}$ is given by

$$R_{th} = \left(\frac{PG^2}{A \ N_0 \gamma_{th}}\right)^{\frac{1}{\alpha}}. \tag{6.1}$$

Note that, the relay will be activated if the SNR at the relay $\gamma_{S,R} \geq \gamma_{th}$; otherwise, the relay will be inactive. As shown in Fig. 6.1, we refer to the area containing all active relays as a visible region.

6.3 Relay Selection Technique

Communications at mmWave bands are considered as highly unreliable due to unfavorable propagation characteristics where the transmitting beam can be obstructed very easily [69]. Relays will play a more important role in improving the robustness in communication between BSs and IoT devices. However, applying an inflexible relay selection technique will significantly degrade the network performance and increase the scheduling overhead. Hence, a promising solution to provide high-reliable communication is to have standby communication links to the kth NLRs. Thus, we adapt the proposed routing technique in previous chapter for dual-hop transmissions.

The adapted technique selects the NLR which has the nearest LoS distance with the IoT device to reduce the distance between the selected relay and IoT devices. Also, the adapted technique controls the relay-selected region to manage the distance between a selected relay with the IoT device and select the second NLR or more generally up to the kth NLR. For instance, limiting the relay-selected region is equivalent to decreasing the density of relays. As a result, the nearest relay will become farther away from the IoT device. We limit the relay-selected region deviation by an angle Ψ from the BS to IoT device link as shown in Fig. 6.2. It is noticed that we have two cases depending on the location of the IoT device. The first case, in Fig.6.2.a, represents the scenario when the IoT device does not exist in the visible region. The second case represents the case when IoT device exists in the visible region as shown in Fig.6.2.b.
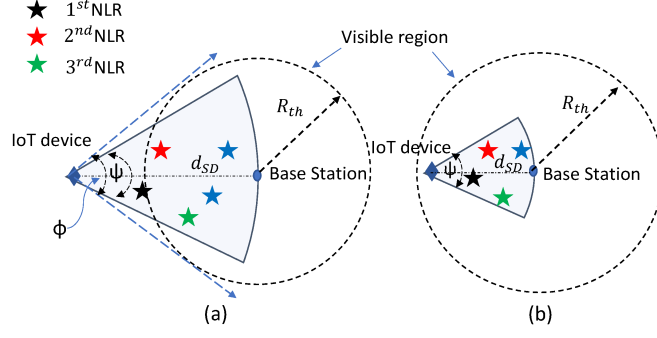
Figure 6.2: An example of the kth NLR technique in a certain area bounded by angle Ψ for (a) $R_{th} < d_{SD}$ and (b) $R_{th} \geq d_{SD}$.

6.4 Performance Analysis

In this section, we analyze the connectivity probability and energy consumption of the proposed relay selection technique in mmWave relaying systems. Firstly, we derive a closed-form expression for the distance distribution between the kth NLR and IoT device. Different from previous chapters, we consider both the relay-selected region and the order of the NLR. Then we use this closed-form expression to derive analytical expressions for connectivity probability and energy consumption for the IoT device associated with the kth NLR.

6.4.1 Distance Distribution

In the NLR technique, each IoT device is served by the kth NLR. These NLRs seen from the IoT device form independent non-homogeneous PPP with intensity functions $\Lambda_A(r)$. The intensity of relays in the shadowed region with an angle Ψ shown in Fig. 6.3 is given by

$$\Lambda_A(r, \Psi) = \int_0^r \int_{-\Psi/2}^{\Psi/2} e^{-\beta x} \lambda_R x \; dx \; d\theta = \frac{\Psi \lambda_R}{\beta^2} \left(1 - \beta r e^{-\beta r} - e^{-\beta r} \right). \tag{6.2}$$

According to *Poisson law*, the probability that the shadowed region in Fig. 6.3 contains exactly k relays is defined as

$$P(K = k, A) = \frac{(\Lambda_A(r))^k}{k!} e^{-\Lambda_A(r)}. \tag{6.3}$$

Then the PDF of the distance between the IoT device and the kth NLR for an angle Ψ is given by [53]

$$f_{NLR_k}(r, \Psi) = \frac{[\Lambda_A(r, \Psi)]^{(k-1)}}{(k-1)!} \; e^{-\Lambda_A(r, \Psi)} \frac{d\Lambda_A(r, \Psi)}{dr}. \tag{6.4}$$

For the NLR ($k = 1$), one can derive the distance distribution from the NLR to the IoT device for an angle Ψ as

$$f_{NLR}(r, \Psi) = \Psi \lambda_R r e^{\left(-\beta r - \frac{\Psi \lambda_R}{\beta^2}\left(1 - \beta r e^{-\beta r} - e^{-\beta r}\right)\right)}. \tag{6.5}$$
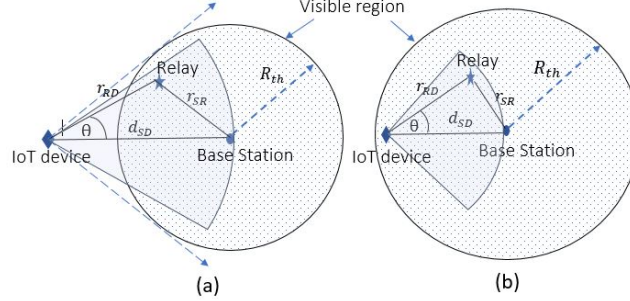
Figure 6.3: A graphical representation of mmWave network connectivity model for (a) $R_{th} < d_{SD}$ and (b) $R_{th} \geq d_{SD}$.

6.4.2 Connectivity Probability Analysis

The connectivity probability defined as the probability that the IoT device is connected to the network through LoS link(s). Therefore, the connectivity probability of dual-hop communication is the probability that there exists a LoS connection for the BS-relay link and relay-IoT device link. The connectivity probability for the kth NLR, defined as the probability that the BS and IoT device are connected through the kth NLR with LoS links. Without loss of generality, we develop the analysis of the connectivity probability considering a typical IoT device located at the origin with the associated BS. The concept of a typical IoT device in stochastic geometry refers to an IoT device residing at the origin where the properties of the point process can be computed. In other words, the typical IoT device is assumed to be a representative to all IoT devices. As shown in Fig. 6.3, we assume the IoT device located at $(0, 0)$, BS at $(d_{SD}, 0)$ and selected relay at (x_{R_k}, y_{R_k}). The connectivity probability of the path that includes the kth NLR is given by

$$P_{Con} = P_{S,R_k} \times P_{R_k,D}, \tag{6.6}$$

where $P_{R_k,D}$ denotes the probability that at least k relays have LoS connection to the typical IoT device, given by

$$P_{R_k,D} = 1 - \sum_{i=0}^{k-1} \frac{(\Lambda_A(r_{sd}, \Psi))^i}{i!} e^{-\Lambda_A(r_{sd}, \Psi)}. \tag{6.7}$$

Regarding the link between the kth NLR and BS, P_{S,R_k} represents the LoS probability between the kth NLR and BS. This probability depends on the distribution of the distance

r_{SR} from the BS to k^{th} NLR. Note that, the distance distributions for r_{SR} and r_{RD} are dependent, and the relation between them for a given d_{SD} can be obtained by

$$r_{SR} = \sqrt{r_{RD}^2 + d_{SD}^2 - 2\ d_{SD}\ r_{RD}\ cos(\theta)}. \tag{6.8}$$

For given coverage angle θ and distance between the IoT device and relay r_{RD}, the connectivity probability for the kth NLR $P_{S,R_k} = e^{-\beta\ r_{SR}}$. As shown in Fig. 6.3, the visible region (dotted circle area) represents all possible locations of the relay which have SNR $\geq \gamma_{th}$. Hence, we integrate the connectivity probability over the visible region using the distance distribution of r_{RD} for the kth NLR. It is noted that there are two cases based on R_{th}. The first case represents the scenario when $R_{th} < d_{SD}$ shown in Fig.6.3.a given by

$$P_{con}(\Psi) = \frac{P_{R_k,D}}{\Psi} \times \int\limits_{-\Psi/2}^{\Psi/2} \int\limits_{R_{min}}^{R_{max}} e^{-\beta\sqrt{r^2+d_{SD}^2-2d_{SD}\ r\ cos(\theta)}} \times f_{NLR_k}(r, \Psi)\ dr\ d\theta, \tag{6.9}$$

where the parameters R_{min} , R_{max} and ϕ are given by

$$R_{min} = \frac{2\ d_{SD} - \sqrt{4\ d_{SD}^2 - 4\ \sec^2(\theta)(d_{SD}^2 - R_{th}^2)}}{2\sec(\theta)}. \tag{6.10}$$

$$R_{max} = \frac{2\ d_{SD} + \sqrt{4\ d_{SD}^2 - 4\ \sec^2(\theta)(d_{SD}^2 - R_{th}^2)}}{2\sec(\theta)}. \tag{6.11}$$

$$\phi = \arcsin\left(\frac{R_{th}}{d_{SD}}\right). \tag{6.12}$$

The connectivity probability in the second case as shown in Fig.6.3.b given the deviation angle Ψ is expressed as

$$P_{con}(\Psi) = \begin{cases} \frac{P_{R_k,D}}{2\pi}\left[\int\limits_{-\pi/2}^{\pi/2} \int\limits_{0}^{R_{max}} e^{-\beta r_{SR}} f_{NLR_k}(r, \Psi) dr d\theta + 2 \int\limits_{\pi/2}^{\Psi/2} \int\limits_{0}^{R_{min}} e^{-\beta r_{SR}} f_{NLR_k}(r, \Psi) dr d\theta \right] & \Psi > \frac{\pi}{2} \\ \frac{P_{R_k,D}}{2\pi} \int\limits_{-\Psi/2}^{\Psi/2} \int\limits_{0}^{R_{max}} e^{-\beta r_{SR}} f_{NLR_k}(r, \Psi) dr d\theta & \Psi \leq \frac{\pi}{2} \end{cases}. \tag{6.13}$$

6.4.3 Energy Consumption Analysis

We adopt the energy consumption model for the IoT device in [95], where the energy consumption at the IoT device consists of data processing and transmission energy consumption. The energy consumption at IoT device for transmitting and receiving N_{bits} is given by, respectively [93]

$$\eta_{tx} = (\epsilon_p + \epsilon_{tx})N_{bits}, \tag{6.14}$$

$$\eta_{rx} = \epsilon_p \ N_{bits}, \tag{6.15}$$

where ϵ_p and ϵ_{tx} is the energy dissipation per bit for data processing and transmission at IoT device, respectively. The energy dissipation per bit for data transmission is modeled as

$$\epsilon_{tx} = \rho \ r_{RD}^2, \tag{6.16}$$

where ρ is a constant of power amplification in the link budget. The average energy consumption at IoT device associated with k^{th} NLR for transmitting and receiving N_{bits} can be expressed by

$$\eta_{av} = (2\epsilon_p + \rho \ E(r_{RD}^2)) \ N_{bits}, \tag{6.17}$$

where $E(r_{RD}^2)$ is the expected value of squared distance between IoT device and k^{th} NLR, given by

$$E(r_{RD}^2) = \int\limits_{-\Psi/2}^{\Psi/2} \int\limits_{0}^{\infty} r_{RD}^2 \ f_{NLR_k}(r, \Psi) \ dr \ d\theta. \tag{6.18}$$

6.5   Simulation Results

In this section, we assess the accuracy of the analytical results by simulating the NLR selection technique in mmWave relaying systems. All simulation results are averaged over 500×10^3 realizations, and the simulations consider a square area fixed to [1000 $m \times$ 1000 m]. We assume that buildings have length and width range of [10 m, 25 m], and [10 m, 20 m], respectively. Similar to [36], the path-loss exponent $\alpha = 2$ and path-loss intercept $A = 69.8$ dB for LoS links. The network is assumed to be operated at 73 GHz with a system bandwidth $BW = 2$ GHz. The transmit power of relays and BSs $P = 30 \ dBm$, the thermal noise is given by $-174 + 10 \ log_{10}(BW)$ dBm, noise figure $= 10$ dB, and antenna gain for relays and source $G = 10$ dB. The energy dissipation per bit of processing is set to $\epsilon_p =$ 50 nJ/bit for IoT device, the power amplification constant is set to $\rho =$ 1 pJ/m2/bit, and IoT device generates 1000 bits [93].

In Fig. 6.4, we verify the accuracy of the analytical expressions for the connectivity probability and derived distribution for the distance from the IoT devices to the kth NLR given in (6.4). The system parameters are $\lambda_R = 4 \times 10^{-4} m^{-2}$, $\lambda_B = 2 \times 10^{-4} m^{-2}$, and $d_{SD} = 100 \ m$. In each realization, the relays and blockages are randomly and uniformly distributed over the square area. The theoretical results are consistent with the simulated

ones. Analyzing the results presented in Fig. 6.4.a for deviation angle $\Psi = 120°$, we observe that the mean and variance of distance distribution between NLR and IoT device increase as the order of the NLR becomes higher. The effect of relay-selected region for NLR on the distance distribution is illustrated in Fig. 6.4.b for $\Psi = \{90°, 120°, 180°\}$. As one may notice that increasing angle Ψ from 120° to 180° leads to an increase in the mean and variance for distance distribution between IoT device and NLR. This is due to the fact that limiting the region of selected-relay is equivalent to decreasing the density of relays. As a result, the nearest relay will become farther away from the IoT device.

(a) Varying k

(b) Varying Ψ
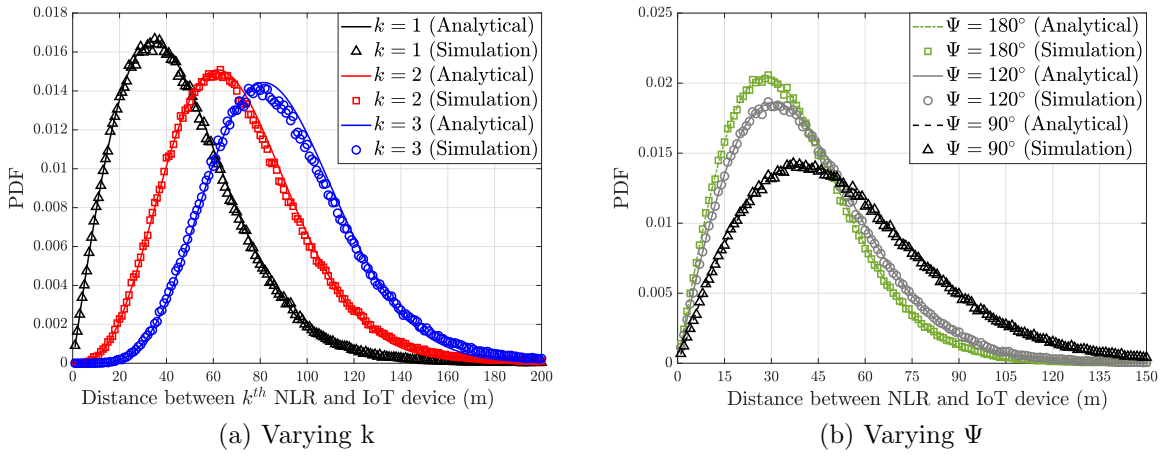
Figure 6.4: The distance distribution as a function of order of NLR (k) and the deviation angle (Ψ).

Fig. 6.5 illustrates the connectivity probability of the first three NLRs versus the distance between the IoT device and BS (d_{SD}) for $\Psi = \{90°, 120°\}$ and SNR threshold $\gamma_{th} = 20$ dB. The figure shows that the impact of the relay-selected region on the connectivity probability based on the distance between the IoT device and BS. As one may observe, the effect of Ψ on the connectivity probability depends on the location of the IoT device. For the first NLR ($k = 1$), the case $d_{SD} \geq 100\ m = R_{th}$ represents case (a) in Fig. 6.2 where the connectivity probability decreases as Ψ increases. This is because the increase in Ψ results in more (nearest) relays near to the IoT device and reduces the probability of the NLR to be located in the visible region. On the contrary, increasing Ψ improves the connectivity probability for $d_{SD} < 100\ m$ which represents case (b) in Fig. 6.2. Also, the impact of the order of NLR on the connectivity probability depends on the location of the IoT device. For $\Psi = 120°$, the connectivity probability for the first NLR outperforms the second and the third NLR for $d_{SD} < 100\ m$. This represents case

(a) in Fig. 6.2 where the IoT device exists on the visible region, and the NLR has the minimum average distance to the IoT device. For $d_{SD} \geq 100$, this region represents case (b) in Fig. 6.2, and the higher-order NLR surpasses the lower-order of the NLR in the connectivity probability. The reason is that the connectivity probability depends on the distance between the BS and selected relay, and increasing the order of NLR decreases the distance between the BS and IoT device.
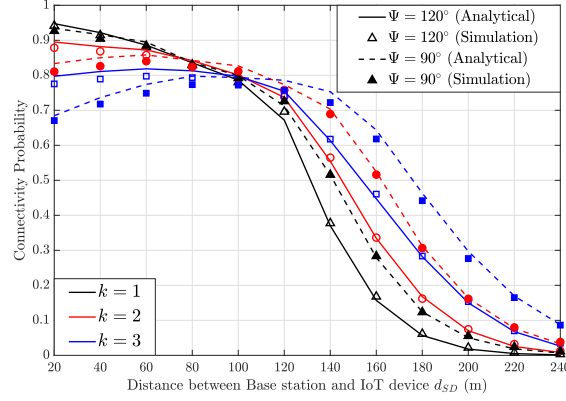
Figure 6.5: The connectivity probability as a function of order of NLR (k) and the deviation angle (Ψ).

Fig. 6.6.a presents the connectivity probability of IoT device for the first two NLRs versus different deviation angle Ψ where $\lambda_R = \{2, 5\} \times 10^{-4} \, m^{-2}$, $\lambda_B = 5 \times 10^{-5} \, m^{-2}$, $\gamma_{th} = 20$ dB, and $d_{S,D} = 250 \, m$. It is shown that increasing the density of relays λ_R decreases the connectivity probability when the IoT device does not exist in the visible region which represents case (a) in Fig. 6.2. Also, the connectivity probability deteriorates as Ψ extends. An interesting observation from the results is that the connectivity probability of the second NLR outperforms the one for the first NLR. This is due to the second NLR being close to IoT device compared to the first one.

In Fig. 6.6.b, the energy consumption is depicted as a function of k, and λ_R. The results indicate that the energy consumption significantly decreases as the deviation angle Ψ extends. As shown in the figure, increasing Ψ from $60°$ to $180°$ reduces the consumption energy by 50% for $\lambda_R = 2 \times 10^{-4}$ and $k = 2$. This is because the average distance between the NLR and IoT device increases as Ψ extends as shown in Fig. 6.4.b. Also, as the relay density increases, energy consumption reduces significantly. From Fig. 6.6, we note the trade-off between the connectivity probability and the energy consumption when limiting the relay-selected region and changing the relay density are applied to the NLR selection

technique. For instance, decreasing Ψ significantly improves the connectivity probability, however, the average energy consumption increases.

(a) The connectivity probability

(b) The energy consumption
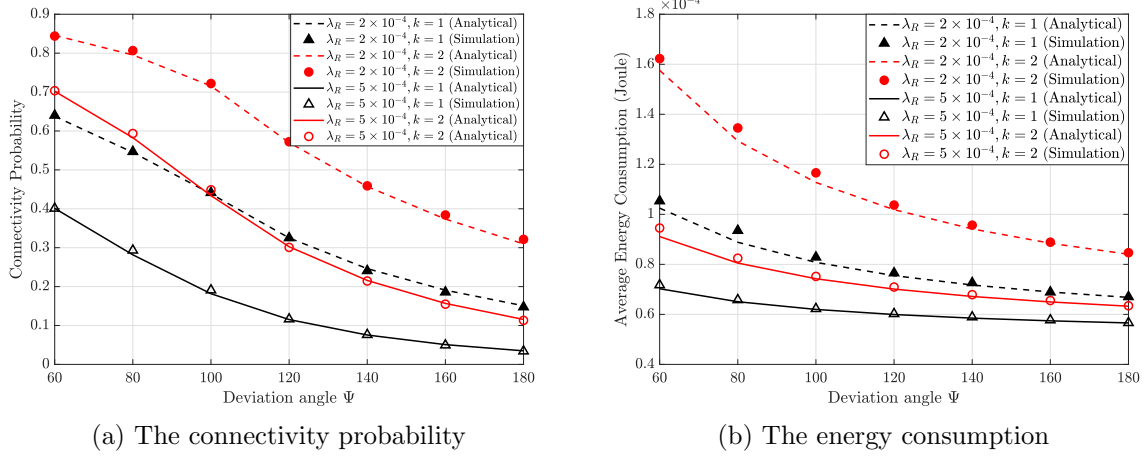
Figure 6.6: The connectivity probability and the energy consumption at IoT device as a function of order of NLR (k), the deviation angle (Ψ), and density of relays λ_R.

Fig. 6.7 depicts the impact of the density of blockages on the connectivity probability for different deviation angles Ψ with $\lambda_R = 2 \times 10^{-4} m^{-2}$, $d_{SD} = 250\ m$, $k = 1$, and $\gamma_{th} = \{10, 15\}$ dB. The results indicate that, with a fixed Ψ, the connectivity probability significantly deteriorates as the density of blockages increases for different SNR thresholds. The figure also shows that the impact of relay-selected region on the connectivity probability depends on γ_{th}. It is noticeable that the connectivity probability significantly reduces as Ψ extends for $\gamma_{th} = 15$ dB. This decline in connectivity probability rises as γ_{th} increases. We notice that decreasing γ_{th} and Ψ can achieve a significant improvement in the connectivity probability.
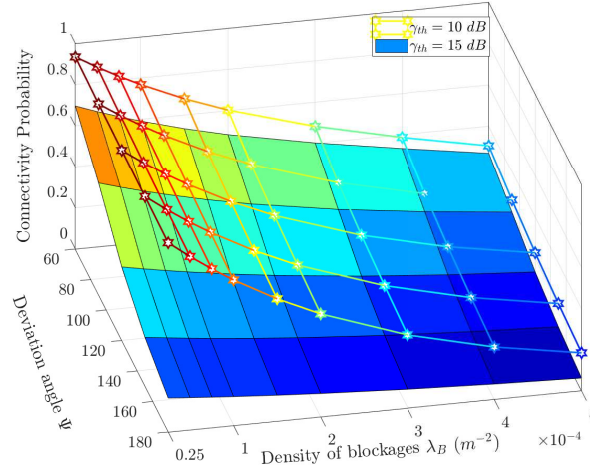
Figure 6.7: Connectivity probability of NLR versus different deviation angle Ψ and density of blockages λ_b for $\lambda_R = 2 \times 10^{-4}m^{-2}$, $d_{SD} = 250\ m$, and $\gamma_{th} = \{10, 15\}$ dB

6.6 Summary

In this chapter, we proposed a NLR selection technique for IoT devices in mmWave relaying systems. We presented a tractable analytical framework to characterize the network connectivity for the proposed technique using tools from stochastic geometry. Moreover, we investigated the impact of the relay-selected region and the distance between the base station and IoT device on the network connectivity of mmWave relaying systems. The analytical results unveil a high degree of accuracy which is confirmed by extensive simulations at different relay densities, blockage densities, and SNR thresholds. Results obtained via simulations and analyses reveal the trade-off between the network connectivity and the energy consumption of IoT devices. Results also reveal a significant impact of blockage density and controlling the relay-selected region on the network connectivity and energy consumption.

Chapter 7

Uplink Performance of MmWave Fronthaul Cell-free Massive MIMO Systems

7.1 Introduction

Fifth-generation (5G) and beyond networks are currently witnessing a wide range of new users services and an unprecedented increase in data rates [56,96,97]. A promising technology to support the requirements of these networks is the CF mMIMO [12,98]. In CF mMIMO systems, a large number of distributed APs are deployed and connected to a CPU via a fronthaul network to communicate with a smaller number of users. In that, the CPU operates all APs in a cooperative manner to serve all users simultaneously over the same time-frequency resources. It has been revealed that the performance of CF mMIMO systems outperforms the counterpart performance of fully distributed small-cell systems in-terms of the 95%-likely per-user throughput. Besides, the system can provide a uniformly reliable service to all users within the coverage area through applying max-min power control [98–100].

It is noteworthy that the capacity of the fronthaul network dramatically influences the CF mMIMO system performance. This is due to its vital role in handling the data exchange between the CPU and APs. More specifically, the higher amount of data to be transferred in the fronthaul network, the higher capacity requirement for fronthaul links. The performance of the limited-fronthaul CF mMIMO systems has been extensively analyzed in [101–107] and references therein. The works in [101–103] investigated the limited-fronthaul capacity effect on the downlink (DL) performance, whereas the authors in [101,104,106,107] analyzed the limited-fronthaul capacity effect on the UL performance. Results showed that the limited capacity of fronthaul links degrades the achievable UL

and DL data rates.

The limited-fronthaul capacity effect on the DL performance has been investigated under two different system operations, namely, fully-distributed and fully-centralized systems. In the fully-distributed system operation, the channel estimation and DL precoding processes are performed at APs while the CPU is the responsible entity for the channel estimation and DL precoding processes in the fully-centralized system operation. The DL performance of CF mMIMO systems has been analyzed under both system operations in [101, 102]. The work in [101] compared both system operations when normalized conjugate beamforming (CB) is applied for DL transmission. On the other hand, the work in [102] considered different precoding techniques for both system operations. In particular, local CB precoding along with beamforming training are applied for the distributed system operation due to the low-processing capabilities at APs. However, zero-forcing (ZF) precoding is applied for the centralized system operation due to the high processing capabilities of the CPU. Besides, the authors in [103] analyzed the DL performance of CF mMIMO under limited-fronthaul capacity assuming fully-distributed operation with local CB precoding. Results in [101–103] revealed that the limited-fronthaul effect is more prominent on the centralized system operation with ZF precoding. Also, the achievable DL data rates of the distributed operation using local CB precoding and beamforming training approaches the counterpart performance of the centralized operation with ZF precoding as the capacity of the fronthaul links decreases. In addition, the number of served users per AP should be adapted with the available fronthaul capacity to alleviate the limited capacity effect.

The impact of limited capacity fronthaul links on the UL performance of CF mMIMO systems has been investigated in-terms of the spectral efficiency in [104, 106] and the energy efficiency in [104, 107]. The UL transmission schemes between AP and CPU in these works can be categorized into three different approaches, namely, Estimate-Detect-Compress-Forward (EDCF), Estimate-Compress-Forward (ECF), and Compress-Forward-Estimate (CFE). In ECF, all APs firstly estimate the users' channels. Then, the estimated channels as well as the received data signals are compressed and transmitted to the CPU where the detection process is carried out. On the other hand, in EDCF, both channel estimation and UL data detection processes are performed locally at the APs. The APs, then, compress the local detected signals and send them to the CPU. Contrary to EDCF, in

CFE, the received data and pilot signals at APs are compressed and transmitted to the CPU where both channel estimation and users' data detection processes are carried out.

The authors in [104] investigated the UL performance of limited-fronthaul CF mMIMO under the aforementioned UL transmission schemes when applying maximum ratio combining (MRC) detection technique. In doing so, the authors proposed a low-complexity fronthaul rate allocation among users, followed by one-dimensional line search for capacity allocation between pilot and data transmission. Results revealed that there is an optimal portion of the fronthaul capacity to be assigned for the data transmission to maximize the sum UL data rates under ECF and CFE. In [106], the UL max-min problem of limited-fronthaul CF mMIMO has been analyzed under the EDCF approach assuming a two-stage UL data detection technique. Results showed that there is an optimal number of users to be served by each AP to lessen the impact of limited-fronthaul capacity. Furthermore, the work in [107] addressed the UL energy efficiency of limited-fronthaul CF mMIMO for the EDCF approach when applying a two-stage UL data detection technique. It has been shown that there is a trade-off between the number of APs and the number of antennas per AP to maximize the UL energy efficiency.

In fact, the fronthaul network can be deployed in different manners, namely, wired and wireless. Deploying a wired fronthaul network can provide high capacity fronthaul links, especially using high-speed optical fiber cables. However, this will significantly increase the deployment cost due to the large number of links to be established between APs and CPU [108]. As such, a wireless fronthaul link is more preferable for the system operation. For instance, microwave communication can provide the fronthaul network with low deployment cost, easy upgrade, and high-flexibility [109]. Nevertheless, the limited available bandwidth in microwave bands leads to a degradation in the system performance. Many potential technologies have been designed to overcome such limitation in bandwidth, including non-orthogonal multiple access [110, 111], cognitive radio [112], free space optics (FSO) [113] and mmWave [9, 34, 45]. For instance, FSO communication can provide high bandwidth comparable to those in microwave bands with more cost-efficient in implementation and maintenance. In that, aiming at deploying a cost-efficient fronthaul network, the authors in [113] proposed a FSO-based fronthaul network for CF mMIMO operation. However, FSO transmission suffers from the non-ideal conditions arising from atmospheric turbulence and unstable weather conditions, such as rain, fog, haze and dust [114]. On

the other hand, mmWave communication can preserve link connectivity in a more reliable manner than FSO [115]. Also, motivated by the high available bandwidth as well as the high beamforming gain of mmWave bands, a mmWave fronthaul network may play an important role in handling the information exchange between the CPU and APs [27, 116].

Despite recent works have investigated the access link performance of CF mMIMO systems in the mmWave band [117, 118], the reported results in these works may be unreliable. This is due to the short wavelength of mmWave communications which poses a crucial threat to the link stability, especially under non LoS communications [42, 119]. As such and since the environment around users includes static and dynamic objects that may completely block the LoS links between users and APs [119, 120], mmWave is not a reliable candidate for the access link operation. On the other hand, since both CPUs and APs are deployed at fixed locations, this boosts the possibility of having reliable fronthaul links for CF mMIMO systems. Therefore, in this chapter, we analyze the performance of CF mMIMO systems when adopting mmWave bands for the fronthaul communication while carrying out the access link operation over the microwave band. In that, tools from stochastic geometry are exploited to derive an analytical expression for the UL achievable data rates under the considered system operation.

This chapter investigates the UL performance of CF mMIMO under mmWave-assisted fronthaul network. Unlike a deterministic approach in which the analysis is performed under specific system parameters, stochastic geometry offers a statistical approach to develop a tractable and accurate modeling framework to characterize the performance of CF mMIMO systems. The analysis is conducted assuming the system operation under the CFE transmission approach due to its potential in improving the achievable UL data rates since the estimated channels will be available while performing the data detection process at the CPU. Also, we consider that the network consists of multiple CPUs to which APs are associated in a distance-based association criterion. In what follows we summarize the contributions of this investigation as compared to previous work in the literature:

- Analyzing the performance of CF mMIMO systems under the deployment of a practical and cost-efficient mmWave-based fronthaul network, taking into account the inevitable effect of blockages on the fronthaul communication in the mmWave band.

- Exploiting stochastic geometry tools to derive the distribution of the achievable capacity of mmWave fronthaul links, taking into account the density of blockages and CPUs as well as the available bandwidth for fronthaul communications.

- Deriving an analytical expression for the average UL data rates of CF mMIMO systems while considering the effects of both the blockages and the distribution of the provided capacity for the fronthaul links.

- Providing a comprehensive investigation of different system parameters on the average achievable UL data rates, namely, the density of CPUs and APs under different environments (dense urban, suburban and rural).

7.2   System Model

7.2.1   Network Architecture

We consider a CF mMIMO system in which APs and users are distributed according to a homogeneous PPP with densities λ_a and λ_u, respectively. All APs are equipped with N_{ap} antennas, whereas user equipments (UEs) are assumed to be single-antenna terminals. In addition, we assume that the signal processing tasks are distributed among different physical CPUs that are connected together and distributed according to a homogeneous PPP with density λ_c [121]. In that, we consider that APs are divided into disjunct sets where the APs in each set are connected to the nearest CPU via fronthaul links. We also consider the presence of static blockages such as buildings as shown in Fig. 7.1. In particular, we model the centers of blockages as a PPP with density λ_b, and each blockage is modelled as a rectangle shape with random sizes and orientations. In that, the length and width parameters of blockages are independent and uniformly distributed with $[L_{min}, L_{max}]$ and $[W_{min}, W_{max}]$, respectively.

7.2.2   Fronthaul Communication

MmWave frequency band is adopted for the fronthaul network operation due to the large available bandwidth and the high beamforming gains. For instance, one can operate the fronthaul network at 73 GHz where the available contiguous bandwidth is up to 5 GHz [23]. Such high bandwidth can handle the immense amount of data transfer in the fronthaul network of CF mMIMO systems. Nevertheless, a prerequisite for a reliable

operation of the mmWave fronthaul network in such band is to have LoS links between the CPUs and their associated APs. This is due to the fact that signal transmission in such band suffers from severe path-loss, especially under NLoS transmissions, which in turn may lead to transmission breakdown [36]. As such, we consider the LoS link only in communication between CPU and APs. For the path-loss model, we assume the reference distance is 1 m, and the transmitted power P_f with propagation distance r is attenuated by factor r^α where α is the path-loss exponent [61]. The corresponding SNR received at the AP is given by

$$\gamma = \frac{P_f G_t}{A r^\alpha N_0 \mathscr{B}_f},$$ (7.1)

where N_0 is the thermal noise power per Hz, A is the path-loss intercept, and $\mathscr{B}_f$ represents the link bandwidth. Also, G_t denotes the total gain for the link between the AP and CPU. Note that, since CPUs and APs are deployed in fixed locations, the buildings are considered as the main obstacle towards having LoS links between the CPUs and their associated APs. In particular, the probability of having a LoS mmWave fronthaul link for a certain AP depends mainly on its distance with the associated CPU as well as the density of blockages.

7.2.3 Access Communication

Different from the fronthaul transmission, the environment around users includes static and dynamic objects that may completely block the LoS links between users and APs [119, 120]. As such, and aiming at having reliable access communication links, we consider that access links operate on the microwave band. Also, the channels between APs and users are modeled as Rayleigh fading channels. For a specific network realisation with M APs and K users, the channel vector $\boldsymbol{g}_{mk} \in \mathbb{C}^{N_{ap} \times 1}$ between the m-th AP and the k-th
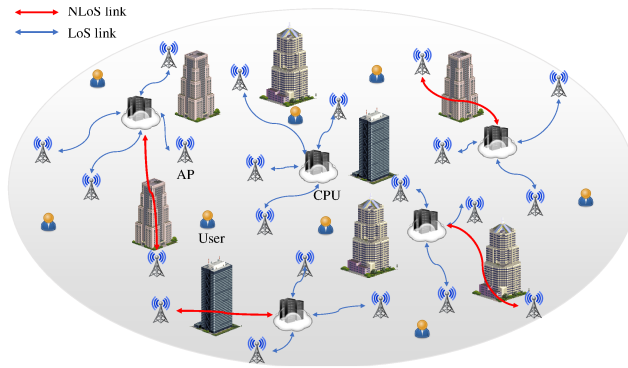
Figure 7.1: CF mMIMO system with mmWave fronthaul.

user is given by

$$\boldsymbol{g}_{mk} = \sqrt{l_{mk}}\boldsymbol{h}_{mk}, \tag{7.2}$$

where $\boldsymbol{h}_{mk} \in \mathbb{C}^{N_{ap} \times 1}$ denotes a vector of the small-scale fading coefficients whose entries are independent and identically distributed (i.i.d.) $\mathcal{CN}(0,1)$. Also, l_{mk} denotes the large-scale fading coefficient which accounts for the geometric attenuation (path-loss). Furthermore, we consider the three-slope path-loss model for the large-scale fading calculations as follows [122]:

$$l_{mk} = d_{mk}^{-3.5}\,\mathbf{1}(d_{mk} > d_1) + d_1^{-1.5}d_{mk}^{-2}\,\mathbf{1}(d_0 \leq d_{mk} \leq d_1) + d_1^{-1.5}d_0^{-2}\,\mathbf{1}(d_{mk} < d_0), \tag{7.3}$$

where $\mathbf{1}(\cdot)$ denotes the indicator function and d_{mk} represents the distance between the m-th AP and the k-th user. Also, d_0 and d_1 are two constants whose values are set to 10 m and 50 m, respectively.

7.3 Fronthaul Operation

In this section, we analyze the UL performance of CF mMIMO in the presence of mmWave fronthaul network. Firstly, using tools from stochastic geometry, we derive the density of activated APs for fronthaul communications (APs with LoS fronthaul links with their associated CPUs). Then, we derive the distribution of the achievable fronthaul capacity between APs and CPU as a function of the densities of blockages and CPUs.

7.3.1 Active APs Density

Due to the impact of blockages on the mmWave fronthaul links between APs and CPUs, some APs may not be capable of exchanging data with their associated CPUs. As such, we firstly analyze the impact of blockages on the density of activated APs. Note that, the activation of a particular AP depends mainly on the blockage density and its distance with its associated CPU. Hence, the activated APs can be released as being generated from an independent thinning operation over the entire existing APs PPP [53]. In that, the corresponding density of activated APs can be calculated as

$$\widetilde{\lambda}_a = p_a \times \lambda_a, \tag{7.4}$$

where p_a is the probability of AP activation. We assume that APs are associated with the nearest CPU where the distance distribution between the AP and the nearest CPU

is given by

$$f_R(r) = 2\pi\lambda_c \, re^{-\pi\lambda_c r^2}. \tag{7.5}$$

Then, the distance distribution is applied to evaluate the activation probability p_a as follows:

$$p_a = P(N_B(CPU, AP) = 0) = \int_0^\infty e^{-\beta r} 2\pi\lambda_c \, re^{-\pi\lambda_c r^2} \, dr = 1 - \beta \int_0^\infty e^{-\beta r} e^{-\pi\lambda_c r^2} \, dr$$

$$= 1 - \frac{\beta e^{\frac{\beta^2}{4\pi\lambda_c}}}{2\sqrt{\lambda_c}} erfc\Big[\frac{\beta}{2\sqrt{\pi\lambda_c}}\Big], \tag{7.6}$$

where $N_B(AP, CPU)$ represents the number of blockages on the link between the CPU and AP, and erfc is the complementary error function.

7.3.2 Achievable Fronthaul Capacity

After determining the set of activated APs for fronthaul communication, one needs to determine the provided fronthaul capacity to APs which in turn affects the amount of data to be transferred over the fronthaul network. To this end, we firstly derive the distribution of the provided capacity to APs as a function of the available mmWave bandwidth as well as the densities of CPUs, APs, and blockages. In doing so, we assume the available fronthaul bandwidth is divided equally among these APs and reused with a factor one between CPUs. As such, the assigned bandwidth to each active AP is given by

$$\mathscr{B}_{f,m} = \frac{\mathscr{B}_f}{M_u}, \tag{7.7}$$

where M_u denotes the number of APs, associated to CPU u. Based on that, and considering the noise-limited system for mmWave communications [123], the fronthaul capacity in bps for link between m-th AP and its associated CPU u is defined as

$$\mathscr{R}_m = \mathscr{B}_{f,m} \times log_2(1 + \gamma) = \frac{\mathscr{B}_f}{M_u} \times log_2(1 + \frac{P_f G_t}{Ar^\alpha N_0 \frac{\mathscr{B}_f}{M_u}}). \tag{7.8}$$

To consider the impact of the mmWave fronthaul links' capacities on the system performance, one has to normalize the provided capacity of fronthaul links to access link bandwidth. Since all users are served over the whole available access bandwidth, the normalized mmWave fronthaul capacity of the m-th AP C_m in bps/Hz is given by

$$C_m = \frac{\mathscr{R}_m}{\mathscr{B}_A} = \frac{\mathscr{B}_f}{M_u * \mathscr{B}_A} \times log_2(1 + \frac{P_f G_t}{Ar^\alpha N_0 \frac{\mathscr{B}_f}{M_u}}) = \frac{\mathscr{B}_f}{M_u * \mathscr{B}_A} \times log_2(1 + \frac{\rho \, M_u}{r^\alpha \mathscr{B}_f}), \tag{7.9}$$

where $\rho = \frac{P_f G_t}{A N_0}$. Since, we consider that each AP is served by its closest CPU, this results in a non-overlapping and irregular coverage area that form a Voronoi tessellation of the

space [124]. Hence, the probability mass function (PMF) of the number of active APs per CPU will be [125]

$$f_{M_u}(m_u) = \frac{(\frac{3.5}{\lambda_h+3.5})^{3.5}}{\Gamma(3.5)} \left(\frac{\lambda_h}{\lambda_h + 3.5}\right)^{m_u} \frac{\Gamma(m_u) + 3.5}{\Gamma(m_u) + 1}, \tag{7.10}$$

where $\lambda_h = \widetilde{\lambda}_a/\lambda_c$ represents the average number of active APs, associated to CPU.

Depending on the PMF of the number of active APs per CPU, the cumulative distribution function of the achievable fronthaul capacity for the m-th AP C_m can be derived as follows:

$$\begin{aligned} F_{C_m}(c_m) &= \sum_{m_u=0}^{\infty} F_{(C_m|M_u=m_u)}(c_m) \times P(M_u = m_u) \\ &= \sum_{m_u=0}^{\infty} P(C_m \leq c_m | M_u = m_u) \times f_{M_u}(m_u) \\ &= \sum_{m_u=0}^{\infty} P\left(\frac{\mathcal{B}_f}{m_u * \mathcal{B}_A} log_2(1 + \frac{\rho \; m_u}{r^\alpha \mathcal{B}_f}) \leq c_m\right) \times f_{M_u}(m_u) \\ &= \sum_{m_u=0}^{\infty} P\left(r \geq \sqrt{\frac{\rho \; m_u/\mathcal{B}_f}{2^{(\frac{m_u}{\mathcal{B}_f/\mathcal{B}_A}c_m)} - 1}}\right) \times f_{M_u}(m_u). \end{aligned} \tag{7.11}$$

Then, PDF of the achievable capacity C_m between the APs and the CPU is given by

$$\begin{aligned} f_{C_m}(c_m) = \frac{dF_{C_m}(c_m)}{d \; c_m} &= \sum_{m_u=0}^{\infty} \frac{log(2)\mathcal{B}_A}{2} \sqrt{\rho \frac{m_u^3}{\mathcal{B}_f^3}} \frac{2^{(\frac{m_u}{\mathcal{B}_f \mathcal{B}_A}c_m)}}{\sqrt{(2^{(\frac{m_u}{\mathcal{B}_f/\mathcal{B}_A}c_m)} - 1)^3}} \\ &\times f_R\left(\sqrt{\frac{\rho \; m_u}{\mathcal{B}_f(2^{(\frac{m_u}{\mathcal{B}_f/\mathcal{B}_A}c_m)} - 1)}}\right) f_{M_u}(m_u), \end{aligned} \tag{7.12}$$

where $f_R(.)$ is the PDF of the distance between CPU and APs. This distance distribution depends mainly on the availability of link between APs and CPU where the AP should have a LoS connection with its associated CPU to be active. Since the location of APs are uniformly distributed, the PDF of the distance from the CPU to APs can be obtained as follows

$$f_R(r) = P(R = r | N_B(CPU, AP) = 0) = \frac{\frac{2r}{R_o^2}e^{-\beta r}}{\int_0^{R_o} \frac{2x}{R_o^2}e^{-\beta x}d \; x} = \frac{\beta^2 r e^{-\beta r}}{1 - e^{-\beta \; R_o}(1 + \beta \; R_o)}, \tag{7.13}$$

where $R_o = \sqrt{\lambda_c^{-1}}$ is the average coverage radius of the CPU.

By substituting (7.10) and (7.13) in (7.12) and after some mathematical manipulations, the PDF of the achievable capacity between APs and CPU can be given by

$$\begin{aligned} f_{C_m}(c_m) = \mathcal{Q}_{\mathcal{B}} \sum_{m_u=0}^{\infty} m_u^2 \frac{2^{(\frac{m_u}{\mathcal{B}_f \mathcal{B}_A}c_m)}}{(2^{(\frac{m_u}{\mathcal{B}_f/\mathcal{B}_A}c_m)} - 1)^2} &\times exp\left[-\beta\left(\frac{\rho \; m_u}{\mathcal{B}_f(2^{(\frac{m_u}{\mathcal{B}_f/\mathcal{B}_A}c_m)} - 1)}\right)^{0.5}\right] \\ &\times \left(\frac{\lambda_h}{\lambda_h + 3.5}\right)^{m_u} \frac{\Gamma(m_u) + 3.5}{\Gamma(m_u) + 1}. \end{aligned} \tag{7.14}$$

with

$$\mathscr{Q}_{\mathscr{B}} = \frac{\frac{log(2)}{2\ \Gamma(3.5)}(\mathscr{B}_A/\mathscr{B}_f^2)\beta^2\rho}{(1 - e^{-\beta\ R_o}(1 + \beta\ R_o))}(\frac{3.5}{\lambda_h + 3.5})^{3.5}. \tag{7.15}$$

This PDF of the achievable capacity is defined in the interval $[c_{min}, \infty]$ where c_{min} is given by

$$c_{min} = \frac{\mathscr{B}_f}{M_u * \mathscr{B}_A} \times log_2(1 + \frac{\rho\ M_u}{R_o^\alpha \mathscr{B}_f}). \tag{7.16}$$

7.4 Uplink Performance Analysis

Capitalizing on the derived expressions for the density of activated APs and the distribution of the provided fronthaul capacity, we provide a mathematical framework to calculate the average achievable UL data rates of CF mMIMO systems in this section.

7.4.1 Data Compression

Due to the limited capacity of fronthaul links, one cannot perfectly represent the transmitted signals from APs to CPUs. This urges the need of signal compression before signal transmission through the fronthaul links. This in turn leads to a distortion that can be precisely analyzed in the rate-distortion theory [126]. Such distortion can be modeled as a quantization noise as in [103, 104]. In particular, to compress a signal $X \sim f_X(x)$ with zero mean and variance $\mathscr{P}$ to a compressed version $\hat{X}$, subject to a distortion measure $d(X, \hat{X})$ with $\mathbb{E}\{d(X, \hat{X})\} \leq Q$, the rate distortion function can be defined by

$$R(Q) = \min_{f(\hat{x}|x):\mathbb{E}\{|\hat{X}-X|^2\}\leq Q} I(\hat{X}; X), \tag{7.17}$$

where $I(.;.)$ is the information content, and $\hat{X}$ can be defined as $\hat{X} = X + q$, with $q \sim \mathscr{CN}(0, Q)$ be the additive quantization noise which is independent of X [103, 104]. Thus, the amount of information to be transmitted between the m-th AP and its associated CPU can be expressed as a function of the differential entropy by

$$C_m = I(\hat{X}; X) = h(\hat{X}) - h(\hat{X}|X) \leq \log_2(1 + \mathscr{P}/Q_m). \tag{7.18}$$

As such, the compression quantization noise accompanying the data transmission over this link can be expressed by [104]

$$Q_m = \frac{\mathscr{P}}{2^{C_m} - 1}. \tag{7.19}$$

7.4.2 Uplink Channel Estimation

We adopt time-division duplexing (TDD) mode for the system operation. Depending on the channel reciprocity property under TDD operation, the APs exploit the UL estimated channels to perform the DL data precoding. Also, no DL pilots are transmitted, however, users detect the DL transmitted data symbols depending on the channel statistics. In that, users send pilot sequences in the first phase for the sake of channel estimation where the channel estimation process is performed between users and activated APs for fronthaul communication. After activated APs receive the transmitted pilot sequences from users, they compress them and send the compressed vectors through the fronthaul links to the CPU. We assume that the received training vector at each antenna element is compressed separately. Therefore, the compressed vector at the r-th antenna element in the m-th AP will be

$$\hat{\boldsymbol{y}}_{p,m,r} = \boldsymbol{y}_{p,m,r} + \boldsymbol{q}_{p,m,r}, \tag{7.20}$$

where $\boldsymbol{q}_{p,m,r}$ denotes the quantization noise vector whose entries are i.i.d. $\mathscr{C}\mathscr{N}(0, Q_{p,m,r})$. We assume that the training vectors at different antenna elements are assigned equal fronthaul capacities. Also, the different pilot symbols within the same training vector are assigned equal fronthaul capacities. Let us consider $C_{p,m}$ as the assigned capacity for pilot symbols transmission from the r-th antenna element in the m-th AP to its associated CPU such that

$$C_{p,m} = \frac{\alpha\, C_m}{N_{ap}} = \frac{\tau_p}{\tau_c} \log_2\left(1 + \frac{P_p \sum\limits_{k'=1}^{K} l_{mk'} + \sigma_w^2}{Q_{p,m,r}}\right), \tag{7.21}$$

where the term $P_p \sum\limits_{k'=1}^{K} l_{mk'} + \sigma_w^2$ represents the composite received power of each training symbol, and $0 < \alpha < 1$ denotes the portion of allocated fronthaul capacity for pilot transmission. In addition, τ_c and τ_p represent the coherence interval length and the pilot sequence length, respectively. Also, σ_w^2 denotes the noise variance, and P_p represents the transmission power of pilot sequence. Based on this, the received training sequence matrix from the m-th AP at the CPU will be

$$\hat{\boldsymbol{Y}}_{p,m} = \sqrt{P_p \tau_p} \sum_{k'=1}^{K} \boldsymbol{g}_{mk'} \boldsymbol{\psi}_{k'}^T + \boldsymbol{\Omega}_{p,m} + \boldsymbol{W}_{p,m}, \tag{7.22}$$

where $\boldsymbol{\Omega}_{p,m} \in \mathbb{C}^{N_{ap} \times \tau_p}$ denotes the matrix of pilot compression quantization noise. Also, $\boldsymbol{\psi}_{k'} \in \mathbb{C}^{\tau_u \times 1}$ denotes the assigned pilot sequence to user k', and $\boldsymbol{W}_{p,m} \in \mathbb{C}^{N_{ap} \times \tau_p}$, represents the additive noise matrix at the mth AP whose vectors follow $\mathscr{C}\mathscr{N}(0, \sigma_w^2 I_N)$. After

the signals are received at the CPU, the CPU estimates the channel coefficients of all users. In particular, to estimate the k-th user channel with the r-th antenna element in the m-th AP, the CPU applies minimum mean-square error (MMSE)-based channel estimation technique as follows:

$$\breve{g}_{mk,r} = \breve{\epsilon}_{mk}\hat{\boldsymbol{y}}_{p,m,r}\boldsymbol{\psi}_k^*, \tag{7.23}$$

with

$$\breve{\epsilon}_{mk} = \frac{\sqrt{P_p\tau_p}l_{mk}}{P_p\tau_p \sum\limits_{k'=1}^{K} l_{mk'}\left|\boldsymbol{\psi}_{k'}^T\boldsymbol{\psi}_k^*\right|^2 + Q_{p,m,r} + \sigma_w^2}. \tag{7.24}$$

According to the MMSE estimation, the estimated channel at the CPU $\breve{g}_{mk,r}$ and the corresponding channel estimation error $\grave{g}_{mk,r}$ are independent and distributed as

$$\begin{aligned} \breve{g}_{mk,r} &\sim \mathscr{CN}(0, \eta_{mk}), \\ \grave{g}_{mk,r} &\sim \mathscr{CN}(0, l_{mk} - \eta_{mk}), \end{aligned} \tag{7.25}$$

with $\eta_{mk} = \sqrt{P_p\tau_p}l_{mk}\breve{\epsilon}_{mk}$.

7.4.3 Uplink Data Transmission

In what follows, we discuss the UL data transmission where we derive an analytical expression for the achievable UL data rates. In doing so, we apply MRC for UL data detection during the UL transmission phase. Without loss of generality, we develop the analysis considering a typical user located at the origin. During the UL data transmission phase, all users simultaneously transmit their UL data symbols to APs over the same time-frequency resources. Assuming equal power allocation for UL data transmission, the received UL signal at the m-th AP is given by

$$\boldsymbol{z}_m = \sqrt{P_u}\sum_{k=1}^{K}\boldsymbol{g}_{mk}s_k + \boldsymbol{w}_m, \tag{7.26}$$

where $s_k \sim \mathscr{CN}(0,1)$ is the transmitted UL signal from user k while P_u is the UL transmission power. Also, $\boldsymbol{w}_m \in \mathbb{C}^{1 \times N_{ap}}$ is the additive noise vector at the m-th AP whose entries are i.i.d. $\sim \mathscr{CN}(0,1)$. Then, each AP compresses the received UL data signals and sends them through the mmWave fronthaul links to the CPU. In particular, the compressed transmitted signal from the m-th AP to the CPU is given by

$$\hat{\boldsymbol{z}}_m = \boldsymbol{z}_m + \boldsymbol{q}_{d,m}, \tag{7.27}$$

where $\boldsymbol{q}_{d,m}$ represents the quantization noise vector whose entries are i.i.d. $\mathscr{CN}(0, Q_{d,m,r})$. Let us consider $C_{d,m}$ as the assigned fronthaul capacity for UL data transmission from

the r-th antenna element of the m-th AP such that

$$C_{d,m} = \frac{(1-\alpha)C_m}{N_{ap}} = \frac{\tau_c - \tau_p}{\tau_c} \log_2\left(1 + \frac{P_u \sum\limits_{k'=1}^{K} l_{mk'} + \sigma_w^2}{Q_{d,m,r}}\right), \qquad (7.28)$$

where $P_u \sum\limits_{k'=1}^{K} l_{mk'} + \sigma_w^2$ represents the total received power of UL data symbols at different antenna elements of the m-th AP. After the CPU receives the compressed UL signals from all APs, it exploits the estimated users channels during the channel estimation phase to detect the data symbols of each user. In particular, we consider that the CPU applies MRC to detect different users' data symbols. Thus, the UL detected signal of user o is given by

$$y_o = \sqrt{P_u} \sum_{m=1}^{M} \hat{\boldsymbol{g}}_{mo}^H \hat{\boldsymbol{r}}_m + \sum_{m=1}^{M} \hat{\boldsymbol{g}}_{mo}^H \boldsymbol{w}_{m,u}, \qquad (7.29)$$

which can be rewritten as follows:

$$y_o = \underbrace{\sqrt{P_u} \sum_{m=1}^{M} \hat{\boldsymbol{g}}_{mo}^H \hat{\boldsymbol{g}}_{mo} s_o}_{\text{desired signal for user } o} + \underbrace{\sqrt{P_u} \sum_{m=1}^{M} \sum_{k=1}^{K} \hat{\boldsymbol{g}}_{mk}^H \tilde{\boldsymbol{g}}_{mk} s_k}_{\text{estimation error effect}} + \underbrace{\sum_{m=1}^{M} \hat{\boldsymbol{g}}_{mo}^H \boldsymbol{q}_{d,m} s_o}_{\text{quantization noise effect}}$$

$$+ \underbrace{\sqrt{P_u} \sum_{k \neq o} \sum_{m=1}^{M} \hat{\boldsymbol{g}}_{mo}^H \hat{\boldsymbol{g}}_{mk} s_k}_{\text{interference from other users}} + \sum_{m=1}^{M} \underbrace{\hat{\boldsymbol{g}}_{mo}^H \boldsymbol{w}_{m,u}}_{\text{noise}}, \qquad (7.30)$$

where the first term represents the desired signal, and the remaining terms represent the interference due to channel estimation error, quantization noise effect, interference from other users' transmission, and thermal noise effect. Accordingly, the achievable UL data rate for user o can be determined using (7.31) on top of next page.

$$R_o = \mathbb{E}\left[log_2\left(1 + \frac{P_u \left|\sum\limits_{m=1}^{M} \hat{\boldsymbol{g}}_{mo}^H \hat{\boldsymbol{g}}_{mo}\right|^2}{P_u \sum\limits_{k=1}^{K} \sum\limits_{m=1}^{M} (l_{mk} - \eta_{mk}) \left\|\hat{\boldsymbol{g}}_{mo}\right\|^2 + \sum\limits_{m=1}^{M} Q_{d,m,r} \left\|\hat{\boldsymbol{g}}_{mo}\right\|^2 + P_u \sum\limits_{k \neq o} \left|\sum\limits_{m=1}^{M} \hat{\boldsymbol{g}}_{mo}^H \hat{\boldsymbol{g}}_{mk}\right|^2 + \sigma_w^2 \sum\limits_{m=1}^{M} \left\|\hat{\boldsymbol{g}}_{mo}\right\|^2}\right)\right]. \qquad (7.31)$$

However, (7.31) is not in a closed-form, thus, we follow the same procedure as [127] to obtain a closed-from expression of the achievable DL data rate by applying the following approximation

$$\mathbb{E}\left\{\log_2\left(1 + \frac{\mathscr{X}_1}{\mathscr{X}_2}\right)\right\} \approx \log_2\left(1 + \frac{\mathbb{E}\{\mathscr{X}_1\}}{\mathbb{E}\{\mathscr{X}_2\}}\right), \qquad (7.32)$$

where $\mathscr{X}_1$ and $\mathscr{X}_2$ are both sums of non-negative random variables. Applying (7.32) in (7.31), a closed-form approximation of the achievable DL is given by (7.33) where different terms in (7.33) can be calculated as follows.

$$\breve{R}_o = log_2\left(1 + \frac{P_u \mathbb{E}\left[\left|\sum\limits_{m=1}^{M} \hat{\boldsymbol{g}}_{mo}^H \hat{\boldsymbol{g}}_{mo}\right|^2\right]}{P_u \sum\limits_{k=1}^{K} \sum\limits_{m=1}^{M} (l_{mk} - \eta_{mk}) \mathbb{E}\left[\left\|\hat{\boldsymbol{g}}_{mo}\right\|^2\right] + \sum\limits_{m=1}^{M} Q_{d,m,r} \mathbb{E}\left[\left\|\hat{\boldsymbol{g}}_{mo}\right\|^2\right] + P_u \sum\limits_{k \neq o} \mathbb{E}\left[\left|\sum\limits_{m=1}^{M} \hat{\boldsymbol{g}}_{mo}^H \hat{\boldsymbol{g}}_{mk}\right|^2\right] + \sigma_w^2 \sum\limits_{m=1}^{M} \mathbb{E}\left[\left\|\hat{\boldsymbol{g}}_{mo}\right\|^2\right]}\right), \qquad (7.33)$$

Firstly, the desired power P_d is given by

$$
\begin{aligned}
P_d &= P_u \mathbb{E}\left[\left|\sum_{m=1}^{M} \hat{\boldsymbol{g}}_{mo}^{H}\hat{\boldsymbol{g}}_{mo}\right|^2\right] \\
&= P_u \sum_{m=1}^{M} \mathbb{E}\left[|\hat{\boldsymbol{g}}_{mo}^{H}\hat{\boldsymbol{g}}_{mo}|^2\right] + P_u \sum_{m=1}^{M}\sum_{n\neq m} \mathbb{E}\left[|\hat{\boldsymbol{g}}_{mo}^{H}\hat{\boldsymbol{g}}_{mo}|\right]\mathbb{E}\left[|\hat{\boldsymbol{g}}_{no}^{H}\hat{\boldsymbol{g}}_{no}|\right] \\
&= P_u \sum_{m=1}^{M}(N_{ap}^2 + N_{ap})\eta_{mo}^2 + P_u \sum_{m=1}^{M}\sum_{n\neq m} N_{ap}^2 \eta_{mo}\eta_{mk} \\
&= P_u \left(\sum_{m=1}^{M} N_{ap}\eta_{mo}\right)^2 + P_u \sum_{m=1}^{M} N_{ap}\eta_{mo}^2.
\end{aligned}
\tag{7.34}
$$

Also, the interference power due to channel estimation errors will be

$$
EE = \sum_{k=1}^{K}\sum_{m=1}^{M}(l_{mk} - \eta_{mk})\mathbb{E}\left[\|\hat{\boldsymbol{g}}_{mo}\|^2\right] = \sum_{k=1}^{K}\sum_{m=1}^{M} N_{ap}(l_{mk} - \eta_{mk})\eta_{mo}.
\tag{7.35}
$$

The quantization noise power is calculated by

$$
QN_o = \sum_{m=1}^{M} Q_{d,m,r}\mathbb{E}\left[\|\hat{\boldsymbol{g}}_{mo}\|^2\right] = \sum_{m=1}^{M} N_{ap}Q_{d,m,r}\eta_{mo}.
\tag{7.36}
$$

In addition, the interference due to received data from other users is given by

$$
\begin{aligned}
UI_o &= \sum_{k\neq o} \mathbb{E}\left[\left|\sum_{m=1}^{M} \hat{\boldsymbol{g}}_{mo}^{H}\hat{\boldsymbol{g}}_{mk}\right|^2\right] \\
&= P_u \sum_{k\neq o}\sum_{m=1}^{M} N_{ap}\eta_{mo}\eta_{mk} + P_u \sum_{k\neq o}\left(\sum_{m=1}^{M} N_{ap}\eta_{mo}\frac{l_{mk}}{l_{mo}}\right)^2 |\boldsymbol{\psi}_o\boldsymbol{\psi}_k^{H}|^2.
\end{aligned}
\tag{7.37}
$$

Finally, the noise power is given by

$$
N_o = \sigma_w^2 \sum_{m=1}^{M} \mathbb{E}\left[\|\hat{\boldsymbol{g}}_{mo}\|^2\right] = \sigma_w^2 \sum_{m=1}^{M} N_{ap}\eta_{mo}.
\tag{7.38}
$$

Applying some mathematical manipulations, the achievable UL data rate is given by

$$
R_o = \log_2\left(1 + \frac{A_u}{B_u + C_u - D_u + E_u + F_u}\right),
\tag{7.39}
$$

where

$$
A_u = P_u\left(\sum_{m=1}^{M} N_{ap}\eta_{mo}\right)^2 + P_u \sum_{m=1}^{M} N_{ap}\eta_{mo}^2, \qquad B_u = P_u \sum_{k=1}^{K}\sum_{m=1}^{M} N_{ap}\eta_{mo}l_{mk},
$$

$$
C_u = P_u \sum_{k\neq o}\left(\sum_{m=1}^{M} N_{ap}\eta_{mo}\frac{l_{mk}}{l_{mo}}\right)^2 |\boldsymbol{\psi}_o\boldsymbol{\psi}_k^{H}|^2, \qquad D_u = P_u \sum_{m=1}^{M} N_{ap}\eta_{mo}^2,
$$

$$
E_u = P_u \sum_{m=1}^{M} N_{ap}Q_{d,m,r}\eta_{mo}, \qquad F_u = \sigma_w^2 \sum_{m=1}^{M} N_{ap}\eta_{mo}.
$$

7.4.4 Average UL Data Rate

In this section, we derive a tight approximation for the average achievable UL data rates under the quantization noise effect using tools of stochastic geometry. Note that, according

to (7.39), the effect of non-orthogonal pilot sequences depends mainly on the number and locations of users, assigned the same pilot sequence. Due to the randomness in the number and locations of users assigned the same pilot sequences, accounting for these effects renders the analysis more complicated. As such and for ease of analysis and tractability, we do not consider the pilot contamination effect while carrying out the stochastic geometry analysis. Therefore, the achievable DL data rate can be rewritten as

$$R_o = log_2(1 + \gamma_o), \tag{7.40}$$

with

$$\gamma_o = \frac{P_u \left[\left(\sum_{m=1}^{M} N_{ap}\, \eta_{mo} \right)^2 + \sum_{m=1}^{M} N_{ap}\eta_{mo}^2 \right]}{P_u \sum_{k=1}^{K} \sum_{m=1}^{M} N_{ap}\eta_{mo}l_{mk} - P_u \sum_{m=1}^{M} N_{ap}\eta_{mo}^2 + P_u \sum_{m=1}^{M} N_{ap}Q_{d,m,r}\eta_{mo} + \sigma_w^2 \sum_{m=1}^{M} N_{ap}\, \eta_{mo}}. \tag{7.41}$$

Consequently, the average achievable UL data rate over different realizations is given by

$$\bar{R}_o = \mathbb{E}\big[log_2(1 + \gamma_o)\big]. \tag{7.42}$$

One can note that the calculations of $\bar{R}_o$ are challenging since it requires averaging over all APs and users' locations. To circumvent this issue, one needs to simplify the expression of γ_o in (7.41). Since η_{mo}, l_{mo}, and l_{mk} are monotonically decreasing with distance, we apply the mean plus nearest approximation [103] to simplify each individual term in (7.41). Accordingly, the term $\sum_{m=1}^{M} \eta_{mo}$ in the numerator can be approximated by

$$\sum_{m=1}^{M} \eta_{mo} \approx \eta(r_1) + \mathbb{E}\left[\sum_{m'=2}^{M} \eta_{m'o} \big| r_1 \right] \approx \eta(r_1) + \sum_{m'=2}^{M} \int_{r_1}^{\infty} \eta(r)\, f_{R_{1m'}}\big(r\big| r_1\big) dr, \tag{7.43}$$

where m' represents the order of the active APs according to their distances with the typical user. Also, the first term represents the contribution of the nearest AP as a function of its distance from the typical user r_1. In addition, the second term denotes the average contribution of all other APs from the second nearest AP to the mth nearest AP conditioned on the distance with the first nearest AP r_1. Also, the distance distribution of the m'-th nearest AP given the distance r_1 can be expressed by [128]

$$f_{R_{m'}}\big(r\big| r_1\big) = 2\pi\widetilde{\lambda}_a\, r\, \frac{\big[\pi\widetilde{\lambda}_a(r^2 - r_1^2)\big]^{m'-2}}{(m' - 2)!} e^{-\pi\widetilde{\lambda}_a(r^2 - r_1^2)}, \tag{7.44}$$

Hence, (7.43) can be calculated by

$$\sum_{m=1}^{M} \eta_{mo} = \eta(r_1) + \sum_{m'=2}^{M} \int_{r_1}^{\infty} \eta(r) \; 2\pi\widetilde{\lambda}_a \; r \frac{\left[\pi\widetilde{\lambda}_a(r^2 - r_1^2)\right]^{m'-2}}{(m'-2)!} \times e^{-\pi\widetilde{\lambda}_a(r^2-r_1^2)} dr$$

$$= \eta(r_1) + \int_{r_1}^{\infty} \eta(r) \; 2\pi\widetilde{\lambda}_a \; r \; e^{-\pi\widetilde{\lambda}_a(r^2-r_1^2)} \times \sum_{m'=2}^{M} \frac{\left[\pi\widetilde{\lambda}_a(r^2 - r_1^2)\right]^{m'-2}}{(m'-2)!} dr, \quad (7.45)$$

where
$$\sum_{k'=2}^{K} \frac{\left[\pi\widetilde{\lambda}_a(r^2 - r_1^2)\right]^{k'-2}}{(k'-2)!} = \sum_{k'=0}^{K-2} \frac{\left[\pi\widetilde{\lambda}_a(r^2 - r_1^2)\right]^{k'}}{k'!},$$

$$\overset{(a)}{=} e^{\pi\widetilde{\lambda}_a(r^2-r_1^2)}\frac{\Gamma(K-1, \pi\widetilde{\lambda}_a(r^2 - r_1^2))}{\Gamma(K-1)} \overset{(b)}{\approx} e^{\pi\widetilde{\lambda}_a(r^2-r_1^2)}, \quad (7.46)$$

with $\Gamma(\cdot\,,\,\cdot)$ denotes the lower incomplete gamma function. To simplify $\overset{(a)}{=}$ in (7.46) , we consider an asymptotic approach assuming $K \to \infty$ which results in a simpler form as shown in $\overset{(b)}{\approx}$. Hence, the first term of the numerator in (7.41) can be given by

$$\sum_{m=1}^{M} \eta_{mo} \approx \; \eta(r_1) + \int_{r_1}^{\infty} \eta(r) \; 2\pi\widetilde{\lambda}_a r \; dr. \quad (7.47)$$

Similarly, the second term $\sum_{m=1}^{M} \eta_{mo}^2$ in the numerator can also be approximated by

$$\sum_{m=1}^{M} \eta_{mo}^2 \approx \; \eta^2(r_1) + \int_{r_1}^{\infty} \eta^2(r) \; 2\pi\widetilde{\lambda}_a r \; dr. \quad (7.48)$$

Regarding the denominator in (7.41), we firstly neglect the effect of noise. Then, the first term in denominator can be expressed by

$$\sum_{m=1}^{M} \eta_{mo} \sum_{k=1}^{K} l_{mk} = \; \sum_{m=1}^{M} \eta_{mo} l_{mo} + \sum_{m=1}^{M} \eta_{mo} \sum_{k \neq o}^{K} l_{mk}$$

$$\approx \; \eta(r_1) \; l(r_1) + \mathbb{E}\Big[\sum_{m'=2}^{M} \eta_{m'o} l_{m'o}\big|r_1\Big] + \sum_{m=1}^{M} \eta_{mo} \sum_{k \neq o}^{K} l_{mk}, \quad (7.49)$$

where following the same procedure as (7.45) and (7.46), the second term in (7.49) can be calculated by

$$\mathbb{E}\Big[\sum_{m'=2}^{M} \eta_{m'o} l_{m'o}\big|r_1\Big] = \sum_{m'=2}^{M} \int_{r_1}^{\infty} \eta(r) \; l(r) \; f_{R_{m'}}\big(r|r_1\big) \; dr = \int_{r_1}^{\infty} \eta(r) \; l(r) \; 2\pi\widetilde{\lambda}_a \; r \; dr. \quad (7.50)$$

In addition, the third term in (7.49) can be approximated by

$$\sum_{m=1}^{M} \eta_{mo} \sum_{k \neq o}^{K} l_{mk} \overset{(a)}{\approx} \; \mathbb{E}\Big[\sum_{k \neq o}^{K} l_{mk}\Big] \sum_{m=1}^{M} \eta_{mo},$$

$$\approx \int_{0}^{\infty} l(r) \; 2\pi\lambda_u r \; dr \times \Big(\eta(r_1) + \mathbb{E}\Big[\sum_{m'=2}^{M} \eta_{m'o}\big|r_1\Big]\Big), \quad (7.51)$$

$$\approx \int_{0}^{\infty} l(r) \; 2\pi\lambda_u r \; dr \times \Big(\eta(r_1) + \int_{r_1}^{\infty} \eta(r) \; 2\pi\widetilde{\lambda}_a r \; dr\Big)$$

where in $\overset{(a)}{\approx}$, we assume that the summation of large-scale fading coefficients of users on each active AP is independent of the AP index. Then, we apply the mean plus nearest approximation on the summation over the channel estimation variances for the typical user.

Note that, the second term in the denominator of (7.41) is similar to the term in (7.48). The $Q_{d,m,r}$ in (7.41) can be calculated using (7.28) as follows:

$$Q_{d,m,r} = \mathscr{W}_c P_u \sum_{k'=1}^{K} l_{mk'}, \tag{7.52}$$

with

$$\mathscr{W}_c = \frac{1}{2^{\left(\frac{(1-\alpha)\tau_c}{(\tau_c-\tau_p)N_{ap}}c_m\right)} - 1}. \tag{7.53}$$

Thus,

$$\sum_{m=1}^{M} Q_{d,m,r}\eta_{mo} = \sum_{m=1}^{M} \mathscr{W}_c \, \eta_{mo} \sum_{k=1}^{K} l_{mk} \overset{(a)}{\approx} \mathscr{W}_c \, \eta(r_1) \, l(r_1) + \int_{r_1}^{\infty} \mathscr{W}_c \, \eta(r) \, l(r) \, 2\pi\widetilde{\lambda}_a \, r \, dr$$

$$+ \int_{0}^{\infty} \mathscr{W}_c \, l(r) \, 2\pi\lambda_u r \, dr \times \left(\eta(r_1) + \int_{r_1}^{\infty} \eta(r) \, 2\pi\widetilde{\lambda}_a r \, dr\right) \tag{7.54}$$

where $\overset{(a)}{\approx}$ follows the same procedure as in approximating the term in (7.49) where $\mathscr{W}_c$ is independent of the order of the active APs according to their distances with the typical user.

By substituting (7.47)-(7.49), and (7.54) in (7.41), γ_o can be defined by

$$\gamma_o(r_1, c_m) = \frac{N_{ap}\eta(r_1) + \eta^2(r_1) + I_1(r_1)}{(\mathscr{W}_c + 1)\eta(r_1) \, l(r_1) - \eta^2(r_1) + I_2(r_1, c_m) + I_3(r_1, c_m)}. \tag{7.55}$$

$$I_1(r_1) = \int_{r_1}^{\infty} (N_{ap}\eta(r) + \eta^2(r)) \, 2\pi\widetilde{\lambda}_a r \, dr,$$

$$I_2(r_1, c_m) = \int_{r_1}^{\infty} ((\mathscr{W}_c + 1)\eta(r) \, l(r) - \eta^2(r)) \, 2\pi\widetilde{\lambda}_a \, r \, dr,$$

$$I_3(r_1, c_m) = (\mathscr{W}_c + 1) \int_{0}^{\infty} l(r) \, 2\pi\lambda_u r \, dr \times \left(\eta(r_1) + \int_{r_1}^{\infty} \eta(r) \, 2\pi\widetilde{\lambda}_a r \, dr\right).$$

Note that the approximation of γ_o in (7.55) is only a function of the distance of the nearest AP to the typical user r_1 and the achievable capacity of fronthaul link. As such, the average UL data rate in (7.42) can be calculated by averaging over the distance r_1 and the provided capacity c_m as follows:

$$\bar{R}_o = \mathbb{E}_{R_1, C_m}\left[log_2(1 + \gamma_o(r_1, c_m))\right] = \mathbb{E}_{C_m}\left[\mathbb{E}_{R_1}\left[log_2(1 + \gamma_o(r_1, c_m))\big|(C_m = c_m)\right]\right]$$

$$= \int_{c_{min}}^{\infty} \int_{0}^{\infty} log_2\left(1 + \gamma_o(r_1, c_m)\right) \times 2\pi\widetilde{\lambda}_a r_1 e^{-\pi\widetilde{\lambda}_a r_1^2} \times f_{C_m}(c_m) \, d \, r_1 d \, c_m, \tag{7.56}$$

where $E_{R_1,C_m}[.]$ denotes expectation over the random variables R_1 and C_m.

7.5   Simulation Results

We consider a CF mMIMO system where CPUs, APs and users are uniformly distributed in a square area of $[1000\ m \times 1000\ m]$. All simulation results are averaged over 500×10^3 realizations. Results are generated assuming a microwave carrier frequency $f_c = 2$ GHz. Also, the UL pilot and data transmission powers are equal with $P_p = P_u = 100$ mW [122]. The noise variance $\sigma_w^2 = 290 \times \kappa \times \mathscr{B}_A \times NF$ where κ is the Boltzman constant, the system bandwidth $\mathscr{B}_A = 20$ MHz, and $NF = 9$ dB is the noise figure [101]. On the other hand, regarding the fronthaul network communication under mmWave band, we consider a path-loss exponent of $\alpha = 2$ and $A = 69.8$ dB with available contiguous bandwidth up to 5 GHz as in [23, 45]. The total antenna gain for fronthaul link is set to $G_t = 10$ dB, and the transmit power $P_f = 1$ W [27, 42]. Also, we assume that buildings have length and width range of $[10\ m,\ 25\ m]$, and $[10\ m,\ 20\ m]$, respectively [46]. All APs are equipped with $N_{ap} = 4$ antennas, and the densities of APs, users, and CPUs are $\lambda_a = 500/km^2$, $\lambda_u = 50/km^2$, and $\lambda_c = 6/km^2$, respectively, unless otherwise specified.

Considering different target APs activation probabilities, Fig. 7.2 depicts the required density of CPUs to achieve such APs activation probabilities under different blockage densities. It is noted that the required density of CPUs significantly increases with the density of blockages. This can be interpreted from (7.6) where doubling the blockage density increases the required density of CPUs by four-fold to maintain the same activation probability. Also, it can be noted from (7.6) that, at a certain blockage density, the activation probability is a logarithmically increasing function of λ_c. Hence, the required CPUs density exponentially increases with the activation probability. This reflects the significant increase in the required CPUs density as the activation probability increases from $p_a = 0.8$ to $p_a = 0.9$ under different blockage densities. This in turn leads to an extremely high density of required CPUs at higher blockage densities. However, since such high number of CPUs is practically not feasible, it is required to evaluate the performance loss at low activation probabilities compared to higher ones.

In Fig. 7.3, we verify the accuracy of the derived distribution of the achievable capacity of mmWave fronthaul links between CPUs and activated APs given in (7.14). This has been carried out under different densities of APs (Fig. 7.3.a) and different CPU
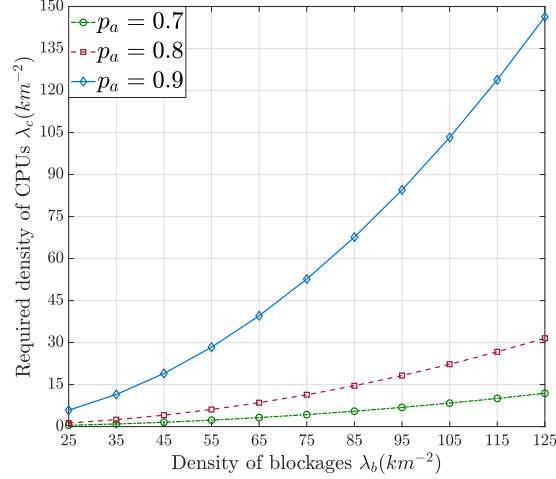
Figure 7.2: Required density of CPUs for certain APs activation probability under different densities of blockages.

densities as well as fronthaul bandwidths (Fig. 7.3.b) assuming a density of blockages $\lambda_b = 400/km^2$. As one can notice, the derived analytical results are consistent with the simulated ones under various simulation parameters. Analyzing the presented results in Fig. 7.3.a for $\lambda_c = 2/km^2$ and fronthaul bandwidth $\mathscr{B}_f = 2$ GHz, one can observe that the mean and variance of the fronthaul capacity distribution decreases as the density of APs increases. The effect of CPU density and fronthaul bandwidth on the capacity distribution is illustrated in Fig. 7.3.b for $\lambda_a = 600/km^2$. As seen, increasing CPU density from 1 $/km^2$ to 2 $/km^2$ leads to an increase in the mean and variance of the achievable fronthaul capacity distribution between APs and CPUs. Also, increasing the fronthaul bandwidth from 2 GHz to 3 GHz improves the achievable fronthaul capacity.

Fig. 7.4 shows the average UL data rates under different densities of blockages and CPUs. The mmWave fronthaul bandwidth is considered to be 1.5 GHz, and $\lambda_a = 400/km^2$. As noted, the simulation results are in perfect agreement with the derived analytical results in (7.56) at different system settings. It is clear that the average UL data rates decrease as the density of blockages increases. This is a consequence of the smaller number of activated APs at higher densities of blockages. However, increasing the density of CPUs remarkably improves the average UL data rates as a result of limiting the number of deactivated APs due to blockages. Besides, the increase in the average UL data rates declines as the density of CPUs gets higher since a reasonable number of APs has been already activated.

Fig. 7.5 depicts the average achievable UL data rates as a function of density of block-

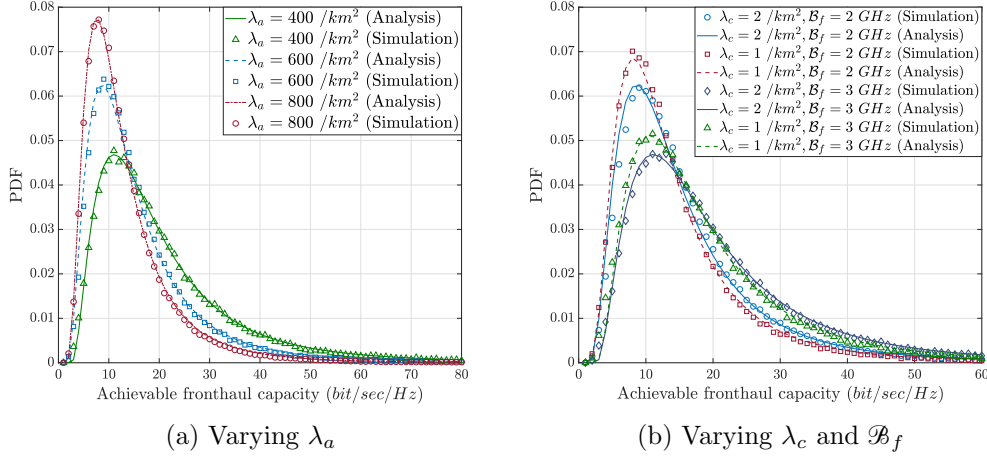(a) Varying λ_a (b) Varying λ_c and $\mathcal{B}_f$

Figure 7.3: The probability distribution functions of the achievable fronthaul capacity distribution for different densities of APs and CPUs as well as assigned bandwidths to fronthaul networks.
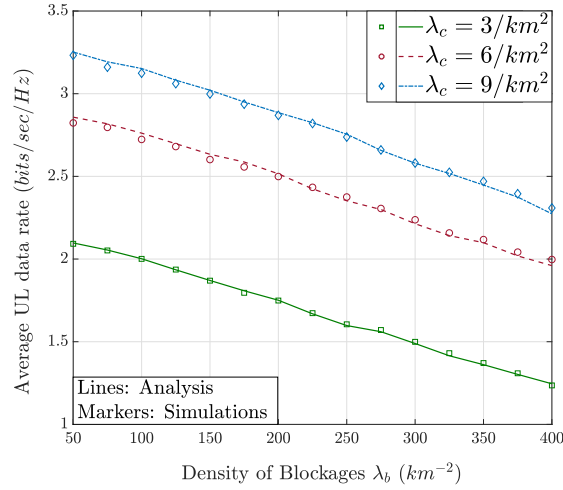

Figure 7.4: Average uplink data rates at different densities of blockages and CPUs.

ages and mmWave fronthaul bandwidth. As noted, increasing the density of blockages degrades the average achievable UL data rates. This is a consequence of decreasing the density of activated APs for the system operation. Furthermore, increasing the available mmWave bandwidth for fronthaul network operation significantly increases the average achievable UL data rates, especially under low-density of blockages, i.e., $\lambda_b = 100/km^2$. However, as the blockage density increases, the improvement in the achievable UL data rates with the mmWave fronthaul bandwidth becomes less prominent.

Fig. 7.6 shows how the average UL data rates are influenced by increasing the density of APs, the number of antennas per AP, and fronthaul bandwidth under a density of blockages $\lambda_b = 200/km^2$. In Fig. 7.6.a, it is noticed that increasing the density of APs
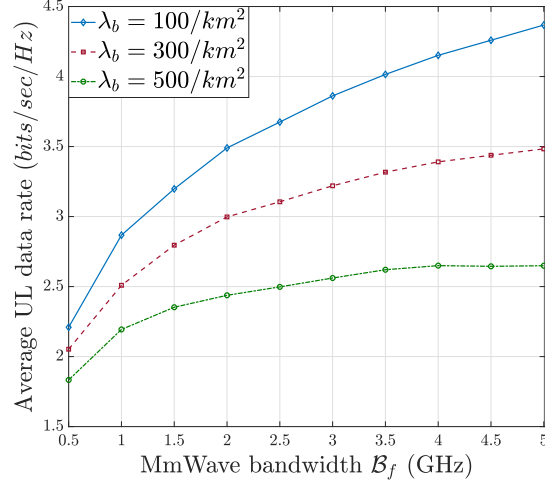
Figure 7.5: Average uplink data rates at different density of blockages and fronthaul bandwidths.

significantly improves the average UL data rates under high bandwidth of the fronthaul network $\mathcal{B}_f = 5$ GHz. This is due to the fact that increasing the density of APs brings more APs closer to CPUs. This, in turns, leads to a corresponding increase in the number of activated APs which improves the provided diversity gains to users. It is shown that the improvement in the average UL data rates due to higher AP density decreases as the fronthaul bandwidth gets smaller. For low bandwidth of the fronthaul network ($\mathcal{B}_f = 0.5$ GHz), the average UL data rates starts to increase with density of APs but finally saturates regardless of the increase of density of APs.

The impact of increasing the number of antennas per AP on the average UL data rates under different fronthaul bandwidths is illustrated in Fig. 7.6.b. One can note that increasing the number of antennas per AP significantly improves the achievable UL data rates under high bandwidth of the fronthaul network $\mathcal{B}_f = 5$ GHz. Nevertheless, decreasing the available bandwidth for fronthaul communication limits this increase in the achievable UL rates. In addition, increasing the number of antennas per AP under small bandwidth for fronthaul communication may lead to a corresponding degradation in the achievable UL data rates. The reason is that the number of transmitted pilot and data signals between APs and their associated CPUs increases linearly with the number of antennas per AP. This in turn increases the compression quantization noise accompanying data transmission over the fronthaul links and significantly affects the achievable UL data rates.

In Fig. 7.7, the average UL data rates are shown at different blockage densities under

(a) Varying density of APs (b) Varying number of antenna per AP
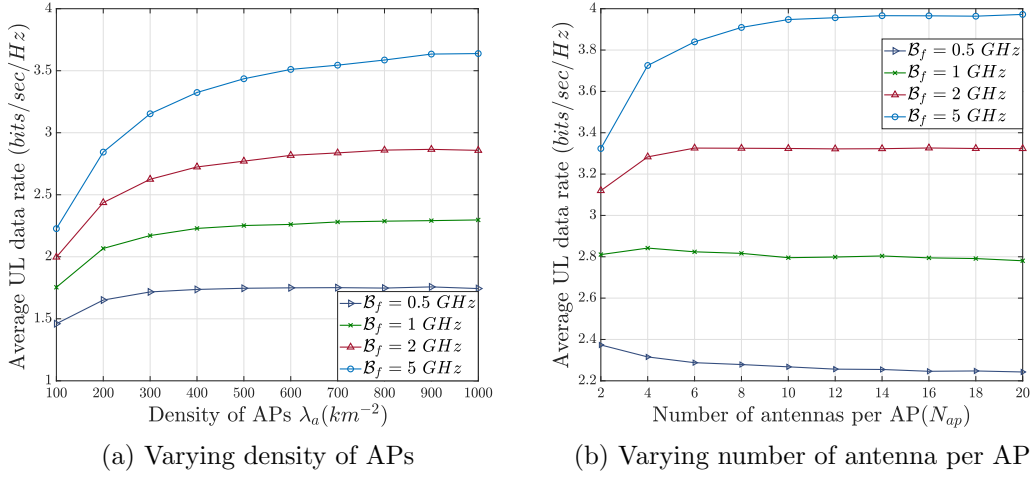
Figure 7.6: Average uplink data rates at different fronthaul bandwidths.

different network configurations. In particular, we consider different combinations of AP densities and number of antennas per APs in each configuration. Also, for a fair comparison, we consider that the total number of antennas in the system is the same for different configurations. The mmWave fronthaul bandwidth is considered to be 2 GHz, and $\lambda_c = 2/km^2$. One can observe that increasing the density of APs ($\lambda_a = 1000/km^2$, $N_{ap} = 2$) attains superior average UL data rates. This is due to improving the provided spatial diversity gains through deploying a larger number of APs with a small number of antennas.

Figure 7.7: Average uplink data rates versus density of blockages for different densities of APs and number of antennas at AP.

7.6   Summary

In this chapter, we investigated the UL performance of CF mMIMO under mmWave-supported fronthaul network. We considered that the system consists of multiple CPUs to which APs a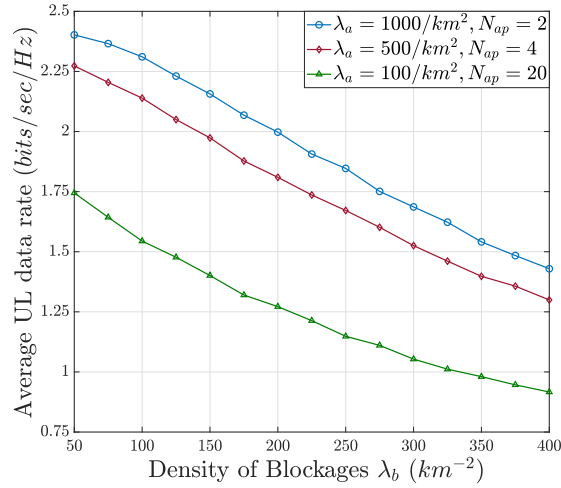re associated in a distance-based association approach. Based on this and using tools from stochastic geometry, we derived the density of activated APs as a function of the blockage and CPU densities. Furthermore, we derived the distribution of achievable fronthaul capacity assuming equal fronthaul bandwidth allocation is obtained at APs. The average UL data rates as a function of the density of active APs. We showed that although increasing the density of blockages degrades the average UL data rates, increasing the density of CPUs can limit such effect. Moreover, the obtained results reveal that the network deployment should be adjusted according to the available fronthaul bandwidth and the density of blockages. In particular, for a given fronthaul bandwidth, increasing the density of APs beyond a certain limit would not achieve further improvement in the UL data rates. Besides, increasing the number of antennas per AP may even cause a degradation in the system performance.

Chapter 8
Conclusions and Future Work

8.1 Conclusions

5G and beyond networks experience a new era of internet of intelligence with connected people and things. This connectivity will be the foundation for increasingly intelligent mobility systems for new technologies, such as smart manufacturing, telehealth, and smart homes which drive our lives into a higher level of convenience and efficiency. These future technologies are facing spectrum shortage challenges mainly due to the massive numbers of connections and the emerging bandwidth-hungry applications. MmWave communication represents one of the most effective solutions to this spectrum scarcity challenge motivated by the immense amount of bandwidth at mmWave bands. Operating at mmWave band imposes technological challenges while offering great opportunities. To overcome these challenges, This thesis considered the development and enhancement of mmWave communications to meet the requirement of 5G and beyond networks. Indeed, the nature of millimeter waves renders the communication quality susceptible due to blockage caused by obstacles. To deal with blockages, we exploited the relaying systems for mmWave networks to guarantee the robustness of network reliability and provide high quality of service. In addition, we investigated the potential of mmWave bands to support the fronthaul network of CF mMIMO systems. Significant contributions have been made in this thesis, which is evident from the track record of publications that resulted from this research work. We briefly summarize these achievements:

1. We have introduced an analytical framework to analyze the network reliability for mmWave relaying system. Capitalizing on this framework, we have investigated the impact of limiting the hop count on the network reliability of mmWave communications. Results obtained via both simulations and analyses revealed the trade-off between the network connectivity and the delay as a function of the hop count.

2. we have proposed a novel routing technique for mmWave networks to improve the spectral efficiency. It is shown that the proposed routing technique outperforms other selection schemes in literature in-terms of spectral efficiency. Results showed that the maximum spectral efficiency is achieved at certain SNR threshold and vary according to the order of selected best relay. Hence, we proposed the adaptive SNR threshold approach based on the order of the best relay. It is observed that the proposed adaptive SNR threshold approach has a significant impact on the spectral efficiency.

3. We have proposed novel routing techniques in the mmWave relaying system to support wide range of use cases for 5G and beyond networks, namely MHC and NLR-MHC routing techniques. We have modeled the distribution of hop count for the aforementioned routing techniques using phase-type distribution, and then we have used this distribution to derive analytical results for the coverage probability and spectral efficiency. This investigation provides accurate and insightful expressions for designing multi-hop mmWave networks to improve data rates and latency while maintaining the network reliability.

4. We have investigated the power consumption and network reliability of IoT devices. Also, we have adapted the proposed relay selection technique for IoT devices in mmWave relaying systems to prolong the IoT device's battery life. Results obtained via both simulations and analyses revealed the trade-off between the network connectivity and the energy consumption of IoT devices. Results also showed a significant impact of blockage density and controlling the relay-selected region on the network connectivity and energy consumption.

5. We have proposed the mmWave communication to support the fronthaul links of CF mMIMO systems. We have provided a comprehensive investigation of different system parameters on the UL performance of mmWave fronthaul-based CF mMIMO systems. It is shown that the UL data rates are significantly affected by the density of blockages in the network. However, increasing the density of CPUs can alleviate the performance degradation at high blockage densities. It has been also shown that increasing the AP density beyond a certain limit would not achieve further improvement in the UL data rates. Also, the higher number of antennas per AP may even cause UL data rates degradation.

8.2   Future Works

In this section, we shed light on some interesting directions of research to further extend the results contributed in this thesis:

1. **Supporting Massive Connectivity for IoT Networks in Millimeter Wave Relaying Systems**

   Many advanced applications in 5G and beyond network, such as smart cities, smart factories, smart agriculture, and smart healthcare lead to IoT revolution. Such huge ranges of smart applications are expected to be supported with massive connectivity. This requires a more efficient, flexible, and agile wireless communication systems. Therefore, an interesting direction for future works is to investigate the problem of supporting reliable connections for massive IoT devices using mmWave relaying systems.

2. **Towards Secure Communications for IoT Networks in Millimeter Wave Relaying Systems**

   Security remains important issue for IoT devices where these devices not only collect personal information but can also monitor user activities. Due to decentralized existence of IoT devices, the confidential messages in IoT architecture are easy to be intercepted and decoded by eavesdroppers. As such, investigating the potential of incorporating physical layer security and mmWave relaying systems to provide data security for IoT devices is highly recommended.

3. **Towards Reliable Communications using Reconfigurable Intelligent Surfaces (RIS) in Millimeter Wave Systems**

   RIS has captured a huge attention from the research community as a key enabling technology to realize a smart control over the radio propagation environment. This stems from the fact the RIS is capable of boosting the received signals quality, extending the communication range, and improving the network security, while maintaining high energy and spectral efficiencies and low computational complexity. In fact, multiple RISs can be used to overcome severe signal blockage between the BS and users to achieve better service coverage. In light of this, the integration of the multi-hop RIS and mmWave networks is although beneficial, but still an open problem.

Appendix:

List of Publications

Journal Articles

1. M. Ibrahim, S. Elhoushy and W. Hamouda, "Uplink Performance of MmWave-Fronthaul Cell-free Massive MIMO Systems," in *IEEE Transactions on Vehicular Technology*, vol. 71, no. 2, pp. 1536-1548, Feb. 2022.

2. S. Elhoushy, M. Ibrahim and W. Hamouda, "Cell-Free Massive MIMO : A Survey," in *IEEE Communications Surveys & Tutorials*, vol. 24, no. 1, pp. 492-523, First quarter 2022.

3. M. Ibrahim and W. Hamouda, "Performance Analysis of Minimum Hop Count-Based Routing Techniques in Millimeter Wave Networks: A Stochastic Geometry Approach,". in *IEEE Transactions on Communications*, vol. 69, no. 12, pp. 8304-8318, Dec. 2021.

4. M. Ibrahim, W. Hamouda and S. Muhaidat, "Spectral Efficiency of Multi-hop Millimeter Wave Networks using N^{th} Best Relay Routing Technique," in *IEEE Transactions on Vehicular Technology*, vol. 69, no. 9, pp. 9951-9959, Sept. 2020.

Conference Proceedings

1. M. Ibrahim and W. Hamouda, "Millimeter Wave-based Fronthaul Network for Cell-free Massive MIMO,". in *2022 IEEE International Conference on Communications (ICC)*, 2022, (Accepted).

2. M. Ibrahim and W. Hamouda, "Reliable Millimeter Wave Communication for IoT Devices,". in *2021 IEEE International Conference on Communications (ICC)*, 2021, pp. 1-6.

3. M. Ibrahim and W. Hamouda, "Impact of Limited Hop Count on Connectivity of Millimeter Wave Networks,". in *GLOBECOM 2020 - 2020 IEEE Global Communications Conference*, 2020, pp. 1-6.

Bibliography

[1] S. Biswas, S. Vuppala, J. Xue, and T. Ratnarajah, "On the performance of relay aided millimeter wave networks," *IEEE Journal of Selected Topics in Signal Processing*, vol. 10, no. 3, pp. 576–588, April 2016.

[2] K. Belbase, Z. Zhang, H. Jiang, and C. Tellambura, "Coverage analysis of millimeter wave decode-and-forward networks with best relay selection," *IEEE Access*, vol. 6, pp. 22 670–22 683, 2018.

[3] B. P. Sahoo, C.-C. Chou, C.-W. Weng, and H.-Y. Wei, "Enabling Millimeter-Wave 5G Networks for Massive IoT Applications: A Closer Look at the Issues Impacting Millimeter-Waves in Consumer Devices Under the 5G Framework," *IEEE Consumer Electronics Magazine*, vol. 8, no. 1, pp. 49–54, 2019.

[4] W. Saad, M. Bennis, and M. Chen, "A Vision of 6G Wireless Systems: Applications, Trends, Technologies, and Open Research Problems," *IEEE Network*, vol. 34, no. 3, pp. 134–142, 2020.

[5] A. Dogra, R. K. Jha, and S. Jain, "A Survey on Beyond 5G Network With the Advent of 6G: Architecture and Emerging Technologies," *IEEE Access*, vol. 9, pp. 67 512–67 547, 2021.

[6] M. Vaezi, A. Azari, S. R. Khosravirad, M. Shirvanimoghaddam, M. M. Azari, D. Chasaki, and P. Popovski, "Cellular, Wide-Area, and Non-Terrestrial IoT: A Survey on 5G Advances and the Road Towards 6G," *IEEE Communications Surveys & Tutorials*, pp. 1–1, 2022.

[7] Y. Wu, S. Singh, T. Taleb, A. Roy, H. S. Dhillon, M. R. Kanagarathinam, and A. De, *6G mobile wireless networks.* Springer, 2021.

[8] I. A. Hemadeh, K. Satyanarayana, M. El-Hajjar, and L. Hanzo, "Millimeter-Wave Communications: Physical Channel Models, Design Considerations, Antenna Con-

structions, and Link-Budget," *IEEE Communications Surveys & Tutorials*, vol. 20, no. 2, pp. 870–913, 2018.

[9] X. Wang, L. Kong, F. Kong, F. Qiu, M. Xia, S. Arnon, and G. Chen, "Millimeter wave communication: A comprehensive survey," *IEEE Communications Surveys Tutorials*, vol. 20, no. 3, pp. 1616–1653, thirdquarter 2018.

[10] G. R. A. N. W. Group *et al.*, "Technical specification group radio access network; NR; NR and NG-RAN overall description. Rel. 16, V. 16.2.0," 3GPP TS 38.300, Tech. Rep., 2020.

[11] J. Huang, Y. Liu, C.-X. Wang, J. Sun, and H. Xiao, "5G Millimeter Wave Channel Sounders, Measurements, and Models: Recent Developments and Future Challenges," *IEEE Communications Magazine*, vol. 57, no. 1, pp. 138–145, 2019.

[12] S. Elhoushy, M. Ibrahim, and W. Hamouda, "Cell-Free Massive MIMO: A Survey," *IEEE Communications Surveys Tutorials*, vol. 24, no. 1, pp. 492–523, 2022.

[13] F. Jameel, S. Wyne, S. J. Nawaz, and Z. Chang, "Propagation channels for mmwave vehicular communications: State-of-the-art and future research directions," *IEEE Wireless Communications*, vol. 26, no. 1, pp. 144–150, 2019.

[14] S. Wu, R. Atat, N. Mastronarde, and L. Liu, "Improving the coverage and spectral efficiency of millimeter-wave cellular networks using device-to-device relays," *IEEE Transactions on Communications*, vol. 66, no. 5, pp. 2251–2265, 2018.

[15] X. Lin and J. G. Andrews, "Connectivity of millimeter wave networks with multi-hop relaying," *IEEE Wireless Communications Letters*, vol. 4, no. 2, pp. 209–212, April 2015.

[16] J. Lianghai, B. Han, M. Liu, and H. D. Schotten, "Applying device-to-device communication to enhance iot services," *IEEE Communications Standards Magazine*, vol. 1, no. 2, pp. 85–91, 2017.

[17] A. Papazafeiropoulos, P. Kourtessis, M. D. Renzo, S. Chatzinotas, and J. M. Senior, "Performance analysis of cell-free massive MIMO systems: A stochastic geometry approach," *IEEE Transactions on Vehicular Technology*, vol. 69, no. 4, pp. 3523–3537, 2020.

[18] A. Adhikary, J. Nam, J. Ahn, and G. Caire, "Joint spatial division and multiplexing–the large-scale array regime," *IEEE Transactions on Information Theory*, vol. 59, no. 10, pp. 6441–6463, Oct 2013.

[19] S. Han, C. I, Z. Xu, and C. Rowell, "Large-scale antenna systems with hybrid analog and digital beamforming for millimeter wave 5G," *IEEE Communications Magazine*, vol. 53, no. 1, pp. 186–194, January 2015.

[20] A. Ghosh, "The 5G mmwave radio revolution." *Microwave Journal*, vol. 59, no. 9, 2016.

[21] S. Baek, D. Kim, M. Tesanovic, and A. Agiwal, "3GPP New Radio Release 16: Evolution of 5G for Industrial Internet of Things," *IEEE Communications Magazine*, vol. 59, no. 1, pp. 41–47, 2021.

[22] G. Americas, "The 5G Evolution: 3GPP Releases 16 and 17," 2020. [Online]. Available: https://www.5gamericas.org/wp-content/uploads/2020/01/5G-Evolution-3GPP-R16-R17-FINAL.pdf

[23] F. C. Commission *et al.*, "Spectrum frontiers report and order and further notice of proposed rulemaking: FCC-16-89A1.pdf," 2016. [Online]. Available: https://docs.fcc.gov/public/attachments/FCC-16-89A1.pdf

[24] A. N. Uwaechia and N. M. Mahyuddin, "A Comprehensive Survey on Millimeter Wave Communications for Fifth-Generation Wireless Networks: Feasibility and Challenges," *IEEE Access*, vol. 8, pp. 62 367–62 414, 2020.

[25] T. S. Rappaport, J. N. Murdock, and F. Gutierrez, "State of the art in 60-GHz integrated circuits and systems for wireless communications," *Proceedings of the IEEE*, vol. 99, no. 8, pp. 1390–1436, 2011.

[26] T. S. Rappaport *et al.*, "Millimeter Wave Mobile Communications for 5G Cellular: It Will Work!" *IEEE Access*, vol. 1, pp. 335–349, 2013.

[27] M. Ibrahim and W. Hamouda, "Reliable Millimeter Wave Communication for IoT Devices," in *ICC 2021 - IEEE International Conference on Communications*, 2021, pp. 1–6.

[28] H. Zhao *et al.*, "28 GHz millimeter wave cellular communication measurements for reflection and penetration loss in and around buildings in new york city," in *2013 IEEE International Conference on Communications (ICC)*, 2013, pp. 5163–5167.

[29] J. Ryan, G. R. MacCartney, and T. S. Rappaport, "Indoor office wideband penetration loss measurements at 73 GHz," in *2017 IEEE International Conference on Communications Workshops (ICC Workshops)*, 2017, pp. 228–233.

[30] G. R. A. N. W. Group *et al.*, "Study on channel model for frequencies from 0.5 to 100 GHz (release 15)," 3GPP TR 38.901, Tech. Rep., 2018.

[31] S. Collonge, G. Zaharia, and G. E. Zein, "Influence of the human activity on wideband characteristics of the 60 GHz indoor radio channel," *IEEE Transactions on Wireless Communications*, vol. 3, no. 6, pp. 2396–2406, 2004.

[32] K. Pahlavan and P. Krishnamurthy, *Principles of wireless access and localization.* John Wiley & Sons, 2013.

[33] S. Rangan, T. S. Rappaport, and E. Erkip, "Millimeter-Wave Cellular Wireless Networks: Potentials and Challenges," *Proceedings of the IEEE*, vol. 102, no. 3, pp. 366–385, 2014.

[34] M. Ibrahim, W. Hamouda, and S. Muhaidat, "Spectral Efficiency of Multi-Hop Millimeter Wave Networks Using Best Relay Routing Technique," *IEEE Transactions on Vehicular Technology*, vol. 69, no. 9, pp. 9951–9959, 2020.

[35] M. Ibrahim and W. Hamouda, "Performance Analysis of Minimum Hop Count-Based Routing Techniques in Millimeter Wave Networks: A Stochastic Geometry Approach," *IEEE Transactions on Communications*, vol. 69, no. 12, pp. 8304–8318, 2021.

[36] M. R. Akdeniz *et al.*, "Millimeter wave channel modeling and cellular capacity evaluation," *IEEE Journal on Selected Areas in Communications*, vol. 32, no. 6, pp. 1164–1179, June 2014.

[37] T. Bai, A. Alkhateeb, and R. W. Heath, "Coverage and capacity of millimeter-wave cellular networks," *IEEE Communications Magazine*, vol. 52, no. 9, pp. 70–77, Sep. 2014.

[38] M. Ashour *et al.*, "A fast ray tracing algorithm for network planning based on relative coverage computations," in *2016 International Conference on Selected Topics in Mobile Wireless Networking (MoWNeT)*, April 2016, pp. 1–6.

[39] J. Lee, J. Choi, J. Lee, and S. Kim, "28 GHz millimeter-wave channel models in urban microcell environment using three-dimensional ray tracing," *IEEE Antennas and Wireless Propagation Letters*, vol. 17, no. 3, pp. 426–429, 2018.

[40] M. Ashour *et al.*, "An enhanced preprocessing dependent image theory algorithm for indoor coverage solutions," in *2016 33rd National Radio Science Conference (NRSC)*, 2016, pp. 274–281.

[41] H. ElSawy, A. Sultan-Salem, M. Alouini, and M. Z. Win, "Modeling and Analysis of Cellular Networks Using Stochastic Geometry: A Tutorial," *IEEE Communications Surveys Tutorials*, vol. 19, no. 1, pp. 167–203, Firstquarter 2017.

[42] M. Ibrahim and W. Hamouda, "Impact of Limited Hop Count on Connectivity of Millimeter Wave Networks," in *GLOBECOM 2020 - 2020 IEEE Global Communications Conference*, 2020, pp. 1–6.

[43] T. Bai and R. W. Heath, "Coverage and rate analysis for millimeter-wave cellular networks," *IEEE Transactions on Wireless Communications*, vol. 14, no. 2, pp. 1100–1114, Feb 2015.

[44] A. Ghosh, T. A. Thomas, M. C. Cudak, R. Ratasuk, P. Moorut, F. W. Vook, T. S. Rappaport, G. R. MacCartney, S. Sun, and S. Nie, "Millimeter-Wave Enhanced Local Area Systems: A High-Data-Rate Approach for Future Wireless Networks," *IEEE Journal on Selected Areas in Communications*, vol. 32, no. 6, pp. 1152–1163, 2014.

[45] S. Singh, M. N. Kulkarni, A. Ghosh, and J. G. Andrews, "Tractable model for rate in self-backhauled millimeter wave cellular networks," *IEEE Journal on Selected Areas in Communications*, vol. 33, no. 10, pp. 2196–2211, Oct 2015.

[46] T. Bai, R. Vaze, and R. W. Heath, "Analysis of Blockage Effects on Urban Cellular Networks," *IEEE Transactions on Wireless Communications*, vol. 13, no. 9, pp. 5070–5083, Sep. 2014.

[47] K. Ntontin and C. Verikoukis, "Relay-Aided Outdoor-to-Indoor Communication in Millimeter-Wave Cellular Networks," *IEEE Systems Journal*, pp. 1–12, 2019.

[48] Y. Niu, W. Ding, H. Wu, Y. Li, X. Chen, B. Ai, and Z. Zhong, "Relay-assisted and QoS aware scheduling to overcome blockage in mmwave backhaul networks," *IEEE Transactions on Vehicular Technology*, vol. 68, no. 2, pp. 1733–1744, Feb 2019.

[49] S. Singh, F. Ziliotto, U. Madhow, E. Belding, and M. Rodwell, "Blockage and directivity in 60 GHz wireless personal area networks: from cross-layer model to multihop MAC design," *IEEE Journal on Selected Areas in Communications*, vol. 27, no. 8, pp. 1400–1413, 2009.

[50] A. Attarkashani and W. Hamouda, "Joint power allocation and subcarrier-relay assignment for OFDM-based decode-and-forward relay networks," *IEEE Communications Letters*, vol. 20, no. 11, pp. 2312–2315, 2016.

[51] M. Elsaadany and W. Hamouda, "Energy efficient design for non-orthogonal AF relaying in underlay spectrum sharing networks," in *2016 IEEE International Conference on Communications (ICC)*, 2016, pp. 1–6.

[52] S. Wang, X. Xu, K. Huang, X. Ji, Y. Chen, and L. Jin, "Artificial noise aided hybrid analog-digital beamforming for secure transmission in MIMO millimeter wave relay systems," *IEEE Access*, vol. 7, pp. 28 597–28 606, 2019.

[53] M. Haenggi, "Stochastic geometry for wireless networks, cambridge uni," 2013.

[54] H. P. Keeler, *Notes on the Poisson point process.* Weierstrass Inst., Berlin, Germany, Tech, 2016.

[55] H. ElSawy, E. Hossain, and M. Haenggi, "Stochastic Geometry for Modeling, Analysis, and Design of Multi-Tier and Cognitive Cellular Wireless Networks: A Survey," *IEEE Communications Surveys Tutorials*, vol. 15, no. 3, pp. 996–1019, Third 2013.

[56] M. Giordani, M. Polese, M. Mezzavilla, S. Rangan, and M. Zorzi, "Toward 6G networks: Use cases and technologies," *IEEE Communications Magazine*, vol. 58, no. 3, pp. 55–61, 2020.

[57] L. Wenxing, W. Muqing, Z. Min, L. Peizhe, and L. Tianze, "Hop count limitation analysis in wireless multi-hop networks," *International Journal of Distributed Sensor Networks*, vol. 13, no. 1, p. 1550147716683606, 2017.

[58] M. Giordani, M. Polese, A. Roy, D. Castor, and M. Zorzi, "A tutorial on beam management for 3GPP NR at mmWave frequencies," *IEEE Communications Surveys Tutorials*, vol. 21, no. 1, pp. 173–196, 2019.

[59] C. Zhang and X. Luo, "Adaptive digital self-interference cancellation for millimeter-wave full-duplex backhaul systems," *IEEE Access*, vol. 7, pp. 175 542–175 553, 2019.

[60] G. R. MacCartney, T. S. Rappaport, and S. Rangan, "Rapid fading due to human blockage in pedestrian crowds at 5G millimeter-wave frequencies," in *GLOBECOM 2017 - 2017 IEEE Global Communications Conference*, 2017, pp. 1–7.

[61] K. Han, Y. Cui, Y. Wu, and K. Huang, "The connectivity of millimeter wave networks in urban environments modeled using random lattices," *IEEE Transactions on Wireless Communications*, vol. 17, no. 5, pp. 3357–3372, May 2018.

[62] B. Anjum and H. Perros, "Adding percentiles of erlangian distributions," *IEEE Communications Letters*, vol. 15, no. 3, pp. 346–348, March 2011.

[63] A. Leon-Garcia, *Probability, statistics, and random processes for electrical engineering*, 3rd ed. Pearson Education, 2007.

[64] K. Belbase, C. Tellambura, and H. Jiang, "Coverage, capacity, and error rate analysis of multi-hop millimeter-wave decode and forward relaying," *IEEE Access*, vol. 7, pp. 69 638–69 656, 2019.

[65] M. Gerasimenko, D. Moltchanov, M. Gapeyenko, S. Andreev, and Y. Koucheryavy, "Capacity of Multiconnectivity mmWave Systems With Dynamic Blockage and Directional Antennas," *IEEE Transactions on Vehicular Technology*, vol. 68, no. 4, pp. 3534–3549, April 2019.

[66] P. Yang, Q. Zhang, and J. Qin, "Exact outage probability of nth-best multicast relay networks with co-channel interference," *IEEE Wireless Communications Letters*, vol. 2, no. 6, pp. 595–598, December 2013.

[67] M. S. Alam, G. Kaddoum, and B. L. Agba, "A novel relay selection strategy of cooperative network impaired by bursty impulsive noise," *IEEE Transactions on Vehicular Technology*, vol. 68, no. 7, pp. 6622–6635, July 2019.

[68] M. Gapeyenko, V. Petrov, D. Moltchanov, M. R. Akdeniz, S. Andreev, N. Himayat, and Y. Koucheryavy, "On the degree of multi-connectivity in 5G millimeter-wave cellular urban deployments," *IEEE Transactions on Vehicular Technology*, vol. 68, no. 2, pp. 1973–1978, Feb 2019.

[69] H. Hashemi, J. Haghighat, M. Eslami, and W. A. Hamouda, "Analysis of equal gain combining over fluctuating two-ray channels with applications to millimeter-wave communications," *IEEE Transactions on Vehicular Technology*, vol. 69, no. 2, pp. 1751–1765, 2020.

[70] M. I. Kamel, W. Hamouda, and A. M. Youssef, "Multiple association in ultra-dense networks," in *2016 IEEE International Conference on Communications (ICC)*, 2016, pp. 1–6.

[71] Y. Yao, H. Tian, G. Nie, H. Wu, and J. Jin, "Multi-path routing based QoS-aware fairness backhaul-access scheduling in mmWave UDN," in *2018 IEEE 29th Annual International Symposium on Personal, Indoor and Mobile Radio Communications (PIMRC)*, Sep. 2018, pp. 1–7.

[72] G. Yang, M. Haenggi, and M. Xiao, "Traffic allocation for low-latency multi-hop networks with buffers," *IEEE Transactions on Communications*, vol. 66, no. 9, pp. 3999–4013, 2018.

[73] H. Jung and I.-H. Lee, "Outage analysis of multihop wireless backhaul using millimeter wave under blockage effects," *International Journal of Antennas and Propagation*, 2017.

[74] ——, "Performance Analysis of Millimeter-Wave Multi-hop Machine-to-Machine Networks Based on Hop Distance Statistics," *Sensors*, vol. 18, no. 2, p. 204, Jan 2018. [Online]. Available: http://dx.doi.org/10.3390/s18010204

[75] Y. Liang and T. Li, "End-to-End Throughput in Multihop Wireless Networks With Random Relay Deployment," *IEEE Transactions on Signal and Information Processing over Networks*, vol. 4, no. 3, pp. 613–625, 2018.

[76] H. U. Yildiz, M. Temiz, and B. Tavli, "Impact of limiting hop count on the lifetime of wireless sensor networks," *IEEE Communications Letters*, vol. 19, no. 4, pp. 569–572, April 2015.

[77] T. K. Vu, M. Bennis, M. Debbah, and M. Latva-Aho, "Joint path selection and rate allocation framework for 5G self-backhauled mm-wave networks," *IEEE Transactions on Wireless Communications*, vol. 18, no. 4, pp. 2431–2445, 2019.

[78] G. Rahmatollahi and G. Abreu, "Closed-form hop-count distributions in random networks with arbitrary routing," *IEEE Transactions on Communications*, vol. 60, no. 2, pp. 429–444, February 2012.

[79] J. Kuo and W. Liao, "Hop count distribution of multihop paths in wireless networks with arbitrary node density: Modeling and its applications," *IEEE Transactions on Vehicular Technology*, vol. 56, no. 4, pp. 2321–2331, July 2007.

[80] R. Verbelen, "Phase-type distributions & mixtures of erlangs," Ph.D. dissertation, UNIVERSITY OF LEUVEN, 2013.

[81] H. Shokri-Ghadikolaei, C. Fischione, G. Fodor, P. Popovski, and M. Zorzi, "Millimeter Wave Cellular Networks: A MAC Layer Perspective," *IEEE Transactions on Communications*, vol. 63, no. 10, pp. 3437–3458, 2015.

[82] J. G. Andrews, T. Bai, M. N. Kulkarni, A. Alkhateeb, A. K. Gupta, and R. W. Heath, "Modeling and Analyzing Millimeter Wave Cellular Systems," *IEEE Transactions on Communications*, vol. 65, no. 1, pp. 403–430, Jan 2017.

[83] M. Haenggi, "On routing in random Rayleigh fading networks," *IEEE Transactions on Wireless Communications*, vol. 4, no. 4, pp. 1553–1562, July 2005.

[84] M. F. Neuts, *Matrix-geometric solutions in stochastic models: an algorithmic approach.* Courier Corporation, 1994.

[85] A. Thummler, P. Buchholz, and M. Telek, "A novel approach for phase-type fitting with the EM algorithm," *IEEE Transactions on Dependable and Secure Computing*, vol. 3, no. 3, pp. 245–258, July 2006.

[86] V. N. Q. Bao and H. Y. Kong, "Performance analysis of decode-and-forward relaying with partial relay selection for multihop transmission over rayleigh fading channels," *Journal of Communications and Networks*, vol. 12, no. 5, pp. 433–441, 2010.

[87] R. Amer, H. Elsawy, M. M. Butt, E. A. Jorswieck, M. Bennis, and N. Marchetti, "Optimized Caching and Spectrum Partitioning for D2D Enabled Cellular Systems With Clustered Devices," *IEEE Transactions on Communications*, vol. 68, no. 7, pp. 4358–4374, 2020.

[88] C. M. Bender and S. A. Orszag, *Advanced mathematical methods for scientists and engineers I: Asymptotic methods and perturbation theory.* Springer Science & Business Media, 2013.

[89] S. Asmussen, J. L. Jensen, and L. Rojas-Nandayapa, "On the laplace transform of the lognormal distribution," *Methodology and Computing in Applied Probability*, vol. 18, no. 2, pp. 441–458, 2016.

[90] M. Elbayoumi, M. Kamel, W. Hamouda, and A. Youssef, "NOMA-assisted machine-type communications in UDN: State-of-the-art and challenges," *IEEE Communications Surveys & Tutorials*, vol. 22, no. 2, pp. 1276–1304, 2020.

[91] "Ericsson mobility report." [Online]. Available: https://www.ericsson.com/49da93/assets/local/mobility-report/documents/2020/june2020-ericsson-mobility-report.pdf

[92] S. Kwon and J. Widmer, "Relay selection for mmWave communications," in *2017 IEEE 28th Annual International Symposium on Personal, Indoor, and Mobile Radio Communications (PIMRC)*, Oct 2017, pp. 1–6.

[93] Z. Wang, X. Qin, and B. Liu, "An energy-efficient clustering routing algorithm for WSN-assisted IoT," in *2018 IEEE Wireless Communications and Networking Conference (WCNC)*, 2018, pp. 1–6.

[94] A. Carroll, G. Heiser *et al.*, "An analysis of power consumption in a smartphone." in *USENIX annual technical conference*, vol. 14. Boston, MA, 2010, pp. 21–21.

[95] B. Martinez, M. Montón, I. Vilajosana, and J. D. Prades, "The power of models: Modeling power consumption for IoT devices," *IEEE Sensors Journal*, vol. 15, no. 10, pp. 5777–5789, 2015.

[96] A. Saci, A. Al-Dweik, A. Shami, and Y. Iraqi, "One-Shot Blind Channel Estimation for OFDM Systems Over Frequency-Selective Fading Channels," *IEEE Transactions on Communications*, vol. 65, no. 12, pp. 5445–5458, 2017.

[97] D. J. Dechene and A. Shami, "Energy-Aware Resource Allocation Strategies for LTE Uplink with Synchronous HARQ Constraints," *IEEE Transactions on Mobile Computing*, vol. 13, no. 2, pp. 422–433, 2014.

[98] H. Q. Ngo, A. Ashikhmin, H. Yang, E. G. Larsson, and T. L. Marzetta, "Cell-free massive MIMO versus small cells," *IEEE Transactions on Wireless Communications*, vol. 16, no. 3, pp. 1834–1850, 2017.

[99] E. Björnson and L. Sanguinetti, "Making cell-free massive MIMO competitive with MMSE processing and centralized implementation," *IEEE Transactions on Wireless Communications*, vol. 19, no. 1, pp. 77–90, 2020.

[100] S. Elhoushy and W. Hamouda, "Performance of distributed massive MIMO and small-cell systems under hardware and channel impairments," *IEEE Transactions on Vehicular Technology*, vol. 69, no. 8, pp. 8627–8642, 2020.

[101] G. Femenias and F. Riera-Palou, "Fronthaul-Constrained Cell-Free Massive MIMO With Low Resolution ADCs," *IEEE Access*, vol. 8, pp. 116 195–116 215, 2020.

[102] S. Elhoushy and W. Hamouda, "Downlink performance of limited-fronthaul cell-free massive mimo," in *ICC 2021 - IEEE International Conference on Communications*, 2021, pp. 1–6.

[103] P. Parida, H. S. Dhillon, and A. F. Molisch, "Downlink Performance Analysis of Cell-Free Massive MIMO with Finite Fronthaul Capacity," in *2018 IEEE 88th Vehicular Technology Conference (VTC-Fall)*, 2018, pp. 1–6.

[104] H. Masoumi and M. J. Emadi, "Performance analysis of cell-free massive MIMO system with limited fronthaul capacity and hardware impairments," *IEEE Transactions on Wireless Communications*, vol. 19, no. 2, pp. 1038–1053, 2020.

[105] D. Maryopi, M. Bashar, and A. Burr, "On the uplink throughput of zero forcing in cell-free massive MIMO with coarse quantization," *IEEE Transactions on Vehicular Technology*, vol. 68, no. 7, pp. 7220–7224, 2019.

[106] M. Bashar *et al.*, "Max–Min rate of cell-free massive MIMO uplink with optimal uniform quantization," *IEEE Transactions on Communications*, vol. 67, no. 10, pp. 6796–6815, 2019.

[107] M. Bashar, K. Cumanan, A. G. Burr, H. Q. Ngo, E. G. Larsson, and P. Xiao, "Energy efficiency of the cell-free massive MIMO uplink with optimal uniform quantization," *IEEE Transactions on Green Communications and Networking*, vol. 3, no. 4, pp. 971–987, 2019.

[108] M. Polese, M. Giordani, T. Zugno, A. Roy, S. Goyal, D. Castor, and M. Zorzi, "Integrated Access and Backhaul in 5G mmWave Networks: Potential and Challenges," *IEEE Communications Magazine*, vol. 58, no. 3, pp. 62–68, 2020.

[109] D. Bojic, E. Sasaki, N. Cvijetic, T. Wang, J. Kuno, J. Lessmann, S. Schmid, H. Ishii, and S. Nakamura, "Advanced wireless and optical technologies for small-cell mobile backhaul with dynamic software-defined management," *IEEE Communications Magazine*, vol. 51, no. 9, pp. 86–93, 2013.

[110] Z. Shi, W. Gao, S. Zhang, J. Liu, and N. Kato, "Machine Learning-Enabled Cooperative Spectrum Sensing for Non-Orthogonal Multiple Access," *IEEE Transactions on Wireless Communications*, vol. 19, no. 9, pp. 5692–5702, 2020.

[111] ——, "AI-Enhanced Cooperative Spectrum Sensing for Non-Orthogonal Multiple Access," *IEEE Wireless Communications*, vol. 27, no. 2, pp. 173–179, 2020.

[112] A. Ali and W. Hamouda, "Advances on spectrum sensing for cognitive radio networks: Theory and applications," *IEEE Communications Surveys Tutorials*, vol. 19, no. 2, pp. 1277–1304, 2017.

[113] P. Agheli, M. J. Emadi, and H. Beyranvand, "Designing Cost-and Energy-Efficient Cell-Free Massive MIMO Network with Fiber and FSO Fronthaul Links," *arXiv preprint arXiv:2011.08511*, 2020.

[114] S. A. Al-Gailani, M. F. Mohd Salleh, A. A. Salem, R. Q. Shaddad, U. U. Sheikh, N. A. Algeelani, and T. A. Almohamad, "A Survey of Free Space Optics (FSO) Communication Systems, Links, and Networks," *IEEE Access*, vol. 9, pp. 7353–7373, 2021.

[115] E. Verdugo, R. Nebuloni, L. Luini, C. Riva, L. d. S. Mello, and G. Roveda, "Rain Effects on FSO and mmWave Links: Preliminary Results from an Experimental Study," in *2020 29th Wireless and Optical Communications Conference (WOCC)*, 2020, pp. 1–6.

[116] R. G. Stephen and R. Zhang, "Joint millimeter-wave fronthaul and OFDMA resource allocation in ultra-dense CRAN," *IEEE Transactions on Communications*, vol. 65, no. 3, pp. 1411–1423, 2017.

[117] M. Alonzo and S. Buzzi, "Cell-free and user-centric massive MIMO at millimeter wave frequencies," in *2017 IEEE 28th Annual International Symposium on Personal, Indoor, and Mobile Radio Communications (PIMRC)*, 2017, pp. 1–5.

[118] M. Alonzo, S. Buzzi, and A. Zappone, "Energy-efficient downlink power control in mmWave cell-free and user-centric massive MIMO," in *2018 IEEE 5G World Forum (5GWF)*, 2018, pp. 493–496.

[119] S. Choi, J. Choi, and S. Bahk, "Mobility-aware analysis of millimeter wave communication systems with blockages," *IEEE Transactions on Vehicular Technology*, vol. 69, no. 6, pp. 5901–5912, 2020.

[120] F. Tang, Y. Zhou, and N. Kato, "Deep Reinforcement Learning for Dynamic Uplink/Downlink Resource Allocation in High Mobility 5G HetNet," *IEEE Journal on Selected Areas in Communications*, vol. 38, no. 12, pp. 2773–2782, 2020.

[121] E. Björnson and L. Sanguinetti, "Scalable cell-free massive mimo systems," *IEEE Transactions on Communications*, vol. 68, no. 7, pp. 4247–4261, 2020.

[122] S. Elhoushy and W. Hamouda, "Limiting doppler shift effect on cell-free massive mimo systems: A stochastic geometry approach," *IEEE Transactions on Wireless Communications*, vol. 20, no. 9, pp. 5656–5671, 2021.

[123] B. Yang, G. Mao, M. Ding, X. Ge, and X. Tao, "Dense Small Cell Networks: From Noise-Limited to Dense Interference-Limited," *IEEE Transactions on Vehicular Technology*, vol. 67, no. 5, pp. 4262–4277, 2018.

[124] S. M. Yu and S. Kim, "Downlink capacity and base station density in cellular networks," in *2013 11th International Symposium and Workshops on Modeling and Optimization in Mobile, Ad Hoc and Wireless Networks (WiOpt)*, 2013, pp. 119–124.

[125] M. Elbayoumi, W. Hamouda, and A. Youssef, "Multiple-Association Supporting HTC/MTC in Limited-Backhaul Capacity Ultra-Dense Networks," *IEEE Transactions on Communications*, vol. 69, no. 6, pp. 4113–4127, 2021.

[126] T. Cover and A. Joy, *Elements of Information Theory.* John Wiley & Sons, New York, USA, 2012.

[127] G. Interdonato, H. Q. Ngo, P. Frenger, and E. G. Larsson, "Downlink training in cell-free massive MIMO: A blessing in disguise," *IEEE Transactions on Wireless Communications*, vol. 18, no. 11, pp. 5153–5169, 2019.

[128] D. Moltchanov, "Distance distributions in random networks," *Ad Hoc Networks*, vol. 10, no. 6, pp. 1146–1166, 2012.